



SYNTHESIS AND CHARACTERIZATION OF NICKEL-BASED MIXED OXIDES FOR ETHANOL STEAM REFORMING

Evgeny Bolshak

ADVERTIMENT. L'accés als continguts d'aquesta tesi doctoral i la seva utilització ha de respectar els drets de la persona autora. Pot ser utilitzada per a consulta o estudi personal, així com en activitats o materials d'investigació i docència en els termes establerts a l'art. 32 del Text Refós de la Llei de Propietat Intel·lectual (RDL 1/1996). Per altres utilitzacions es requereix l'autorització prèvia i expressa de la persona autora. En qualsevol cas, en la utilització dels seus continguts caldrà indicar de forma clara el nom i cognoms de la persona autora i el títol de la tesi doctoral. No s'autoritza la seva reproducció o altres formes d'explotació efectuades amb finalitats de lucre ni la seva comunicació pública des d'un lloc aliè al servei TDX. Tampoc s'autoritza la presentació del seu contingut en una finestra o marc aliè a TDX (framing). Aquesta reserva de drets afecta tant als continguts de la tesi com als seus resums i índexs.

ADVERTENCIA. El acceso a los contenidos de esta tesis doctoral y su utilización debe respetar los derechos de la persona autora. Puede ser utilizada para consulta o estudio personal, así como en actividades o materiales de investigación y docencia en los términos establecidos en el art. 32 del Texto Refundido de la Ley de Propiedad Intelectual (RDL 1/1996). Para otros usos se requiere la autorización previa y expresa de la persona autora. En cualquier caso, en la utilización de sus contenidos se deberá indicar de forma clara el nombre y apellidos de la persona autora y el título de la tesis doctoral. No se autoriza su reproducción u otras formas de explotación efectuadas con fines lucrativos ni su comunicación pública desde un sitio ajeno al servicio TDR. Tampoco se autoriza la presentación de su contenido en una ventana o marco ajeno a TDR (framing). Esta reserva de derechos afecta tanto al contenido de la tesis como a sus resúmenes e índices.

WARNING. Access to the contents of this doctoral thesis and its use must respect the rights of the author. It can be used for reference or private study, as well as research and learning activities or materials in the terms established by the 32nd article of the Spanish Consolidated Copyright Act (RDL 1/1996). Express and previous authorization of the author is required for any other uses. In any case, when using its content, full name of the author and title of the thesis must be clearly indicated. Reproduction or other forms of for profit use or public communication from outside TDX service is not allowed. Presentation of its content in a window or frame external to TDX (framing) is not authorized either. These rights affect both the content of the thesis and its abstracts and indexes.

UNIVERSITAT ROVIRA I VIRGILI

DEPARTAMENT OF CHEMICAL ENGINEERING



**SYNTHESIS AND CHARACTERIZATION OF
NICKEL-BASED MIXED OXIDES FOR
ETHANOL STEAM REFORMING**



UNIVERSITAT ROVIRA I VIRGILI

DOCTORAL THESIS

EVGENY BOLSHAK

July 2015

Evgeny Bolshak

**SYNTHESIS AND CHARACTERIZATION OF NICKEL-BASED MIXED
OXIDES FOR ETHANOL STEAM REFORMING**

DOCTORAL THESIS

Supervised by Dr. Daniel Montané and Dr. Sònia Abelló

Department of Chemical Engineering



UNIVERSITAT ROVIRA I VIRGILI

Tarragona

2015



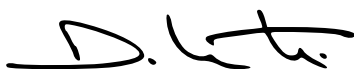
**Departament d'Enginyeria
Química**

Av. Països Catalans 26.
Campus Sescelades
43007 Tarragona (Spain)
Tel.: 977 55 97 20
Fax.: 977 55 96 21

WE STATE that the present study, entitled "Synthesis and characterization of nickel-based mixed oxides for ethanol steam reforming", presented by Evgeny Bolshak for the award of the degree of Doctor, has been carried out under our supervision at the Department of Chemical Engineering of this university, and that it fulfills all the requirements to be eligible for the Doctorate Award.

Tarragona, 22 of July of 2015

Doctoral thesis supervisors:



Dr. Daniel Montané



Dr. Sònia Abelló

Acknowledgements:

First, I would like to thank my PhD supervisors Dr. Daniel Montané and Sònia Abelló for the opportunity to do this PhD project, for many provided opportunities during doing this job, for support during the work and for helpful advices. I am very grateful to them for their kindness and guidance.

I would also like to specially thank Jozefa Làzaro for her priceless aid in solving administrative and laboratory issues. Other special thanks go to my PhD coordinator Nuria Juanpere for the patience and quickness in solving urgent questions. I would also like to thank my group colleagues for quiet and working atmosphere.

Many thanks to all my Russian-speaking friends here in Spain and back in Russia, especially to Anna Pankratova for sharing their spare time and priceless support. Last, but not least, I would like to express my deep gratefulness to my family and especially to my mother Galina, my father Oleg and my sister Olga.

Tarragona, July 2015

Table of contents:

1. Introduction and overview	1
1.1. Hydrogen as an energy carrier	3
1.2. Hydrogen from ethanol	4
1.3. Catalysts for the steam reforming of ethanol	6
1.3.1. Noble-metal catalysts	9
1.3.2. Cobalt-based catalysts	10
1.3.3. Nickel-based catalysts	12
1.3.4. Aim and overview of the Thesis	17
1.4. References	19
2. Ni-Fe catalysts derived from hydrotalcite-like precursors for hydrogen production by ethanol steam reforming	23
2.1. Introduction	25
2.2. Experimental	28
2.2.1. Catalyst preparation	28
2.2.2. Catalyst characterization	29
2.2.3. Catalyst testing	30
2.3. Results and discussion	32
2.3.1. Reevesite activation	32
2.3.1.1. As-synthesized samples	32
2.3.1.2. Thermal decomposition	35
2.3.1.3. Reduction behavior	42
2.3.2. Steam reforming performance	47
2.3.2.1. Effect of Ni/Fe molar ratio	48
2.3.2.2. Effect of calcination conditions	57
2.3.2.3. Characterization of used catalysts	60
2.4. Conclusions	64
2.5. References	66
2.6. Appendix for chapter 2	69
3. Ethanol steam reforming over Ni-Fe-based hydrotalcites: effect of iron content and reaction temperature	71
3.1. Introduction	73

3.2. Experimental	75
3.2.1. Catalyst preparation and activation	75
3.2.2. Catalyst characterization	75
3.2.3. Catalytic tests	77
3.3. Results and discussion	78
3.3.1. Characterization of as-synthesized and calcined samples	78
3.3.2. Activity tests	83
3.3.2.1. Effect of the nickel to iron molar ratio	83
3.3.2.2. Effect of the reaction temperature	89
3.4. Conclusions	95
3.5. References	96
4. Ternary Ni-Al-Fe catalysts for ethanol steam reforming	99
4.1. Introduction	101
4.2. Experimental	102
4.2.1. Catalyst preparation	102
4.2.2. Catalyst characterization	103
4.2.3. Catalytic tests	105
4.3. Results and discussion	106
4.3.1. Catalyst characterization	106
4.3.2. Steam reforming performance	114
4.3.3. Characterization of used catalysts	120
4.4. Conclusions	124
4.5. References	126
4.6. Appendix for chapter 4	129
5. Summary, conclusions and outlook	131
5.1. Summary	133
5.2. Conclusions	135
5.3. Outlook and future work	136
5.4. List of publications	137
5.5. About the author	139

List of Figures:

Figure 1.1. Process flow diagram of a fuel processor based on SCWR directly coupled to a PEMFC unit	5
Figure 1.2. General structure of hydrotalcites	14
Scheme 1. Schematic representation of the set-up used to perform activity tests.....	31
Figure 2.1. XRD patterns of the as-synthesized reevesites (P) and the products of calcination at 773 and 1073 K.....	34
Figure 2.2 Transmission electron micrographs of the different samples.....	36
Figure 2.3. Thermogravimetric and calorimetric profiles of the as-synthesized reevesite samples in air and derivative of the weight loss.....	40
Figure 2.4. Raman spectra of the Ni-Fe oxides obtained upon calcination at 773 (black lines) and 1073 K (grey lines).....	41
Figure 2.5. H ₂ -TPR profiles of the Ni-Fe catalysts calcined at different conditions....	44
Figure 2.6. XRD patterns of the used Ni-Fe oxides.....	46
Figure 2.7 Ethanol conversion and selectivity to the different products vs time during ethanol steam reforming over the Ni-Fe catalysts calcined at 773 K.....	50
Figure 2.8. Ethanol conversion and selectivity to the different products vs time during ethanol steam reforming over the Ni-Fe catalysts calcined at 1073 K.	55
Figure 2.9. Ethanol conversion and selectivity to the different products during ethanol steam reforming over all Ni-Fe catalysts.....	59
Figure 2.10. Selected transmission electron micrographs of the NiFe-U-C773 and NiFe-U-C1073 samples.	61
Figure 2.11. Raman spectra of the Ni-Fe catalysts after 24 h of reaction. Black and grey lines correspond to samples calcined at 773 K and 1073 K, respectively.....	63
Figure 2.SI1. Ethanol conversion and selectivity to the different products vs time during ethanol steam reforming over the NiFe-C773.....	69
Figure 2.SI2. Percentage of crystalline phases determined by XRD Rietveld refinement of the catalysts after a 24 h reaction period.....	69
Figure 2.SI3. XRD patterns of the used NiFe-C773 sample after reaction at 773 K for 1 h.....	70
Figure 3.1. XRD patterns of precursors and calcined samples with Ni/Fe ratios 1:1 and 0.5:1	79

Figure 3.2. Thermogravimetric and calorimetric profiles of the as-synthesized reevesite samples with Ni/Fe ratios 1:1 and 0.5:1 in air and derivative of the weight loss.....	81
Figure 3.3. Transmission electron micrographs of calcined and reacted samples with Ni/Fe ratios 1:1 and 0.5:1.....	81
Figure 3.4. H ₂ -TPR profiles of the NiFe-C and Ni _{0.5} Fe-C samples.....	82
Figure 3.5. Ethanol conversion and selectivity to the different products vs time during ethanol steam reforming over calcined samples with Ni/Fe ratios 1:1 and 0.5:1.....	84
Figure 3.6. XRD patterns of NiFe and Ni _{0.5} Fe samples after reaction.....	86
Figure 3.7. Raman spectra of NiFe and Ni _{0.5} Fe samples after reaction.....	88
Figure 3.8. Ethanol conversion and selectivity to the different products vs time during ethanol steam reforming over NiFe-C at different temperatures.....	91
Figure 3.9. XRD patterns of the NiFe-C sample after reaction for 24 h at different temperatures (T=400°C, T=500°C and T=600°C, left) and after reaction for 3 h at 400°C (right).....	92
Figure 3.10. Transmission electron micrographs of the NiFe-U sample after reaction at different temperatures. The scale bar applies to all micrographs.....	94
Figure 4.1. XRD patterns of precursors and samples calcined at 723 K.....	107
Figure 4.2. Thermogravimetric and calorimetric profiles of the Ni ₃ Al _{1-x} Fe _x precursors in air and derivative of the weight loss.....	108
Figure 4.3. Raman spectra of the Ni ₃ Al _{1-x} Fe _x oxides obtained upon calcination at 723 K.....	111
Figure 4.4. H ₂ -TPR profiles of the Ni ₃ Al _{1-x} Fe _x oxides.....	111
Figure 4.5. Ethanol conversion and selectivity to the different products vs time during ethanol steam reforming over Ni ₃ Al _{1-x} Fe _x samples calcined at 723 K.....	115
Figure 4.6. Ethanol conversion and selectivity to the different products vs the degree of aluminum replacement by iron in the Ni ₃ Al _{1-x} Fe _x catalysts.....	117
Figure 4.7. Ethanol conversion and selectivity to the different products vs time during ethanol steam reforming at different temperatures over Ni ₃ Al _{0.8} Fe _{0.2} calcined at 723 K.....	119
Figure 4.8. XRD patterns of the used Ni ₃ Al _{1-x} Fe _x samples.....	121
Figure 4.9. TEM of the Ni ₃ Al _{1-x} Fe _x samples after 90 h-ESR.....	123
Figure 4.S1. Observed, calculated and difference diffractograms obtained with TOPAS software for the sample Ni ₃ Al _{0.8} Fe _{0.2} -U with Ni and a model for non-crystalline carbon used in the quantitative PONCKS method.....	129

List of Tables:

Table 2.1. Characterization data of the as-synthesized reevesites.....	33
Table 2.2: Characterization data of the calcined reevesites.....	37
Table 2.3: Characterization data of the used catalysts and average carbon balance during the reforming experiments.....	46
Table 3.1: Crystalline phase composition of the different catalysts.....	79
Table 3.2: Average crystallite size of the different catalysts.....	88
Table 4.1. Characterization data of the as-synthesized catalysts.....	106
Table 4.2. Characterization data of the calcined and used catalysts.....	112

Chapter 1

Introduction and overview

1.1. Hydrogen as an energy carrier

Today's world economy is significantly dependent on hydrocarbons since more than 80% of the primary energy consumed worldwide is obtained from fossil fuels [1]. This situation has several major drawbacks such as a high level of environmental pollution during mining, processing and burning of mineral fuels (particularly carbon dioxide emissions), limited long-term availability, and a tendency to rising costs. These factors have favored a widespread tendency to use renewable energy sources to supply part of the demand of primary energy. Among renewable energy sources like wind, solar, hydropower or biomass, the latter is appealing because it may be converted into liquid biofuels like alcohols, which may be used as chemical intermediates to store energy. Ethanol, for instance, is currently being used as fuel in conventional cars blended with gasoline, and it is an excellent energy storage molecule to produce hydrogen for fuel-cell vehicles [2]. It is known that the electricity generation and automotive sector are main responsible contributors for man-made greenhouse gas emissions [3]; for example, in USA in 2012, 32% and 28% of that type of air pollution came from power plants and transportation, respectively [4]. In fact, the main use of oil is for the production of liquid fuels for transportation, and nowadays more than 80% of world's transportation fuels (air, land and sea) are derived from oil [5]. Socioeconomic implications of biomass are also important, since its widespread use could contribute to improve the economy of developing countries [6], although care has to be taken to avoid interferences with the use of land for food production..

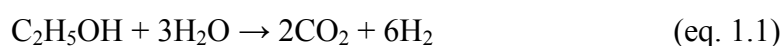
Hydrogen is one of the widespread elements in universe and on earth surface; it has the biggest specific heat of combustion and during the process of burning or using it in fuel cell, it produces water with CO₂ net emissions when it is produced from non-fossil fuels [7]. It exhibits a much higher energy density by weight (at least 3 times more than gasoline when compressed or liquefied [8]), but the problem of its effective and safe storage is under investigation. It is important to note that when hydrogen is used in power trains based on fuel

cells and electric motors, it is around 1.6 times more efficient than internal combustion engines (theoretical maximum for heat engine is 60% and ~95% for fuel cell) [9-11]. All these advantages are promoting hydrogen as a fuel alternative for the near future. In fact, it is already used in commercially made automobiles, buses, and even in military submarines [12-14].

Hydrogen can be produced from a broad variety of primary energy sources. Around 50% is currently being made by steam reforming of natural gas and light hydrocarbons, while the rest is obtained from heavy oil and coal by gasification or partial oxidation (45%) [6,15], and a variety of processes such as water electrolysis, biomass conversion (pyrolysis, gasification, steam reforming), and through enzymatic/bacterial processes (direct and indirect photolysis, photo-fermentation, and dark-fermentation) [16, 17]. However, the production of hydrogen from fossil sources is not attractive because of the associated CO₂ emissions. Electrolysis of water produces extremely pure hydrogen (smaller purification cost for fuel cell in comparison to other processes) and requires a simple reactor setup, but this way is hindered by high electricity consumption [18]. Biomass pyrolysis' main disadvantage is that this process produces large variety of gaseous and liquid by-products, which require to be separated. Biological methods of hydrogen production are relatively slow and usually need to work at low hydrogen partial pressure to accelerate reaction [16].

1.2. Hydrogen from ethanol

The production of hydrogen from renewable sources can be achieved through several pathways. One of the most promising is the production of bioethanol from biomass, which can be easily stored and commercialized with low CO₂ emissions, combined with the production of hydrogen from bioethanol [19]. Hydrogen can be produced from bioethanol through the catalytic steam reforming reaction (ESR):



This reaction exhibits the additional advantage of being almost CO₂ neutral, as most of the CO₂ released into the atmosphere is captured by the growth of biomass [16]. Bioethanol is also attractive since it can serve as safe hydrogen storing liquid for application in fuel processors described elsewhere [21]. Works of Brown [22] and Xuan [23] show the analysis of the ESR for automotive propulsion. It is considered as one of the promising energy supply systems in the future. As illustration, well to wheel analysis made by Campanari [24] and successful testing made Bowers in project of Renault&Nuvera Fuel Cells concludes that such appliances can be economically feasible [25].

In Figure 1.1., the process flow diagram of a fuel processor based on SCWR directly coupled to a PEMFC unit is depicted.

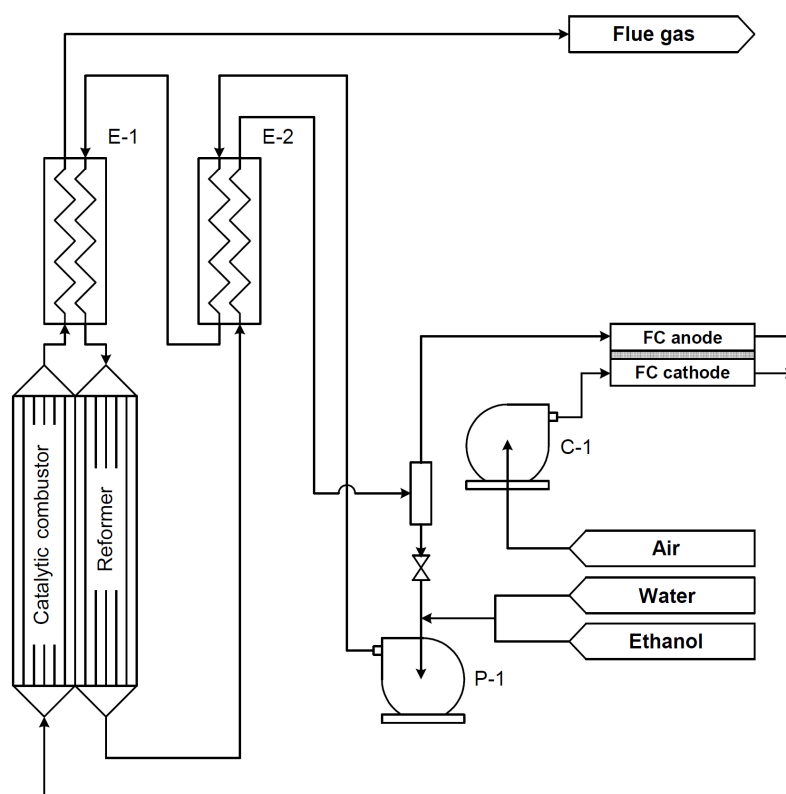


Figure 1.1. Process flow diagram of a fuel processor based on SCWR directly coupled to a PEMFC unit.

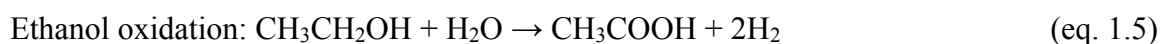
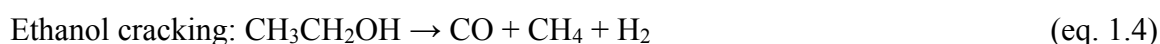
The fuel processor is composed of the reformer and the catalytic burner reactors, which are coupled directly to optimize heat transfer. Heat recovery between streams is performed in series of plate-type heat exchangers (E-1 to E-2). The product gas is cooled and the excess steam condensed and reused, and the water-saturated gas mixture of hydrogen, carbon dioxide and traces of methane is then sent to the fuel cell anode. The spent gas from the anode contains unreacted hydrogen and methane, and it is used as fuel in the burner of the reformer.

1.3. Catalysts for the steam reforming of ethanol

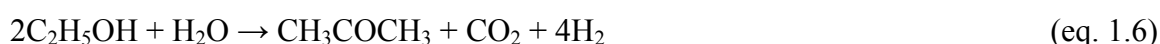
Ethanol steam reforming process can be performed over several families of catalysts. The most usual catalysts are based on non-noble transition metals supported on single metal oxides or mixed oxides [26]. The most frequently used metals are nickel, cobalt, iron and their different mutual combinations with metal oxides [27]. Haryanto et al. [28] also states that blank metal oxides can be used as ethanol steam reforming catalysts, for example pure ZnO, which can completely convert ethanol with significant selectivity to hydrogen, but the catalyst stability was not considered there. Such acidic oxides like Al₂O₃ or V₂O₅ are able to convert ethanol, but with really small hydrogen selectivity.

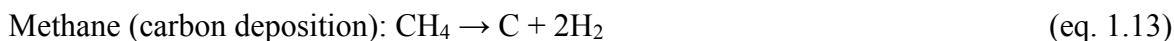
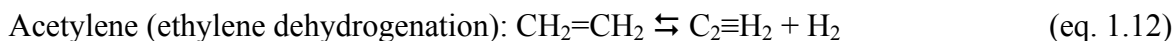
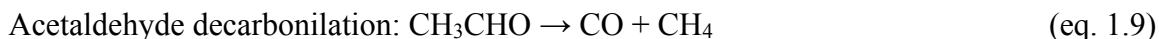
In general, the overall reaction pathway can be described through a set of simultaneous reactions.

Decomposition reactions:

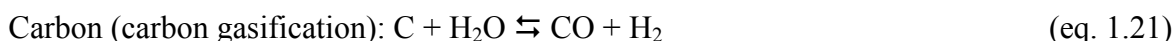
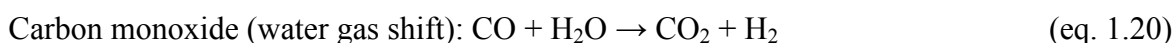


Aldolic condensation, followed by dehydrogenation:





Steam reforming reactions:



Other reactions:



The reaction mechanism depends on catalyst type and reaction conditions, but it is possible to deduce several regular trends. Work by Vicente et al. [29] shows that the general route for hydrogen production starts from ethanol dehydrogenation to acetaldehyde (eq. 1.2), followed by its transformation by steam reforming reactions (eq. 1.17-1.18). At favorable reaction conditions it is possible to observe direct steam reforming of ethanol as well (eq. 1.15-1.16). Also some by-products can react and contribute to the total yield of hydrogen: water gas shift (eq. 1.20), methane reforming (eq. 1.19, 1.22), and the gasification of carbon deposits (eq. 1.21).

Possible side-reactions can be summarized as ethanol cracking/decomposition (eq. 1.4) with the release of methane and carbon monoxide; decarbonilation of acetaldehyde (eq. 1.9); ethylene formation through ethanol dehydration (eq. 1.3) with the subsequent formation of coke by ethylene polymerization (eq. 1.10-1.12); ethanol oxidation to acetic acid and hydrogen (eq. 1.5); aldolic condensation to form acetone (eq. 1.6-1.8); carbon deposition (eq. 1.13-1.14); and other side-reactions like methanation (eq. 1.23-1.24) [29].

One of the main challenges to overcome in our process is catalyst stability, which is usually connected to carbon deposition with subsequent blocking of active sites and as result, catalyst deactivation. There are several works describing the type of carbon deposits formed under different reaction conditions. According to Xu et al. [30] carbon forms from ethoxy- and methyl- groups adsorbed on the catalyst surface, a process that is favored at low water coverage (low steam to carbon ratio) and is relatively fast. A higher partial pressure of steam induces carbon gasification (eq. 1.21) thus cleaning the catalyst surface. The above-mentioned work by Vicente et al. [29] observed three general types of carbon depositions on their Ni/SiO₂ catalyst. The first kind of coke dominates at reaction temperatures close to 300°C, it is an amorphous and highly reactive encapsulating coke; its precursors are presumably ethylene, acetaldehyde and acetone (through aldolic condensation (eq. 1.6-1.8)). The second type (filaments or “whiskers”) is observed mainly in the range 400-500°C, and evolves through the Boudouard reaction (eq. 1.14) and methane cracking (eq. 1.13). Meanwhile, the amount of carbon relatively decreases with temperature till 600°C, and shifts further to more graphitic and condensed form. The accumulation of filamentous coke did not significantly diminish the activity of the catalyst compared to other types of carbon, but this observation was made after a relatively short time on stream, which means that there is a possibility that the carbon filaments could destroy the porous structure of the catalyst after enough time on stream with their continuous growth. Lima da Silva et al. [31] studied the influence of contact time on coke formation. It was concluded that at low contact times, ethanol is generally

converted to ethylene with subsequent carbon formation, and this process is not affected by the steam to carbon ratio. On the contrary, at high contact times, carbon generation was suppressed and could be influenced by the steam/ethanol value. The work by Mas et al. [32] was in agreement with the above observations, and concluded that at low contact times it was possible to obtain significant amounts of acetaldehyde aside from ethylene. Also their results indicated that if moderate temperatures are used (no more than 450-500°C), steam to carbon ratio higher than 3 was required to avoid coke formation. Lee and Papadias [33-34] described the influence of pressure on carbon formation. An increase in pressure led to a decreased hydrogen production coupled to an increased methane formation, and a higher amount of deposited carbon.

1.3.1 Noble-metal catalysts

Ni et al. [27] showed that the catalysts most stable and selective for hydrogen production are noble metal based catalysts (mainly Rh and Ru) supported on metal-oxides like Al₂O₃, La₂O₃, CeO or MgO. These systems are quite active and selective to hydrogen even at 400°C with relatively low metal loading – from 0.5% to 5% [35-37]. The support materials also play a very important role not only because of their typical high surface areas and proper dispersion of metal particles, but because of their chemical nature. For example, Haryanto et al. [28] and Toth et al. [38] observed that Rh supported on gamma alumina (γ -Al₂O₃) suffered from coke accumulation and deactivation due to ethylene formation on the acidic sites of the aluminum oxide. The works by Aupretre et al. [39] and Wu et al. [40] stated that the activity of 1% Rh deposited on different supports decreased in the order Rh/Y₂O₃ > Rh/CeO₂ > Rh/La₂O₃ > Rh/Al₂O₃ at T = 650-800°C. Also it was found that Rh is a poor candidate for water gas shift reaction and that the presence of ZrO₂ doped with CeO₂ improved the CO₂ selectivity in the mentioned Rh-based series. The activity for Pt was investigated by He et al. [41], who observed that 1% weight load of platinum at T = 350°C

followed the sequence of decreasing activity $\text{Pt/CeO}_2 > \text{Pt/ZrO}_2 > \text{Pt/TiO}_2 \sim \text{Pt/C}$. Taking into account ethanol conversion and hydrogen selectivity, Liguras et al. [42] established the following metal order: $\text{Rh} \gg \text{Pt} > \text{Pd} > \text{Ru}$, when these metals were supported on $\gamma\text{-Al}_2\text{O}_3$ at different temperatures. However, Basagiannis et al. [34] observed that at a temperature range of 300–450°C and using $\gamma\text{-Al}_2\text{O}_3$ as support, the catalytic performance varied in the order of $\text{Pt} > \text{Pd} > \text{Rh} > \text{Ru}$, with Pt exhibiting high activity and selectivity toward hydrogen production, as well as long term stability at low temperature. Bimetallic noble systems were also investigated, as an example, Lopez et al. [43] tested 0.5%Rh-0.5%Pd over CeO_2 with almost complete ethanol conversion at $T > 427^\circ\text{C}$ and no generation of by-products. After 75 h on stream, deactivation of the catalyst was observed, which could be completely reverted by oxidation; this means that such system has good mechanical stability. Cobo et al. [44] also demonstrated synergetic effects upon combination of two noble metals, i.e. RhPt deposited on La_2O_3 which also showed good selectivity to H_2 and fine long-term performance.

One of the major drawbacks of noble metals-based catalytic systems is their high cost - it can be roughly 500-1000 times higher than for example, iron group metals even with relatively small metal loadings, thus making their industrial-scale application quite limited.

1.3.2 Cobalt-based catalysts

There are numerous works that use cobalt on different metal oxides supports. For example, Haga et al. [45] used cobalt with 7% (wt.) loading impregnated on SiO_2 , MgO , ZrO_2 and Al_2O_3 , the latter support material giving the catalyst with the highest selectivity to hydrogen (~70%) at complete ethanol conversion. Llorca et al. [47] however concluded an opposite behavior – 1% (wt.) cobalt impregnated on alumina demonstrated quite low hydrogen selectivity (~0%), but ethanol conversion was 100% and ethylene was one of the main products. Therefore, it appears that metal loading is also playing a crucial role on the catalyst effectiveness.

Another study related to the influence of the support was conducted by Song et al. [48]. His team investigated Co deposited on Al₂O₃, TiO₂, ZrO₂ (10% weight load in each case) and found that the reaction over Co/ZrO₂ showed the best catalytic activity: a total conversion and maximum H₂ yield were obtained at 550°C. Finally it was possible to classify these systems in the following way: Co/ZrO₂ > Co/Al₂O₃ ≥ Co/TiO₂. Llorca et al. [46] also prepared Co catalysts with several supports (ZnO, MgO, γ-Al₂O₃, SiO₂-TiO₂, V₂O₅, La₂O₃, CeO₂, and Sm₂O₃) and found that the Co/ZnO catalyst showed the best catalytic performance. This catalyst showed total conversion and 42% of H₂ selectivity at 450°C after 50 h. Ethanol steam reforming also occurred to a large degree over La₂O₃-, Sm₂O₃-, and CeO₂-supported catalysts and CO-free hydrogen was produced. Batista et al. [49] analyzed Co/Al₂O₃, Co/SiO₂, and Co/MgO catalysts. High conversion levels (>90%) were observed for the steam reforming of ethanol in all catalysts. In the case of Co/Al₂O₃ a significant amount of ethylene was detected in the gaseous stream, Co/SiO₂ gave the highest quantity of methane and Co/MgO the highest amount of CO. A considerable amount of carbon was deposited in all catalysts after 8–9 h of reaction, the largest being for Co/Al₂O₃.

The catalyst preparation method is also an important aspect because it influences the interaction between cobalt and its support. Thus, Wang et al. [50] showed that in comparison with catalysts prepared by impregnation, more cobalt ions entered into CeO₂ lattice when the catalyst was prepared by a co-precipitation method, which resulted in weaker interactions between the active phase and ceria on the surface of Co₃O₄/CeO₂. Hence, cobalt oxides derived from co-precipitated catalysts were more reducible, and metallic cobalt was the key active component. Another aspect related to the preparation method is the selection of the solvent. Song et al. [51] observed that the Co/CeO₂ catalysts prepared in ethanol medium showed significant improvements in catalytic performance (higher H₂ yield, higher stability and fewer side reactions), compared to those prepared in aqueous media. Characterization

results showed the presence of oxygenated carbon species, possibly metal-coordinated acetates, on the surface.

It was also possible to use the synergistic effect of several supporting materials, as an example, Lin et al. [52] used a combination of ZrO_2 and CeO_2 to promote the performance of the catalytic system. The $Co/CeZrO_4$ catalysts showed higher activity to produce H_2 than Co/ZrO_2 , which produced CH_4 . Co/CeO_2 gave high H_2 selectivity while suffered low conversion due to the poor thermal stability. In contrast to CeO_2 , Co/ZrO_2 achieved high conversion but attained lower H_2 yield due to the production of methane.

One of the ways to improve the performance of certain catalytic systems is to add a promoting metal (basically they are taken from the alkaline metal group [47], [53]). In case of cobalt containing catalysts, Llorca et al. [47] described that the addition of 1% wt. of sodium significantly improved ethanol conversion and selectivity, and the catalyst was completely free of carbon deposits in comparison to pure Co/ZnO system. Cobalt, however, is less active than nickel on the same support materials because it tends to sinter and oxidize during ESR reaction [54], and it is less able to break C-C bonds [55]. Iron also can serve as promoter for cobalt containing catalysts, for example a 0.22% wt. iron load supported on Al_2O_3 and SiO_2 increased the conversion at $550^\circ C$ from 10 to 30%, depending on reaction time. Hydrogen selectivity also increased almost the same percentage, carbon amount dropped significantly after similar reaction time [56, 64].

1.3.3 Nickel-based catalysts

One of the metals most used for steam reforming catalysts is nickel. In a review by Ni et al. [33] nickel was identified as a widely used low-cost metal catalyst for ethanol reforming, since it favors the rupture of C-C bonds. Sun et al. [57] described nickel supported on Ni/Y_2O_3 , Ni/La_2O_3 and Ni/Al_2O_3 , the former being the most active (showing 100% conversion even at $320^\circ C$) and selective; however, the space velocity (GHSV) was at least

100 times smaller than usual. Then, Comas et al. [58] dealt with Ni supported on γ -alumina, and the authors claimed that the main reaction path below 400°C was ethanol cracking, but above 500°C, steam reforming was more significant. In the same work, no evidences for the water-gas shift reaction were encountered. Ethanol conversion was 100% even at 300°C, and the hydrogen selectivity rose from 40% at 300°C to 60% at 500°C. Yang et al. [59] demonstrated that among La_2O_3 , MgO Al_2O_3 and ZnO , the latter was the best support for the nickel-supported catalyst, reaching total conversion at 330°C, but hydrogen selectivity was 45% at 500°C, and 90% at 650°C. In general, depending on the support, steam to carbon ratio and nickel loading, it was possible to achieve complete conversion of ethanol at 400°C with relatively high hydrogen yields (up to 70%) [60-61]. The main problem for this metal is the fast deactivation caused by nickel sintering and carbon deposition [62]. These obstacles can be partially avoided when adding some promoters like alkali metals or lanthanides (La, Ce, etc.) [63]. The addition of these promoters causes inhibition of carbon formation up to 70%, stabilize the catalytic system, and concomitantly increase the hydrogen yield [64].

Another option to improve the ESR performance is to combine the properties of several active metals in one homogeneous catalytic system. For example, a nickel-containing spinel was tested in ESR reaction [65]. Such a catalyst consisted of a binary mixture of ZnAl_2O_4 and NiAl_2O_4 spinels with different metal ratios, where the nickel content was in the range from 0 to 25 wt.% All catalysts displayed 100% ethanol conversion, but the hydrogen selectivity was half when the Ni loading was below 8 wt.%, with a higher amount of undesirable gases in the product stream (such as C_3H_6 , C_2H_4). The combination of appropriate metals with Ni has been widely investigated to obtain higher steam reforming activity and higher selectivity to hydrogen. In this direction, the concept of using Ni-based bimetallic catalysts with good dispersion of the components is gaining more insights to increase both hydrogen yields and catalyst stability. A prominent route to achieve this type of homogeneous

materials is the synthesis of layered double hydroxides (LDHs), or hydrotalcite-like compounds [66]. Their typical structure is shown in Figure 1.2 [67].

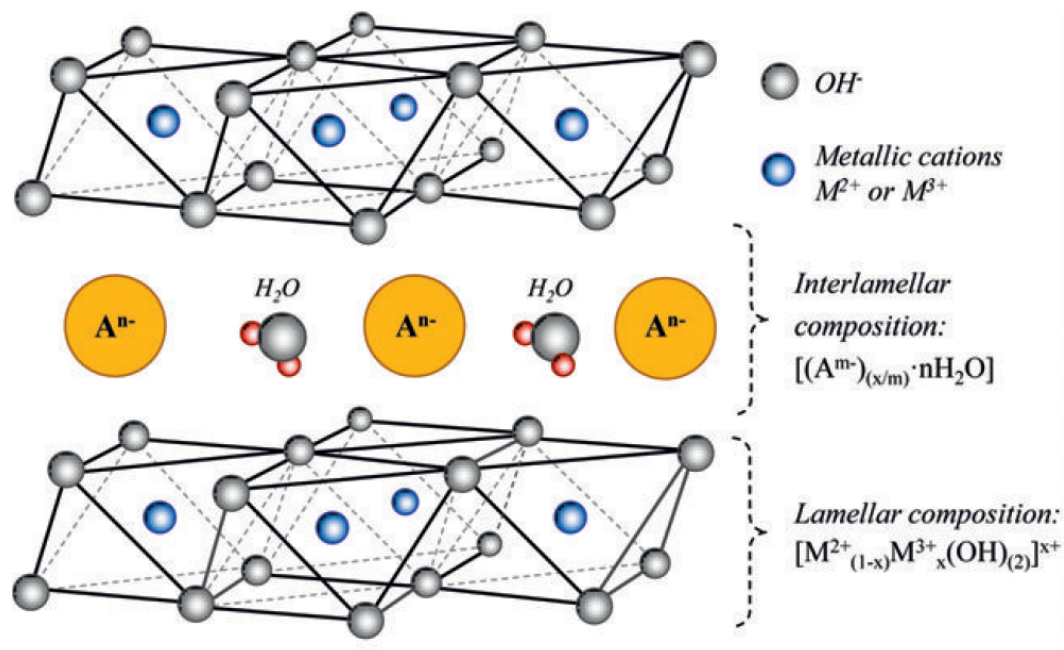


Figure 1.2. General structure of hydrotalcites

According to Trifiro et al. [68], hydrotalcite-based materials are simple and inexpensive to synthesize at laboratory and industrial scale. Forano et al. [69] described the large variety of methods for the preparation of LDHs, but the coprecipitation method is often selected by the easiness, rapidity and low cost to obtain multimetallic catalysts for different applications. Typically, the coprecipitation method at constant pH is the most relevant in terms of high homogeneity, small particle size and high specific surface area of the derived materials [70].

Resini et al. [71] showed that calcination of this type of precursors gave rise to high surface area mixed oxides which essentially retained the lamellar morphology of the precursors. The chemical and structural nature of the resulting materials depended on the initial cations in the LDH structure; as an example, while the mixed oxides obtained from Ni–Zn–Al LDHs were definitely polyphasic, being actually a mixture of a rock salt phase (NiO), a wurtzite phase (ZnO) and a spinel phase (likely mostly ZnAl₂O₄), the mixed oxides obtained

from Ni–Mg–Al LDHs were essentially monophasic, being mostly constituted by a rock salt NiO–MgO solid solution at low calcination temperatures.

Therefore, the calcination temperature significantly affects the properties and activity of the derived catalysts: Yi et al. [72] demonstrated that there is an optimum activation temperature range where the layered and pore structure of the system is retained. The Zn–Ni–Al hydrotalcites were calcined at 250°C, 300°C, 350°C, 400°C and 500°C and XRD results showed that when they were calcined at high temperatures, their layered structures were destroyed and the derived mixed oxides were obtained.

Typically, higher calcination temperature leads to structure collapse and disintegration, gradual growth of mixed oxides (and consequently, larger crystallite sizes), and undesirable chemical nature change – high crystallite size spinel formation [73]. Holgado's work [74] showed that the solids were formed by NiO and NiFe₂O₄ (spinel) and the crystallite size was larger for the spinel crystallites than for the NiO crystallites. In all cases, the crystallite size had a dependence upon the surfactant used and pH during the synthesis.

Romero et al. [75] investigated the effect of the Ni(II)–Mg(II)–Al(III) layered double hydroxide (LDH) activation conditions over the surface and bulk composition and the catalytic performance in ethanol steam reforming (ESR). The catalyst precursor was submitted to calcination at 400, 500, 600 and 700°C with subsequent reduction at 720°C, or direct reduction at 720°C. Calcination in air of a Ni(II)-rich LDHs developed a Ni(II)-poor spinel-type shell onto the NiO domains, evidenced by an increase in the surface Al(III) concentration. Also, the surface area increased as temperature raised until a maximum close to 400°C, and then a further increase in the calcination temperature produced a diminution of surface area. The reductive treatment resulted in an almost quantitative transformation of the NiO phase into Ni metallic crystallites highly dispersed in a stable Mg(II)–Al(III) matrix. The TPR maximum shifts to higher temperatures as well as the calcination temperature increases.

This was related to a higher interaction between nickel atoms and the neighboring cations. It can be seen that the application of an appropriated activation treatment would allow controlling the interaction of the Ni⁰ active centers with the environment and the solid texture, redounding in an improved activity. As result, the catalysts obtained by calcination at 600°C and then reduction at 720°C and those directly reduced at 720°C showed the better performance in ESR.

Coleman et al. [76] demonstrated that the calcination of Ni-Mg-Al LDH was an interesting method to obtain catalytic materials for ethanol steam reforming with desirable properties. In his catalytic system, the improved performance of the mixed oxide supported catalysts was related to the inclusion of the pure oxides, MgO and Al₂O₃, into MgAl₂O₄ phase. The formation of MgAl₂O₄ reduced nickel incorporation onto the support material since MgAl₂O₄ does not reacted with Ni. Therefore, nickel was retained in its active form. In addition, addition of Mg and Al into MgAl₂O₄, a slightly basic material, modified the acid–base properties resulting in a catalyst that exhibited moderate acidic and basic site strength compared to the pure oxide supported catalysts.

Marifio et al. [77] observed two different phenomena occurring during the calcination stage in Cu/Ni/K/γ-Al₂O₃ materials with a copper loading higher than 4 wt%: a) the growth of CuO crystallites, and b) the increase of the copper-support interaction, producing a surface spinel phase. This phase had catalytic properties that counterbalanced the loss of activity due to the first phenomena. On the other hand, for catalysts with a copper loading lower than 4 wt.%, an amorphous and highly dispersed CuO phase was produced, which was not detected by X-ray diffraction, whatever the calcination temperature. When the calcination temperature increased, the high dispersion of CuO particles avoided their growth and favored the diffusion of copper ions into the alumina matrix. Then, a bulk spinel without catalytic properties was produced.

Focusing on ESR, various Ni-based hydrotalcites have been prepared by multiple metal combinations of Ni–Al, Ni–Mg–Al, Ni–Zn–Al, Ni–Co–Zn–Al, Ni–Co–Mg–Al, Ni–Mg–Al–Fe, Ni–Ca–Al, Ni–Cu–Mg–Al, Mg–Zn–Al, Ni/Mg–Zn–Al, La–Ni–Mg–Al, Ce–Ni–Mg–Al, Cu–Ni–Zn–Al, Cu–Ni–Al [78-79, 81-83]. Elementary catalytic systems like takovite (the Ni–Al hydrotalcite) have been investigated in the literature, and have exhibited a boosted performance with respect to conventional Ni/Al₂O₃ prepared by impregnation [80]. Although this route enables a high dispersion of nickel crystallites upon calcination and reduction, alumina favors ethanol dehydration over its acidic sites, thus leading to coke formation. On the other hand, metals like iron have not been much investigated. Iron is used as doping metal, and behaves as a very fruitful booster for the reaction in certain systems [64]. As previously stated [62], iron is an active metal for water–gas-shift (increasing the ratio of CO₂ to CO), reduces carbon deposition, enhances the dispersion of active metals, and increases hydrogen yields. Following a coprecipitation route, Muroyama et al. [84] described the preparation of a Ni–Fe-based spinel for ethanol steam reforming. This catalyst was synthesized by coprecipitation and calcination at 900°C. The catalyst showed high ethanol conversion even at 400°C, and 50% hydrogen selectivity. However, the catalyst stability was relatively poor due to carbon deposition.

Taking into account the versatile route to obtain mixed oxides derived from hydrotalcites, we decided to investigate other Ni-based combinations based on hydrotalcite-like compounds for ethanol steam reforming, able to overcome the negative aspects intrinsic to this reaction like deactivation by sintering or carbon deposition typically found over Ni catalysts.

1.3.4 Aim and overview of the Thesis

The work described in this thesis focuses on the synthesis of multimetallic Ni-based hydrotalcite-type compounds, using iron, aluminum or mixtures thereof for enhanced

hydrogen production via ethanol steam reforming. The ultimate goal is to study the effect of various trivalent cations in the hydrotalcite structure, i.e. iron, and aluminum, to finally achieve an active, selective and stable mixed oxide catalyst for the reaction. Major attention is paid to the composition of the Ni-based hydrotalcite-like compounds in order to attain catalysts with remarkable activity. The effect of iron content, activation conditions, temperature of the reaction, and the presence of a third metal has been evaluated.

In chapter 2 the preparation of the Ni-Fe hydrotalcite precursors is discussed and the effect of the calcination temperature (500°C and 800°C) together with the influence of Ni/Fe ratio (from 3:1 to 1:1 molar) on ethanol steam reforming reaction was studied. Chapter 3 extends the study to account for the influence of reaction temperature (at 400°C, 500°C and 600°C) and further increase of the iron content till ratio 0.5:1. Finally, Chapter 4 studies the influence of a third metal (aluminum) in the system and investigates long-term catalytic testing, up to 120 hours of reaction.

1.4. References:

- [1] Energy in Sweden 2010, Facts and figures. Table 46: Total world energy supply, 1990–2009. <http://www.se.ro/Filer/Startsidan/ET201046.pdf>
- [2] N. Muradov, T. Veziroglu. *Int. J. Hydrogen Energy* 33 (2008) 6804–6839.
- [3] M. Raupach, G. Marland, P. Ciais, C. Le Quéré, J. Canadell, G. Klepper and C. Field. Global and regional drivers of accelerating CO₂ emissions. *PNAS*, 104 (2007) 10288–10293.
- [4] National greenhouse gas emissions data. Inventory of U.S. Greenhouse Gas Emissions and Sinks: 1990–2012 (April 2014).
<http://www.epa.gov/climatechange/ghgemissions/usinventoryreport.html>
- [5] Alternative Transport Fuels. World Petroleum Council 2009.
<http://www.world-petroleum.org/index.php?/Technology/alternative-transport-fuels-courtesy-of-aip.html>
- [6] M. Balat, M. Balat. *Int. J. Hydrogen Energy* 34 (2009) 3589–3603.
- [7] M. Momirlan, T. Veziroglu. *Int. J. Hydrogen Energy* 30 (2005) 795 – 802.
- [8] Alternative Fuels Data Center Report. 27 February 2013.
http://www.afdc.energy.gov/fuels/fuel_comparison_chart.pdf
- [9] Fuel Cells Versus Heat Engines: A Perspective of Thermodynamic and Production Efficiencies. Micropyretics Heaters International Inc.
<http://www.mhi-inc.com/PG2/Fuel%20Cells%20Versus%20Heat%20Engines.pdf>
- [10] Robert J. Farrauto. *Stud. Surf. Sci. Catal.* 145 (2003) 21-29.
- [11] Specifications for Honda FCX Clarity. American Honda Motor Co., Inc.
<http://automobiles.honda.com/fcx-clarity/specifications.aspx?group=epa>
- [12] News. Third fuel cell submarine handed to German navy. *Fuel Cells Bulletin* 6, (2006) Page 10.
- [13] K. Haraldsson, A. Folkesson, P. Alvfors. *J. Power Sources* 145 (2005) 620–631.
- [14] R.J. Pearson, J.W.G. Turner. 5.16 - Renewable Fuels: An Automotive Perspective. *Comprehensive Renewable Energy* 5 (2012) 305-342.
- [15] H. Balat, E. Kirtay. *Int. J. Hydrogen Energy* 35 (2010) 7416-7426.
- [16] D. Levin, R. Chahine. *Int. J. Hydrogen Energy* 35 (2010) 4962–4969
- [17] I. Ray, T. Chakraborty, D. Roy, A. Datta, B. Mandal. *Journal of Emerging Technology and Advanced Engineering*. 3, Special Issue: ICERTSD, (2013) 119-125.
- [18] K. Zeng, D. Zhang. *Prog. Energy Combust. Sci.* 36 (2010) 307–326.
- [19] M. Winther, F. Møller, T. Jensen. *Atmos. Environ.* 55 (2012) 144-153.
- [20] A. Baddeley, A. Ballinger, D. Hogg. Comparative life-cycle assessment. Seal sands waste to biofuel initial plant. INEOS Bio Ltd. (2010)
- [21] D. Montané, E. Bolshak, S. Abelló. *Chem. Eng. J.* 175 (2001) 519-533.
- [22] L. Brown. *Int. J. Hydrogen Energy* 26 (2001) 381–397.

- [23] J. Xuan, M. Leung, D. Leung, M. Ni. *Renewable Sustainable Energy Rev.* 13 (2009) 1301–1313.
- [24] S. Campanari, G. Manzolini, F. de la Iglesia. *J. Power Sources* 186 (2009) 464–477.
- [25] B. Bowers, J. Zhao, M. Ruffo, R. Khan, D. Dattatraya, N. Dushman, J.-C. Beziat, F. Boudjema. *Int. J. Hydrogen Energy* 32 (2007) 1437 – 1442.
- [26] R. Trane, S. Dahl, M.S. Skjøth-Rasmussen, A.D. Jensen. *Int. J. Hydrogen Energy* 37 (2012) 6447-6472.
- [27] M. Ni, D. Leung, M. Leung. *Int. J. Hydrogen Energy* 32 (2007) 3238 – 3247.
- [28] A. Haryanto, S. Fernando, N. Murali, and S. Adhikari. *Energy Fuels*, 19 (2005) 2098-2106.
- [29] J. Vicente, J. Erena, C. Montero, M. J. Azkoiti, J. Bilbao, A. G. Gayubo. *Int. J. Hydrogen Energy* 39 (2014) 18820-18834.
- [30] W. Xu, Z. Liu, A. Johnston-Peck, S. Senanayake, G. Zhou, D. Stacchiola, E. Stach, J. Rodriguez. *ACS Catal.* 3 (2013) 975–984.
- [31] A. Lima da Silva, C. Malfatti, I. Muller. *Int. J. Hydrogen Energy* 34 (2009) 4321 – 4330.
- [32] V. Mas, R. Kipreos, N. Amadeo, M. Laborde. *Int. J. Hydrogen Energy* 31 (2006) 21 – 28.
- [33] S. Lee, D. Papadias, R. Ahluwalia, S. Ahmed. *Steam Reforming of Ethanol at Elevated Pressures for Distributed Hydrogen Production. Alternative Fuels Data Center, US Department of Energy Report* (2006).
- [34] D. Papadias, S. Lee, M. Ferrandon, S. Ahmed. *Int. J. Hydrogen Energy* 35 (2010) 2004 – 2017.
- [35] A. Basagiannis, P. Panagiotopoulou, X. Verykios. *Top. Catal.* 51 (2008) 2-12.
- [36] A. Erdohelyi, J. Rasko, T. Kecskes, M. Toth, M. Domok, K. Baan. *Catal. Today* 116 (2006) 367–376.
- [37] F. Frusteri, S. Freni, L. Spadaro, V. Chiodo, G. Bonura, S. Donato, S. Cavallaro. *Catal. Commun.* 5 (2004) 611–615.
- [38] M. Toth, M. Domok, J. Raskox, A. Hancz, A. Erdohelyi. *Chemical Engineering Transactions* 4 (2004) 229.
- [39] F. Aupretre, C. Descorme, D. Duprez. *Catal. Commun.* 3 (2002) 263–267.
- [40] X. Wu, S. Kawi. *Energy Environmental Science* 3 (2010) 334–342.
- [41] Z. He, M. Yang, X. Wang, Z. Zhao, A. Duan. *Catal. Today* 194 (2012) 2-8.
- [42] D. Liguras, D. Kondarides, X. Verykios. *Appl. Catal., B.* 43 (2003) 355-369.
- [43] E. Lopez, N. Divins, A. Anzola, S. Schbib, D. Borio, J. Llorca. *Int. J. Hydrogen Energy* 38 (2013) 4418-4428.
- [44] M. Cobo, D. Pieruccini, R. Abello, L. Ariza, L.F. Cordoba, J.A. Conesa. *Int. J. Hydrogen Energy* 38 (2013) 5580-5593.
- [45] F. Haga, T. Nakajima, H. Miya, S. Mishima. *Catal. Lett.* 48 (1997) 223-227.
- [46] J. Llorca, N. Homs, J. Sales, and P. Ramirez de la Piscina. *J. Catal.* 209 (2002) 306–317.

- [47] J. Llorca, N. Homs, J. Sales, J.-L. Fierro and P. Ramírez de la Piscina. *J. Catal.* 222 (2004) 470–480.
- [48] H. Song, L. Zhang, R.B. Watson, D. Braden, U.S. Ozkan. *Catal. Today* 129 (2007) 346–354.
- [49] M. Batista, R. Santos, E. Assaf, J. Assaf, E. Ticianelli. *J. Power Sources* 124 (2003) 99–103.
- [50] H. Wang, J.L. Ye, Y. Liu, Y.D. Li, Y.N. Qin. *Catal. Today* 129 (2007) 305–312.
- [51] H. Song, U. Ozkan. *J. Mol. Catal. A: Chem.* 318 (2010) 21–29.
- [52] S.S.Y. Lin, D.H. Kim, S.Y. Ha. *Catal. Lett.* 122 (2008) 295–301.
- [53] F. Frusteri, S. Freni, V. Chiodo, L. Spadaro, O. Di Blasi, G. Bonura, S. Cavallaro. *Appl. Catal., A* 270 (2004) 1–7.
- [54] S. Freni, S. Cavallaro, N. Mondello, L. Spadaro, F. Frusteri. *Catal. Commun.*, 4 (2003) 259–268.
- [55] L. Chen, C. Choong, Z. Zhong, L. Huang, Z. Wang, J. Lin. *Int. J. Hydrogen Energy* 37 (2012) 16321–16332.
- [56] G. de Souza, V. Ávila, N. Marcílio, O. Perez-Lopez. *Procedia Eng.* 42 (2012) 1805 – 1815.
- [57] J. Sun, X. Qiu, F. Wu, W. Zhu. *Int. J. Hydrogen Energy* 30 (2005) 437 – 445.
- [58] J. Comas, F. Mariño, M. Laborde, N. Amadeo. *Chem. Eng. J.* 98 (2004) 61–68.
- [59] Y. Yang, J. Ma, F. Wu. *Int. J. Hydrogen Energy* 31 (2006) 877 – 882.
- [60] J. Bellido, E. Assaf. *J. Power Sources* 177 (2008) 24–32.
- [61] A. Denis, W. Grzegorzczak, W. Gac, A. Machocki. *Catal. Today* 137 (2008) 453–459.
- [62] S. Abelló, E. Bolshak, D. Montané. *Appl. Catal., A* 450 (2013) 261–274
- [63] M. Akiyama, Y. Oki, M. Nagai. *Catal. Today* 181 (2012) 4–13.
- [64] A. Kazama, Y. Sekine, K. Oyama, M. Matsukata, E. Kikuchi. *Appl. Catal., A* 383 (2010) 96–101.
- [65] M. Barroso, M. Gomez, L. Arrua, M. Abello. *Appl. Catal., A* 304 (2006) 116–123.
- [66] F. Cavani, F. Trifiro, A. Vaccari. *Catal. Today* 11 (1991) 173–301.
- [67] C.C. Arruda, P.H.L. Cardoso, I.M.M. Dias, R. Salomão. Hydrotalcite ($\text{Mg}_6\text{Al}_2(\text{OH})_{16}(\text{CO}_3)\cdot 4\text{H}_2\text{O}$): A Potentially Useful Raw Material for Refractories. *Interceram – Refractories Manual I/2013*, p. 187 - 191.
- [68] Trifiro, F., Vaccari, A., 1996. Hydrotalcite-like anionic clays (layered double hydroxides). In: Alberti, G., Bein, T. (Eds.), *Comprehensive Supramolecular Chemistry*, vol. 7. Elsevier, Oxford, pp. 251–291.
- [69] C. Forano, T. Hibino, F. Leroix, C. Taviot-Gueho. *Layered double hydroxides. Handbook of clay science*, 2006. Chapter 13.1, p. 1021.
- [70] M. Tu, J. Shen, Y. Chen. *Thermochim. Acta* 302 (1997) 117–124.
- [71] C. Resini, T. Montanari, L. Barattini, G. Ramis, G. Busca, S. Presto, P. Riani, R. Marazza, M. Sisani, F. Marmottini, U. Costantino. *Appl. Catal., A* 355 (2009) 83–93.

- [72] H. Yi, S. Zhao, X. Tang, P. Ning, H. Wang, D. He. *Catal. Commun.* 12 (2011) 1492–1495.
- [73] H. Cross, G. Parkes, D. Brown. *Appl. Catal., A* 429–430 (2012) 24–30.
- [74] P. Holgado, M. Holgado, M. San Román, V. Rivesn. *Ceram. Int.* 41 (2015) 8451–8460.
- [75] A. Romero, M. Jobbagy, M. Laborde, G. Baronetti, N. Amadeo. *Catal. Today* 149 (2010) 407–412.
- [76] L.J.I. Coleman, W. Epling, R.R. Hudgins, E. Croiset. *Appl. Catal., A* 363 (2009) 52–63.
- [77] F. Marifio, M. Jobbagy, G. Baronetti and M. Laborde. *Stud. Surf. Sci. Catal.* 130 2147-2152.
- [78] G. de Souza, V. Ávila, N. Marcílio, O. Perez-Lopez. *Procedia Eng.* 42 (2012) 1805 – 1815.
- [79] G. Zeng, Q.Liu, R. Gu, L. Zhang, Y. Li. *Catal. Today* 178 (2011) 206–213.
- [80] M. Lindo, A. Vizcaino, J. Calles, A. Carrero. *Int. J. Hydrogen Energy* 35 (2010) 5895 – 5901.
- [81] A.F. Lucrédio, J.D.A. Bellido, E.M. Assaf. *Appl. Catal., A* 388 (2010) 77–85.
- [82] S. Velu, K. Suzuki, M. Vijayaraj, S. Barman, C. Gopinath. *Appl. Catal., B* 55 (2005) 287-299.
- [83] F. Mariño G. Baronetti, M. Jobbagy, M. Laborde. *Appl. Catal., A* 238 (2003) 41–54.
- [84] H. Muroyama, R. Nakase, T. Matsui, K. Eguchi. *Int. J. Hydrogen Energy* 35 (2010) 1575 – 1581.

Chapter 2

Ni-Fe catalysts derived from hydrotalcite-like precursors for hydrogen production by ethanol steam reforming

Nickel-iron mixed oxides derived from reevesite, a hydrotalcite-type compound, were tested in steam reforming of ethanol for hydrogen production. The influence of iron content (Ni/Fe ranging from 3 to 1) and the calcination temperature of the catalyst precursor (773 and 1073 K) on the catalytic performance were investigated. Both parameters were essential to optimize the reforming performance. Increasing the amount of iron in the reevesite precursors affected both the chemical and activity properties of the derived mixed oxide catalysts. Iron displays a positive role in nickel-based catalysts due to the enhancement of catalytic activity and hydrogen selectivity induced by the improved dispersion of nickel and the alleviation in carbon deposition. The calcination temperature led to variations in phase composition consisting of Ni(Fe)O_x solid solution and NiFe₂O₄, which affected the final size and dispersion of nickel species formed during the reaction. The best catalyst, with a Ni/Fe ratio of 1 and calcined at 773 K, rendered high and stable hydrogen and carbon dioxide selectivity of up to ca. 60% and 40%, respectively, low methane content, and consisted of a Ni(Fe)O_x + NiFe₂O₄ mixture with high surface area and small Ni⁰ crystallites. A higher percentage of crystalline NiFe₂O₄ attained at high calcination temperature (1073 K) associated with a lower carbon deposition resistance and probably Ni⁰ sintering brings about lower activity and fast deactivation. The improved performance over catalysts calcined at lower temperature and with lower Ni/Fe ratio is motivated by the effect of iron on the structural and electronic properties of the mixed oxides, thus inducing a slow formation of metallic nickel particles and coke deposits. Features like high surface area, higher iron content, lower reducibility of nickel species and small nickel crystallite size well dispersed on the surface of the catalyst with high iron content lead to a higher activity in ethanol dehydrogenation, acetaldehyde decarbonylation and reforming, and WGS.

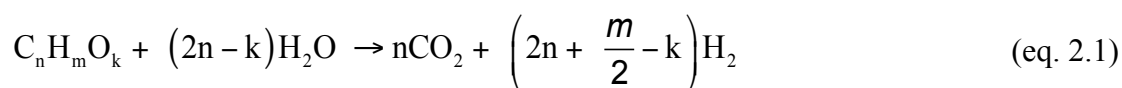
This chapter is based on the following publication:
S. Abelló, E. Bolshak, D. Montané, Appl. Catal. A 450 (2013) 261.

2.1. Introduction

Today, over 80% of world primary energy comes from three fossil fuels (petroleum, natural gas and coal) [1-3]. However, fossil fuel reserves are decreasing rapidly due to the continuous increased demand and they are not replaced as fast as they are consumed. Besides, about 98% of carbon emissions derive from fossil fuel combustion, thus, the damaging environmental effect of fossil fuel utilization is also crucial [4,5]. Therefore, the world's over-demand of energy, the crisis of fossil fuel depletion, the continuous increase in oil prices, and the environmental degradation have focused current efforts on the development of new and renewable fuel alternatives. Energy sources, like sun, wind, geothermal, hydraulic, nuclear, hydrogen, and biomass have been taken into consideration [4]. Among these options, solar, wind and biomass are promising but are generally site-specific and more sporadic [6]. In contrast, hydrogen is expected to play an important role in future energy scenarios [2,7].

At present, the catalytic steam reforming is the most mature and well-established technology for hydrogen production [8]. Particularly, half of the world's hydrogen production derives from the most cost-effective steam reforming of natural gas (also referred as methane steam reforming) [4,8,9]. However, natural gas is a fossil fuel and its utilization to produce hydrogen does contribute to greenhouse gas emissions [6] unless a carbon dioxide capture and sequestration process is implemented in the reforming plant. In this context, there is a growing interest in the search of renewable alternatives to produce hydrogen. Among the various feedstocks, ethanol is very attractive as it can be produced by fermentation of different sources like agricultural wastes, forestry residue materials, and organic fractions of municipal solid wastes, and additionally, it contributes to nearly net-zero CO₂ emissions [10]. From a research point of view, the steam reforming reaction is probably one of the most investigated processes for breaking C-C bonds in chemicals available from biomass [9].

Stoichiometrically, the overall steam reforming of an oxygenated compound with a generic chemical formula C_nH_mO_k follows the equation:



However, the final hydrogen productivity will depend on the state of the equilibrium of the water-gas-shift reaction (WGS), which occurs simultaneously to the steam reforming.



Notably, the steam reforming of ethanol (ESR) has been extensively examined [6,9,11,12]. Although the purpose of the reforming process is the production of as much H₂ and CO₂ as possible, depending on the catalyst used, the overall reaction is very complex and involves several non-selective pathways during the ESR process leading to acetaldehyde, methane, ethylene and other by-products formed in successive side reactions.

Oxide catalysts, metal-based catalysts (Ni, Co, Cu, Ni/Cu) and noble metal (Pd, Pt, Rh)-supported catalysts are promising for the reaction using high temperatures, low pressures and high water-to-ethanol ratios in the feed to favor hydrogen production [6,11,13]. The most effective metal for the ESR is rhodium, due to its greater activity towards C-C breaking, but its high price hinders its utilization in the process [14]. In contrast, nickel, which is comparatively less expensive, has been widely investigated and considered so far as one of the preferred active candidates for ESR due to its low cost and high activity in C-C and O-H rupture, and hydrogenation/dehydrogenation reactions, facilitating H atoms to form H₂ [12,15]. Two negative factors of metallic nickel are the high susceptibility to sinter and to form carbonaceous deposits in contact with hydrocarbons, thus leading to severe deactivation [9,16]. Besides, Ni exhibits a low WGS (thus reducing CO conversion into CO₂) and is also active in methanation reactions [6,17]. The formation of coke deposits can be minimized by addition of other metals as promoters [18], by modification of the surface properties of the active catalyst, and by the reduction of metal particle size [19], while the presence of additional metals can partially inhibit the sintering of Ni as well. In this direction, several studies deal with the preparation of Ni supported on a great variety of solids, i.e. MgO, Al₂O₃,

La₂O₃, ZnO, SBA-15, TiO₂, etc., and the addition of various promoters, i.e. Zr, La, Ce, Li, K, etc. [6,12]. In most cases, the presence of these promoters affected the acidity of the support and the morphology and structure of the Ni particles. The combination of appropriate metals with Ni leads to high steam reforming activity and high selectivity to hydrogen. For example, the addition of Cu over Ni-based catalysts favors dehydrogenation and WGS, thus enhancing the production of hydrogen due to synergetic effects between the metals [6,20].

Following this direction, the concept of using Ni-based bimetallic (or multimetallic) catalysts, implying good dispersion of the different components, gains strength for enhancing both hydrogen yields and catalyst stability. A popular route to obtain multimetallic mixed oxides is the synthesis of hydrotalcite-like compounds [21-23]. This family of anionic clays, also known as layered double hydroxides (LDH), is characterized by a layered structure $[M(II)_{1-x}M(III)_x(OH)_2]^{x+} A_{x/n}^{n-} \cdot mH_2O$, containing divalent and trivalent cations and exchangeable anions in the interlayer space. The oxides derived from calcination of the hydrotalcite precursor combine significant properties like high surface area, high metal loading, high thermal stability, controllable acid/base properties, and high metal dispersion [24,25]. Accordingly, the incorporation of active metals into a mixed oxide matrix is a good strategy to stabilize the metal centre. The latter property has been used to design Ni-based hydrotalcite catalysts active in H₂ production via ESR [18,20,26-35] or auto-thermal reforming [36,37] by usual combinations of Ni-Al, Ni-Mg-Al, Ni-Zn-Al, Ni-Co-Zn-Al, Ni-Co-Mg-Al, Ni-Mg-Al-Fe, Ni-Ca-Al, and Ni-Cu-Mg-Al. Moreover, the promoter effect of various metals (La, Ce, etc.) has been also assessed in this type of materials [32]. In most cases, and depending on the chemical composition, these catalysts have demonstrated high activity, high H₂ selectivity and low coke formation, as well as relevant amounts of intermediate products.

Herein, we report for the first time a variety of Ni-Fe mixed oxides derived from reevesite (Ni-Fe hydrotalcite) in the steam reforming of ethanol. Iron is recognized (i) as an active

metal for water-gas-shift, thus increasing the ratio of CO₂ to CO, (ii) to alleviate carbon deposition, (iii) to improve the dispersion of active metals, and (iv) to increase the hydrogen yield [37-39]. The influence of the Ni/Fe molar ratio and the activation of the reevesite precursors on the physico-chemical properties of the catalysts, and on their performance in ESR have been discussed. Detailed characterizations of the catalysts have been performed to attain structure-activity relationships focused in maximizing the production of hydrogen.

2.2. Experimental

2.2.1. Catalyst preparation

Ni-Fe hydrotalcites with nominal Ni/Fe molar ratio of 3:1, 2:1, and 1:1 were prepared by coprecipitation at constant pH. Aqueous solutions of the metal nitrates (1 M of Ni(NO₃)₂·6H₂O and 1 M of Fe(NO₃)₃·9H₂O) and the precipitating agent (NaOH/Na₂CO₃, 1 M of each) were simultaneously fed into a polypropylene vessel by a 905 Titrand® automated titrator (Metrohm AG) equipped with two 800 Dosino® dosing systems. The pH during precipitation in the stirred reactor vessel was maintained at a constant value of 10 (±0.2). After addition of the appropriate ratio of reactants, the slurry was aged at 303 K for 15 h under vigorous stirring. The precipitate thus obtained was filtered and washed thoroughly with deionized water, and dried overnight at 353 K to yield the as-synthesized hydrotalcites (Ni₃Fe-P, Ni₂Fe-P, and NiFe-P). Dried samples were calcined in static air at 773 and 1073 K for 6 h using a ramp rate of 5 K min⁻¹. Along the manuscript, calcined samples are identified by the code C followed by a number, which refers to the calcination temperature in K (e.g., Ni₃Fe-C773), and the code U refer to the used samples recovered after reaction (e.g., Ni₃Fe-U-C773).

2.2.2. Catalyst characterization

The chemical composition of the solids was determined by inductively coupled plasma-optical emission spectroscopy (ICP-OES) in a Spectro Arcos 165 spectrophotometer. Before analysis, the solids were dissolved in 1% HNO₃ aqueous solution.

Powder X-ray diffraction patterns were acquired in a Siemens D5000 diffractometer with Bragg-Brentano geometry using Ni-filtered Cu-K α radiation. Data were collected in the 2 θ range of 5-70° with an angular step of 0.05° and a counting time of 3 s per step. The quantitative phase content and crystallite sizes were determined by a multiphase Rietveld refinement using the Diffrac-Plus Topas software (Bruker AXS GmbH, Germany, version 4.0).

Transmission electron microscopy (TEM) was carried out in a JEOL JEM- 1011 microscope operated at 100 kV. A few droplets of the sample suspended in ethanol were placed on a carbon-coated copper grid followed by evaporation at ambient conditions.

N₂ isotherms at 77 K were measured on a Quantachrome Quadrasorb-SI gas-adsorption analyzer. Prior to the measurements, the as-prepared and calcined samples were degassed in vacuum at 393 K and 573 K for 10 h, respectively.

Thermogravimetric analysis-differential scanning calorimetry (TGA-DSC) was measured in a Mettler Toledo TGA/DSC 1 microbalance. Analyses were performed in air (20 cm³ STP min⁻¹) ramping the temperature from 298 to 1273 K at 5 K min⁻¹.

Temperature-programmed reduction with hydrogen (H₂-TPR) was measured in a ChemBet Pulsar TPR/TPD unit equipped with a thermal conductivity detector. Ca. 50 mg of Ni-Fe oxide obtained by calcination of the hydrotalcite precursors at 773 or 1073 K were loaded in the U-quartz microreactor, pretreated in air (20 cm³ STP min⁻¹) at 573 K for 1 h, and cooled to 323 K in the same atmosphere. The analysis was carried out in a mixture of 5 vol% H₂ in N₂ (20 cm³ STP min⁻¹), ramping the temperature from 323 to 1173 K at 10 K min⁻¹.

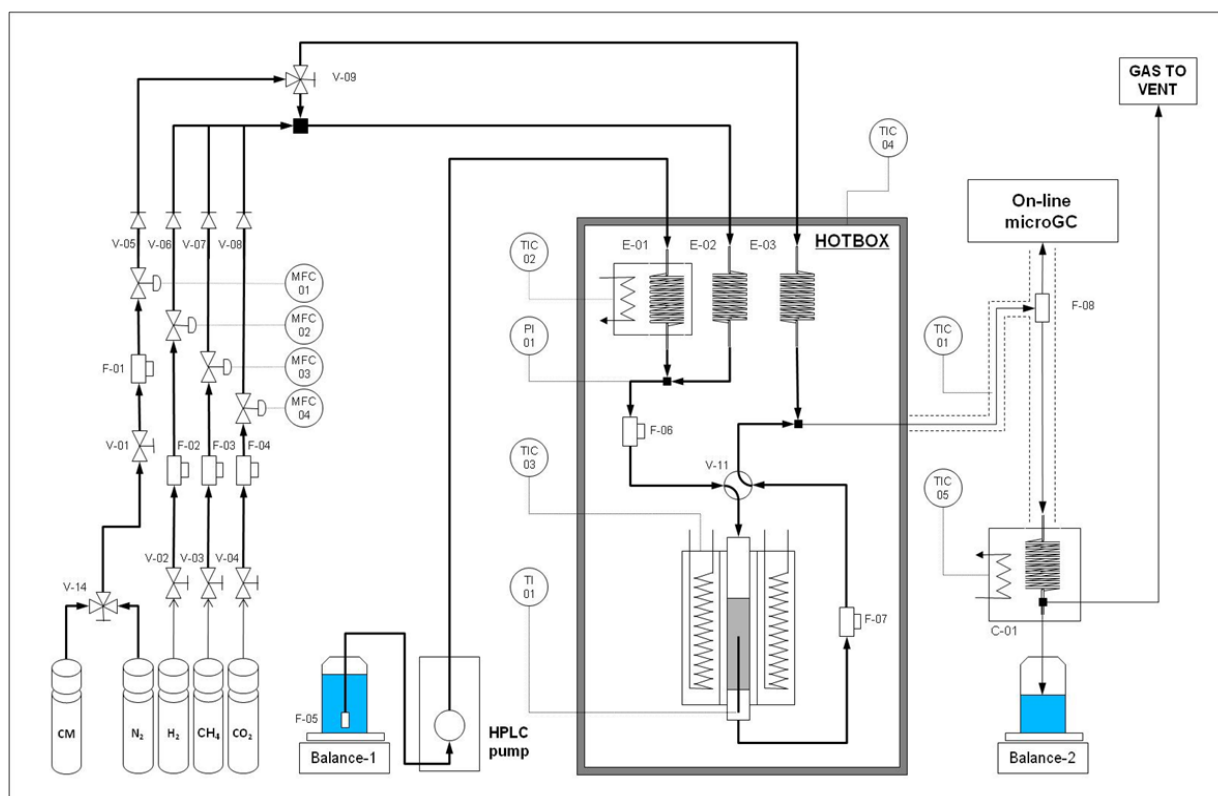
Raman spectra were recorded at ambient temperature using a Renishaw InVia Raman Spectrometer equipped with confocal DM 2500 Leica optical microscope, a CCD detector, and a diode laser operating at 785 nm. The applied power of the laser beam focusing on the sample was 3 mW. The spectra were measured in the 90-2000 cm^{-1} range in single scan with 30 s of exposure time.

2.2.3. Catalyst testing

Steam reforming of ethanol was carried out at ambient pressure in a continuous-flow fixed-bed reactor (10 mm i.d. stainless steel reactor) containing 0.5 g of the catalyst (sieve fraction 100-300 μm) diluted with 10 g of silicon oxide (100-300 μm). In a preliminary blank experiment without catalyst (only SiO_2 as the reactor loading) performed under the same conditions, it was found that the ethanol conversion was kept below 0.03 % for the whole duration of the reaction test. The calcined Ni-Fe catalysts were heated at 773 K under a N_2 flow using a ramp of 10 K min^{-1} , and tested at the same temperature using a typical feed mixture of water/ethanol = 6/1 (steam to carbon molar ratio = 3) and a total flow of 0.2 $\text{cm}^3 \text{STP min}^{-1}$ (weight hourly space velocity, $\text{WHSV} = 147.45 \text{ mol ethanol h}^{-1} \text{ kg}_{\text{cat}}^{-1}$). Occasionally, additional experiments with a higher WHSV of 1474.5 $\text{mol ethanol h}^{-1} \text{ kg}_{\text{cat}}^{-1}$ were performed over one of the catalysts, using 0.05 g of calcined material. Prior to testing, no reduction treatment was applied to any of the reevesite-derived catalysts. The feed mixture of water and ethanol was supplied by a HPLC Gilson 307 piston pump to a liquid evaporator (at 453 K) and the reactant vapors were fed directly to the reactor without diluting with any inert gas (Scheme 1).

The gaseous samples were analyzed on-line by a gas chromatograph (Agilent Technologies 3000A Micro GC) equipped with a TCD detector and two capillary columns, the first one containing an activated molecular sieve 5A using argon as carrier gas (for hydrogen, nitrogen, methane and carbon monoxide analysis), and a second one with a porous polymer PoraPlot Q

using helium as the carrier gas (for carbon dioxide, water, and organics). The sensitivity of the detector to each analyzed compound (response factor) was determined periodically by their calibration against standards of a certified gas mixture composed of H₂, CO, CH₄, CO₂, C₂H₄, and C₂H₂, and liquid reactants, ethanol, water and acetaldehyde, using N₂ as internal standard.



Scheme 1. Schematic representation of the set-up used to perform activity tests.

The ethanol conversion ($X_{C_2H_5OH}$) and product selectivity (S_{H_2} and S_{C_n}) were defined as follows:

$$X_{C_2H_5OH} = \frac{F_{C_2H_5OH,0} - F_{C_2H_5OH}}{F_{C_2H_5OH,0}} \quad (\text{eq. 2.3})$$

$$S_{H_2} = \frac{F_{H_2}}{6(F_{C_2H_5OH,0} - F_{C_2H_5OH})} \quad (\text{eq. 2.4})$$

$$S_{C_n} = \frac{nF_{C_n}}{2(F_{C_2H_5OH,0} - F_{C_2H_5OH})} \quad (\text{eq. 2.5})$$

where $F_{C_2H_5OH}$ denotes the molar flow rate of *ethanol*, and n corresponds to the number of C atoms in each particular product. At the end of the catalytic test, the feed was stopped and the system was cooled down under N_2 . Used catalysts were collected for further characterization.

2.3. Results and discussion

2.3.1. Reevesite activation

2.3.1.1 As-synthesized samples

Figure 2.1 shows the XRD patterns of the coprecipitated materials Ni_3Fe-P , Ni_2Fe-P , $NiFe-P$, and the products of calcination at different temperatures. The as-prepared samples (P) display the characteristic reflections of reevesite [40,41], i.e. the Ni-Fe hydroxycarbonate $Ni_{0.75}Fe_{0.25}(OH)_2(CO_3)_{0.125} \cdot 0.38H_2O$, powder diffraction file 40-0215 from ICDD. As expected from the building of positively charged brucite-like layers and charge-compensating carbonate anions and water molecules in the interlayer space, this material is well-identified as a member of the hydrotalcite-like group of minerals. Although with broader and less intense reflections, even the sample with the lower Ni/Fe ratio is crystalline, indicating that the reevesite structure can be attained in a wide variation of the M^{3+}/M^{2+} ratio [42]. No reflections associated with the single metal hydroxides phases were visible in any of the samples. However, and due to the atypical stoichiometry of the $NiFe-P$ sample, the presence of individual amorphous nickel or iron hydroxide carbonates cannot be discarded. The cell parameters c and a of the rhombohedral structure were calculated from the position of the (003) and (110) diffraction lines, respectively, assuming a 3R stacking of the layers ($c = 3d_{003}$ and $a = 2d_{110}$). The values obtained for the samples are in good agreement with literature (Table 2.1), that is, the c and a values decrease with lower Ni/Fe molar ratios [22,42]. The average crystallite size in the c - and a -directions, as estimated by the Scherrer method using the (003) reflection and the (110) reflection gives indication of the measurement of the crystal

dimension in the stacking direction and that of the crystal dimension in the a-b plane), respectively (Table 2.1). The different aspect ratios between the *a* and *c* values in each sample with different metal contents indicate that the crystalline domains are not equivalent in all crystallographic directions. In fact, the D_{003} increase upon decreasing the Ni/Fe ratio, especially for the sample 1:1, while the D_{110} estimate does not follow a clear trend. As observed in previous studies with other hydrotalcite-like compounds, these differences can be assigned to a lack of positional relationships between consecutive layers within the structure, i.e. turbostratic disorder [43,44].

Table 2.1. Characterization data of the as-synthesized reevesites.

Sample	$M^{2+}/M^{3+a} / -$	<i>c</i> / nm	<i>a</i> / nm	$D_{003}(D_{110})^b$ / nm	V_p / $\text{cm}^3 \text{g}^{-1}$	S_{BET} / $\text{m}^2 \text{g}^{-1}$
Ni ₃ Fe-P	3.03	2.3495	0.3089	4.8 (7.9)	0.06	23
Ni ₂ Fe-P	2.08	2.2977	0.3079	4.8 (20.2)	0.14	90
NiFe-P	1.02	2.2859	0.3076	11 (14.3)	0.27	225

^aMolar metal ratio in solid by ICP-OES. ^bAverage crystallite size estimated by Scherrer analysis applied to the (003) or (110) reflection, respectively.

The morphology of the samples was investigated by transmission electron microscopy (TEM), as shown in Figure 2.2. All samples exhibited randomly distributed aggregates of fibrous particles with an estimated lateral length in the range of 20-45 nm and a thickness of 2-10 nm, depending on the molar ratio in the solid, characteristic of hydrotalcite-type compounds (Figure 2.2) [22,45]. Particles in Ni₃Fe-P tend to aggregate in an edge-face manner, while smaller, thinner and more agglomerated layered particles are present in NiFe-P. The molar Ni/Fe ratio in the solids determined by ICP-OES was 3.03, 2.08, and 1.02 for the three samples, which perfectly match the nominal ratios of 3, 2, and 1 (Table 2.1). Samples were solely mesoporous, with total pore volumes of 0.06, 0.144, and 0.27 $\text{cm}^3 \text{g}^{-1}$, and BET surface areas of 23, 90, and 225 $\text{m}^2 \text{g}^{-1}$, for Ni₃Fe-P, Ni₂Fe-P, and NiFe-P, respectively.

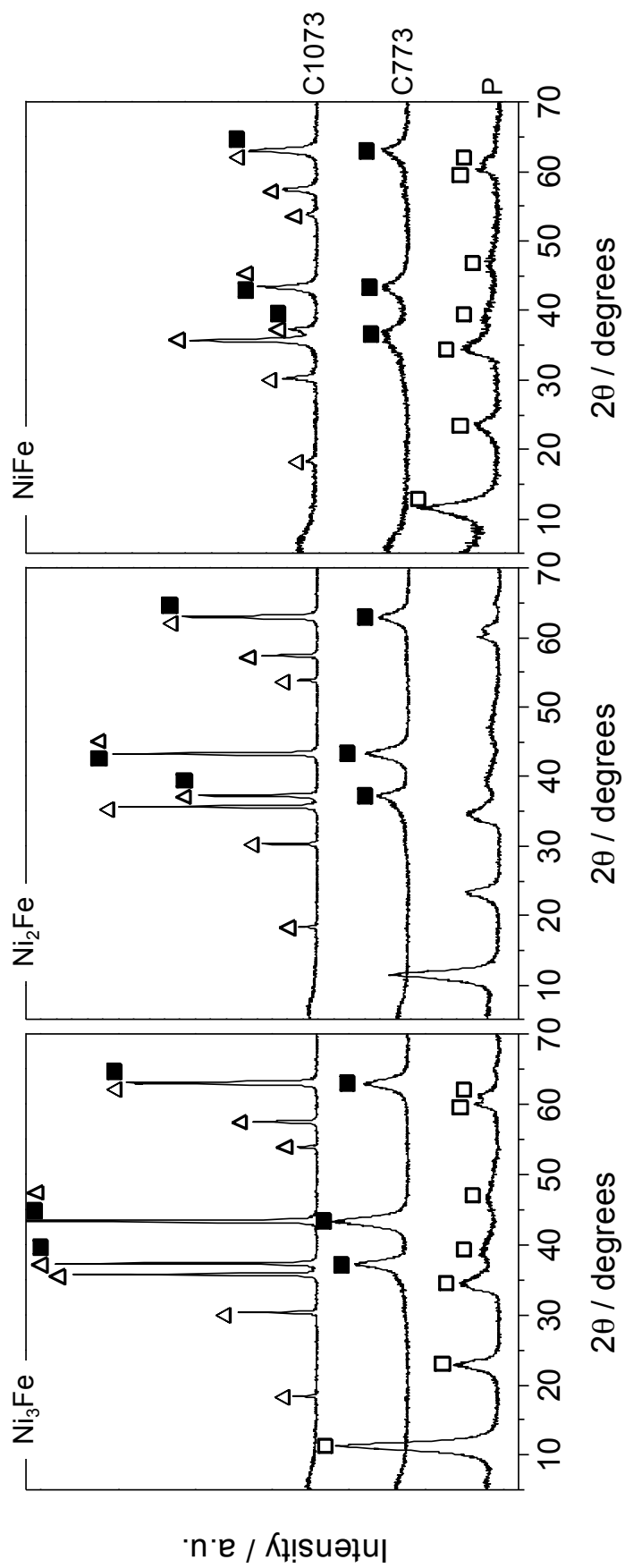


Figure 2.1. XRD patterns of the as-synthesized reevesites (P) and the products of calcination at 773 and 1073 K. Crystalline phases: (□) reevesite, (■) Ni(Fe)O_x, (△) NiFe₂O₄.

2.3.1.2 Thermal decomposition

The visual inspection of XRD patterns of the solids calcined at 773 K showed characteristic reflections of the NiO structure (bunsenite, powder diffraction file 03-065-2901 from ICDD) independently of the Ni/Fe ratio (Figure 2.1). The main diffraction maxima were at ca. 2θ 37°, 43.3°, and 62.9°, according to the (111), (200), and (220) planes, respectively.

Both NiO and NiFe₂O₄ spinel (trevorite, powder diffraction file 54-0964 from ICDD) coexist in the samples calcined at 1073 K, and some of the reflections pair in 2θ position. At this temperature, the diffraction lines related to NiO, which are also coincident with those of NiFe₂O₄, are more intense in the Ni₃Fe-C1073 with respect to the rest of reflections than in the Ni₂Fe-C1073 and NiFe-C1073 samples. In other words, the intensity of the NiFe₂O₄ diffraction lines increases with the increase in Fe content with respect to those of NiO [46]. This is clearly related to the different stoichiometry of the original hydrotalcite precursor ($\text{Ni}_6\text{Fe}_2\text{O}_9 \rightarrow 5\text{NiO} + \text{NiFe}_2\text{O}_4$, $\text{Ni}_4\text{Fe}_2\text{O}_7 \rightarrow 3\text{NiO} + \text{NiFe}_2\text{O}_4$ and $\text{Ni}_2\text{Fe}_2\text{O}_5 \rightarrow \text{NiO} + \text{NiFe}_2\text{O}_4$).

No singular reflections associated with any crystalline form of free iron oxides, i.e. Fe₂O₃ were detected in the samples. However, the reflections of a pure magnetite spinel phase (Fe₃O₄, powder diffraction file 01-076-0956 from ICDD) exhibit the same diffraction pattern than that of NiFe₂O₄ spinel; therefore, although the content of Ni in the catalysts precursors is higher (Ni/Fe 3:1 and 2:1) or equal (Ni/Fe 1:1) than that of Fe, and calcination leads to the formation of NiO + NiFe₂O₄ at the corresponding stoichiometry, partial decomposition into pure magnetite cannot be totally discarded [47].

Typically, calcination of the hydrotalcite structure leads to the formation of a solid solution, denoted as Ni(Fe)O_x, and their corresponding NiO reflections are slightly shifted to higher 2θ values than those corresponding to pure NiO, due to Fe³⁺ replacement in the nickel oxide lattice [48,49]. In all cases, the cubic cell of the solid solution ($a = 0.4183 - 0.4173$ nm) in the Ni₃Fe-C773, Ni₂Fe-C773 and NiFe-C773 is significantly smaller than that of NiO (0.4194 nm).

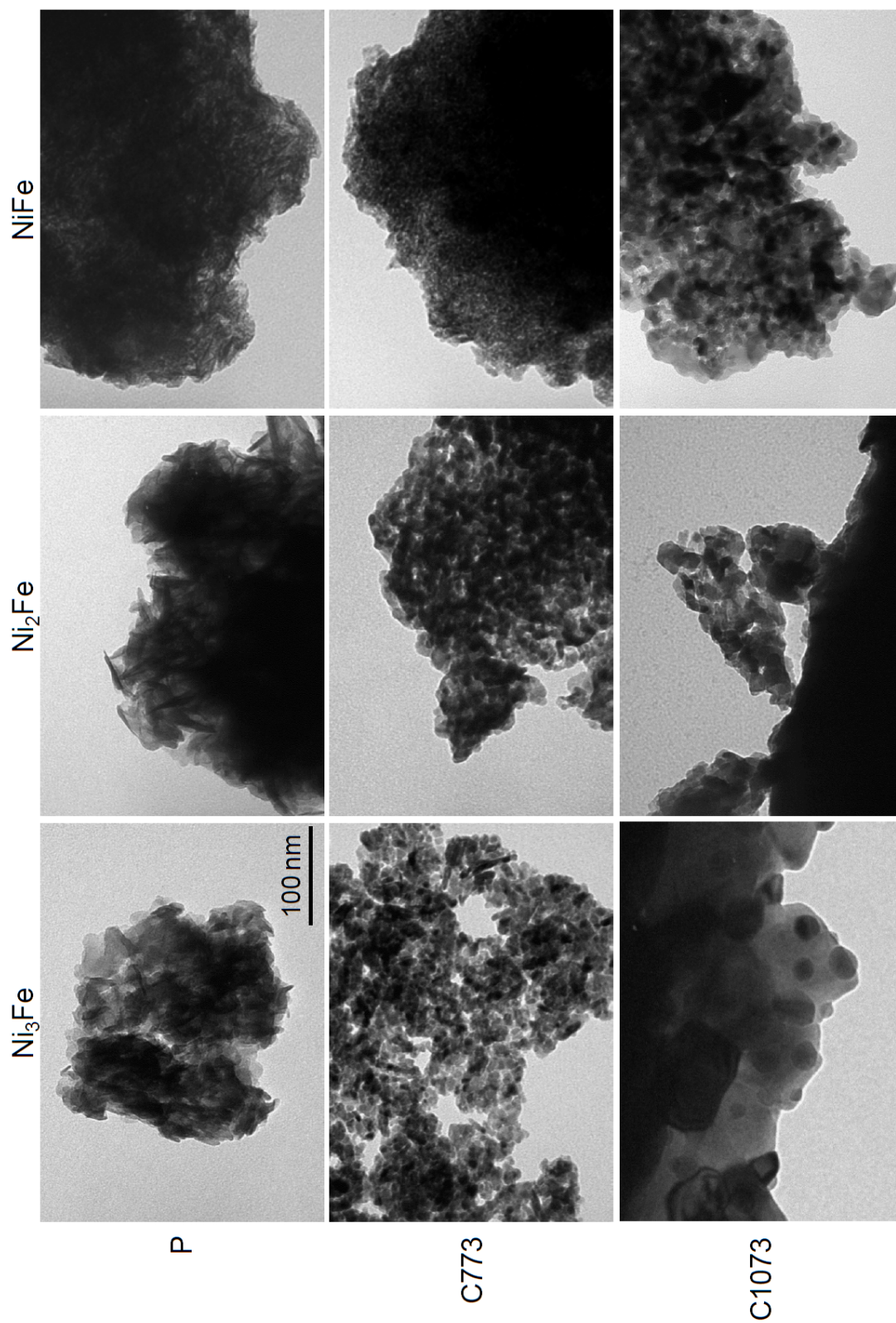


Figure 2.2 Transmission electron micrographs of the different samples. The same scale bar applies to all the micrographs.

As reported by Puxley et al. [50], the disordered metastable mixed oxide Ni(Fe)O_x phase starts to transform into additional phases, especially NiFe₂O₄ at high calcination temperatures. An indication of the segregation of the M³⁺ cation from the solid solution forming pure NiO + spinel can be derived from comparison of the cell parameter *a* in all samples with respect to that of pure NiO. In this case, the cell parameter of the NiO phase in the samples calcined at this temperature (Ni₃Fe-C1073, Ni₂Fe-C1073, and NiFe-C1073) is in the range 0.4181-0.4172 nm, as calculated from the (400) reflection at 2θ = 43° (Table 2.2), being relatively smaller than that of pure nickel oxide. This suggests that iron is partially segregated from the solid solution leading to NiFe₂O₄ spinel, and part of the solid still remains as Ni(Fe)O_x. These results slightly differ from previous results on hydrotalcite-derived Ni-Al oxides calcined at 773 and 1173 K, in which total segregation of Al was observed [51].

Table 2.2: Characterization data of the calcined reevesites.

Sample code	a ^a / nm	Phase composition ^b / %		Crystallite size ^c / nm		V _p / cm ³ g ⁻¹	S _{BET} / m ² g ⁻¹
		Ni(Fe)O _x	NiFe ₂ O ₄	Ni(Fe)O _x	NiFe ₂ O ₄		
Ni ₃ Fe-C773	0.4183	76.7	23.3	5.7	2.2	0.20	73
Ni ₂ Fe-C773	0.4175	60.4	39.6	5.3	2.4	0.22	68
NiFe-C773	0.4173	37	63	3.5	2.0	0.33	183
Ni ₃ Fe-C1073	0.4181	54.8	45.2	89.5	79.7	0	1.1
Ni ₂ Fe-C1073	0.4179	39.5	60.5	61.3	71.8	0	0.8
NiFe-C1073	0.4176	11	89	11.0	14	0.14	44

^aEstimated cubic cell parameter from the (200) and (400) reflections at ca. 2θ = 43°, for the samples calcined at 773 and 1073 K, respectively. ^bCrystalline phase composition determined by Rietveld refinement. ^cAverage crystallite size obtained by refinement of the whole profile. The weighted residual error was in the range 3-6% for both crystallite size and phase composition.

In order to gain a more quantitative analysis of the phases present in the calcined samples, a Rietveld refinement method was applied. Based on the crystalline phases (Table 2.2) and contrarily to what is observed by simple visual inspection of XRD patterns, the trevorite

phase (NiFe_2O_4) was found over all calcined samples. In fact, the amount of NiFe_2O_4 increases upon decrease of the Ni/Fe molar ratio, independently of the calcination temperature, and the opposite applies to the $\text{Ni}(\text{Fe})\text{O}_x$ phase. As expected, the NiFe_2O_4 content is higher in samples calcined at 1073 K, due to the greater tendency of $\text{Ni}(\text{Fe})\text{O}_x$ to be transformed into trevorite at such high temperatures. This reinforces the idea that the surplus of Fe^{3+} in non-theoretical reevesites, i.e. the one with Ni/Fe=1, is not completely replacing Ni^{2+} in the nickel oxide lattice, and therefore, a higher propensity of the mixed oxide to segregate into the NiFe_2O_4 phase is observed.

Table 2.2 also shows the crystallite size obtained from the Rietveld refinement method of the calcined samples. The $\text{Ni}(\text{Fe})\text{O}_x$ average crystallite size for the samples calcined at 773 K, present no substantial differences (in the range 3.4-5.7 nm). In contrast, calcination at 1073 K leads to larger NiO crystallites (11 nm for NiFe-C1073, 61 nm for Ni_2Fe -C1073, and 89 nm for Ni_3Fe -C1073). Similarly, the NiFe_2O_4 crystallite size is around 2 nm after calcination at 773 K, while these values are larger upon calcination at 1073 K, and decrease upon decreasing the Ni/Fe ratio.

Samples calcined at 773 K show the presence of uniform and small nanoparticles characteristic of the oxide of ca. 2-12 nm (Figure 2.2). It is interesting to mention that the NiFe-C773 sample exhibits the smallest $\text{Ni}(\text{Fe})\text{O}_x$ and NiFe_2O_4 crystallites (Table 2.2). Due to sintering of NiO and crystallization/growing of NiFe_2O_4 , the samples calcined at 1073 K generally present larger particles, with sizes in the range of 10-45 nm, which are in line with XRD observations.

As concluded from other works in the literature [48,51-53], the increase in the calcination temperature to 1073 K gives rise to structural rearrangements of the cubic mixed oxides discussed above with segregation of the trivalent cation from the $\text{M}^{2+}(\text{M}^{3+})\text{O}_x$ solid solution and corresponding formation of spinel-type phases. This ultimately causes an important decrease in surface area in all samples (Table 2.2), particularly at 1073 K, due to

crystallization/growing of the NiFe_2O_4 spinel phase. It is noteworthy that the formation of the spinel phase is even observed at lower calcination temperatures, which is probably induced by a promotion effect by iron.

These results are substantiated by thermogravimetric analysis (Figure 2.3, top), which shows the typical two-step decomposition pattern of anionic clays, with transition temperatures at ca. 440 K (removal of interlayer water) and ca. 550 K (dehydroxylation and decarbonation) for the $\text{Ni}_3\text{Fe-P}$ and $\text{Ni}_2\text{Fe-P}$ samples [42,54]. In general, the heat flow profiles show the presence of two endothermic transitions (Figure 2.3, bottom), matching in temperature with TGA results. The decomposition profile of the NiFe-P sample slightly differs from the other two samples, especially in the low-temperature region, where various small transitions can be observed. This is also clearly detected by DSC thermograms, in which small endothermic steps occur in the range 350-700 K (with maxima at 352, 498, 640 and 682 K) in parallel with the two major transitions. This could be associated to the presence of additional amorphous nickel-iron hydroxide carbonate phases decomposing in the same temperature range. The total weight losses amount 31 and 33% for the $\text{Ni}_3\text{Fe-P}$ and $\text{Ni}_2\text{Fe-P}$, respectively, similar to the theoretical weight losses of the pure reevesite samples as calculated based upon their chemical formulae (30% and 32.8% for Ni_3Fe and Ni_2Fe pure reevesites, respectively) [55]. The lower total weight loss for the NiFe-P (29%) with respect to the theoretical value (37.8%) might indicate the incomplete precipitation of the hydrotalcite phase, due to the formation of other amorphous phases beside the reevesite precursor.

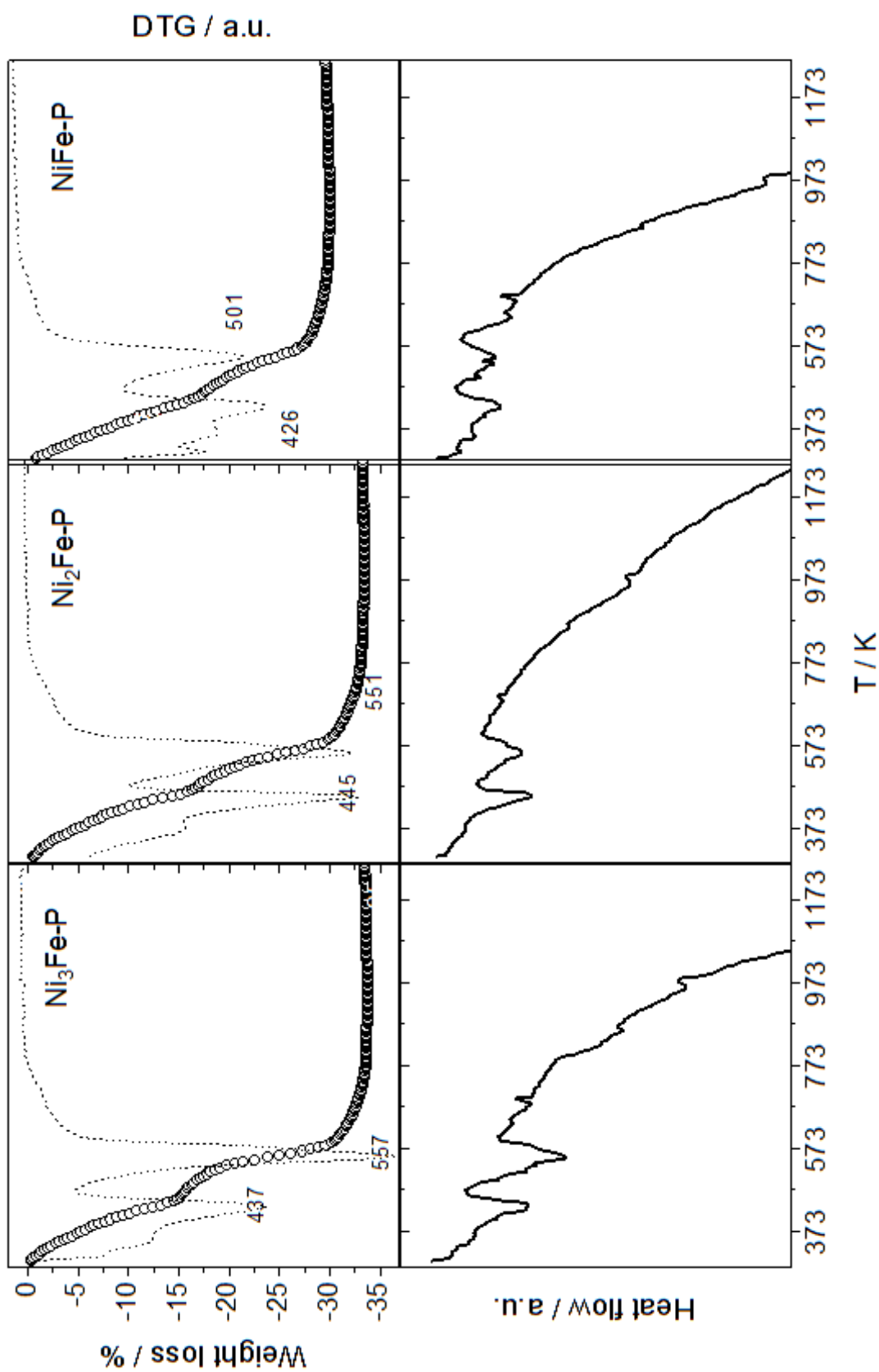


Figure 2.3. Thermogravimetric and calorimetric profiles of the as-synthesized reevesite samples in air and derivative of the weight loss.

The formation of the NiFe_2O_4 spinel phase in the samples calcined at 1073 K was also confirmed by Raman spectroscopy. The spectra of the different samples are shown in Figure 2.4. The Raman peaks at 213, 333, 482, 572, 589, 662 (shoulder), and 701 cm^{-1} are assigned to the NiFe_2O_4 spinel phase [56]. The strong band in the range $670\text{--}710\text{ cm}^{-1}$ is a typical feature of the Raman spectra of inverse spinels [57]. The peaks at 1140 and 1340 cm^{-1} match with those of $\gamma\text{-Fe}_2\text{O}_3$; however, a previous study has found that the formation of this compound should lead to bands of similar intensity than the band at 701 cm^{-1} , thus indicating that $\gamma\text{-Fe}_2\text{O}_3$ is absent in this sample [58]. These bands are then attributed to overtones of the NiFe_2O_4 phase. Samples calcined at 773 K display broad bands at 362, 498 (shoulder), 561, and 696 cm^{-1} , which may be attributed to the NiO structure [56,59]. Bands in the NiFe samples are far less intense than those in Ni_2Fe and Ni_3Fe , whatever the calcination temperature. This should be related with the increase of the NiO crystallite size in the latter samples.

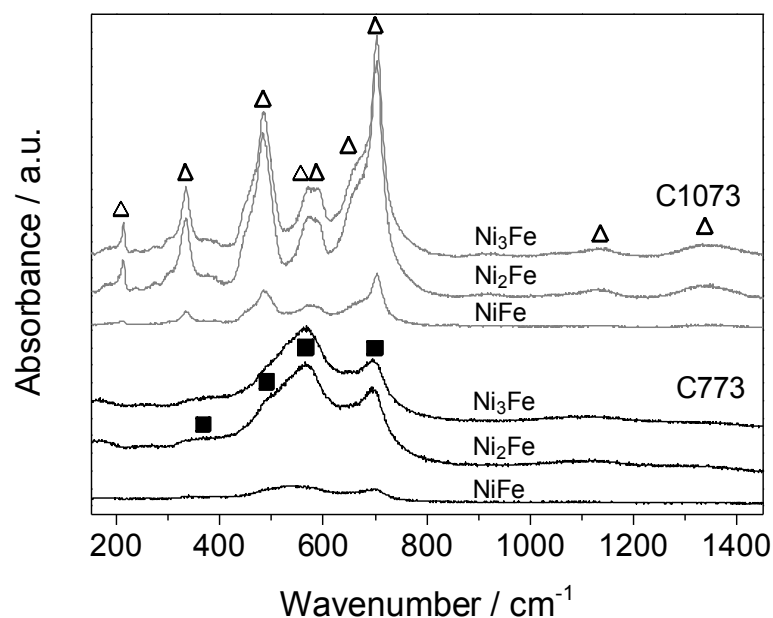


Figure 2.4. Raman spectra of the Ni-Fe oxides obtained upon calcination at 773 (black lines) and 1073 K (grey lines). Phases: (■) Ni(Fe)O_x , (Δ) NiFe_2O_4 .

Interestingly, samples calcined at the lowest temperature do not display the bands related to spinel, as could be expected based on the percentage of phases determined by XRD, due to the small crystallite size of NiFe_2O_4 (ca. 2 nm). As for the samples calcined at 1073 K, the bands related to NiO are partially masked by the bands of spinel.

2.3.1.3 Reduction behavior

Temperature programmed reduction profiles obtained for the Ni/Fe samples calcined at the two selected temperatures are shown in Figure 2.5. The results indicate that the reduction occurs in a wide temperature range of ca. 573-1150 K depending on the calcination temperature of the reevesite precursor. The TPR maximum shifts to higher temperatures upon increasing the calcination temperature. The peaks of hydrogen consumption also display different profiles depending on the Ni/Fe molar ratio. The whole signal for the sample with lower Ni/Fe ratio is shifted to higher temperatures, indicating that the NiFe samples are less reducible and more stable than the others.

The $\text{Ni}_3\text{Fe-C773}$ sample shows a peak of hydrogen consumption centered at 806 K, with a big shoulder at 735 K. The $\text{Ni}_2\text{Fe-C773}$ sample exhibits a peak centered at 792 K with a small shoulder at 640 K and a second shoulder at 868 K. The NiFe-C773 sample displays a more complex reduction pattern, with two peaks centered at 873 and 1004 K, and a small shoulder at 700 K. The reduction of pure NiO typically shows a single peak located at 613-670 K, which matches the low-temperature shoulder in $\text{Ni}_2\text{Fe-C773}$ [31,60]. According to these results, the reduction of nickel in the Ni(Fe)O_x solid solution seems to be hindered by the presence of iron, a similar effect occurring in other $\text{Ni(M}^{3+}\text{)-oxides}$ [51,61], thus causing a shift to higher reduction temperatures with respect to pure NiO. As observed by Tu et al.[46], the reduction temperature for each peak slightly decreases with the increase in the Ni/Fe molar ratio from 1 to 3. In fact, the reduction of Fe_2O_3 and NiO typically proceeds over almost the same temperature range, that is, 573-973 K. It should be taken into account that the

broad temperature range may include the co-reduction of various nickel and iron species, and that a definite assignment of the individual reduction peaks of Fe and Ni in the catalysts is not straightforward. That is the case for the Ni₃Fe-C773 sample, which displays a more symmetrical TPR profile, and the assignment of Ni and Fe reduction cannot be directly ascertained taking into account the vigorous reduction of NiO in the wide range of 523-823 K [37]. In fact, the reduction of iron oxides may occur in various steps, in the order Fe₂O₃→Fe₃O₄→FeO→Fe⁰, taking place in the temperature range 573-1000 K [62,63]. Zu et al. [64] observed that the reduction of Fe³⁺ to Fe²⁺ displays a sharp peak at ca. 702 K, while a continuous broad peak corresponds to reduction of Fe²⁺ to Fe⁰, which is even not complete at 1273 K. The visual inspection of our samples calcined at 773 K shows that peaks at 735, 792 or 873 K in Ni₃Fe-C773, Ni₂Fe-C773 and NiFe-C773, respectively, might be attributed to Fe³⁺ reduction into Fe₃O₄, intermingled with reduction of Ni(Fe)O_x species.

The high-temperature peak at 868 K in Ni₂Fe-C773 and 1004 K in NiFe-C773 grows and shifts to higher temperature with the increase in iron content. Based on the percentage of crystalline phases determined by XRD (Table 2.2), this variation might be attributed to iron-containing species including NiFe₂O₄ (and/or Fe₃O₄) and FeO [37], present in the samples calcined at 773 K and also formed upon heating and reduction of Ni(Fe)O_x species during TPR analysis.

In the C1073 samples, the peaks are broadened towards higher temperatures, indicating the presence of a higher amount of NiFe₂O₄ with larger crystallite sizes observed by XRD. For example, the peak centered at 792 K in Ni₂Fe-C773 and its shoulder at 868 K is unfolded in two well-discerned peaks at 795 and 909 K in the Ni₂Fe-C1073. In this case, and considering that iron is only partially segregated from the solid solution to form the spinel phase, the high-temperature peak should account for the reduction of the Ni-Fe spinel. This phase has been found to be reduced at higher temperatures [37]. In the Ni₃Fe-C1073 sample, a broad reducibility peak is observed due to the presence of nickel species in different environments

in terms of interaction with iron, as concluded from the presence of $\text{Ni}(\text{Fe})\text{O}_x$ and NiFe_2O_4 (or Fe_3O_4) phases by XRD (Figure 2.1 and Table 2.2). A similar conclusion can be extracted for the NiFe-C1073 sample, which may even incorporate other oxides derived from amorphous phases in the reevesite precursor.

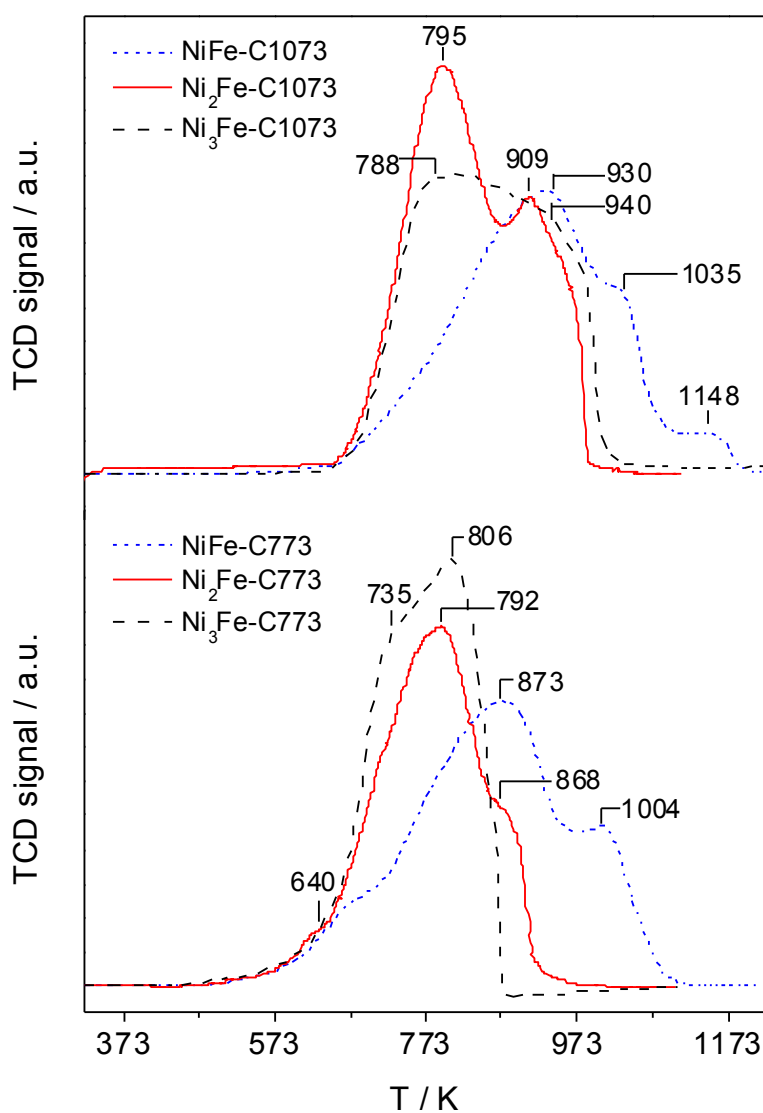


Figure 2.5. H₂-TPR profiles of the Ni-Fe catalysts calcined at different conditions.

Besides, the H₂ consumption by the spinel, whatever the Ni/Fe molar ratio, does not seem to fulfill the theoretical molar ratio $\text{NiO}/\text{NiFe}_2\text{O}_4$ (5 for Ni₃Fe, 3 for Ni₂Fe precursor, and 1 for NiFe). This would also confirm that total segregation of iron from the solid solution does not

occur, and a wide range of oxidic structures (NiO , Ni(Fe)O_x and NiFe_2O_4 or Fe_3O_4) coexist in the sample, thus covering the broad reduction range of 673-1150 K.

It is important to note that no reduction pretreatment was performed over the calcined catalysts before reaction. Accordingly, it can be anticipated that nickel species in these samples are expected to be gradually reduced under reaction conditions, as confirmed by the XRD pattern of the used samples in Figure 2.6. It can be observed that treatment of the catalysts calcined at 773 K with the H_2 produced during ESR results in the disappearance of the peaks corresponding to Ni(Fe)O_x phase, whatever the Ni/Fe ratio. In parallel, two narrow reflections belonging to Ni^0 (powder diffraction file 4-850 from ICDD) emerge at 2θ 44° and 52°. Besides, additional diffraction lines at 2θ 30°, 35.5°, 37.5°, 43°, 57°, and 62° appear which correspond to the growing of NiFe_2O_4 (and/or Fe_3O_4) under reaction conditions (773 K). As expected from the metal ratio in the samples and the stoichiometry of the reevesite precursors upon calcination, the intensity of the NiFe_2O_4 (or Fe_3O_4) diffraction lines increases with the increase in Fe content. The XRD patterns of samples calcined at 1073 K after reaction show the same trends (Figure 2.6). NiFe_2O_4 reflections present in the calcined samples are still present though exhibiting a lower intensity, which may indicate that Ni^{2+} in the spinel phase is only partially reduced. The percentage of all crystalline phases and the average size of the nickel crystallites in these reduced samples were estimated by the Rietveld refinement method (Table 2.3). After reaction, the amount of Ni(Fe)O_x decreases upon reducing the Ni/Fe ratio and at increasing calcination temperatures, at the expenses of Ni^0 formation. The increase in the percentage of spinel whatever the calcination temperature suggests that practically all Ni(Fe)O_x is reduced and NiFe_2O_4 also experiences a partial reduction.

The amount of NiFe_2O_4 is also higher in samples calcined at 1073 K, but the amount of metallic nickel is smaller in samples with lower Ni/Fe ratio, due to the less reducible character of samples with higher iron content (Figure 2.5).

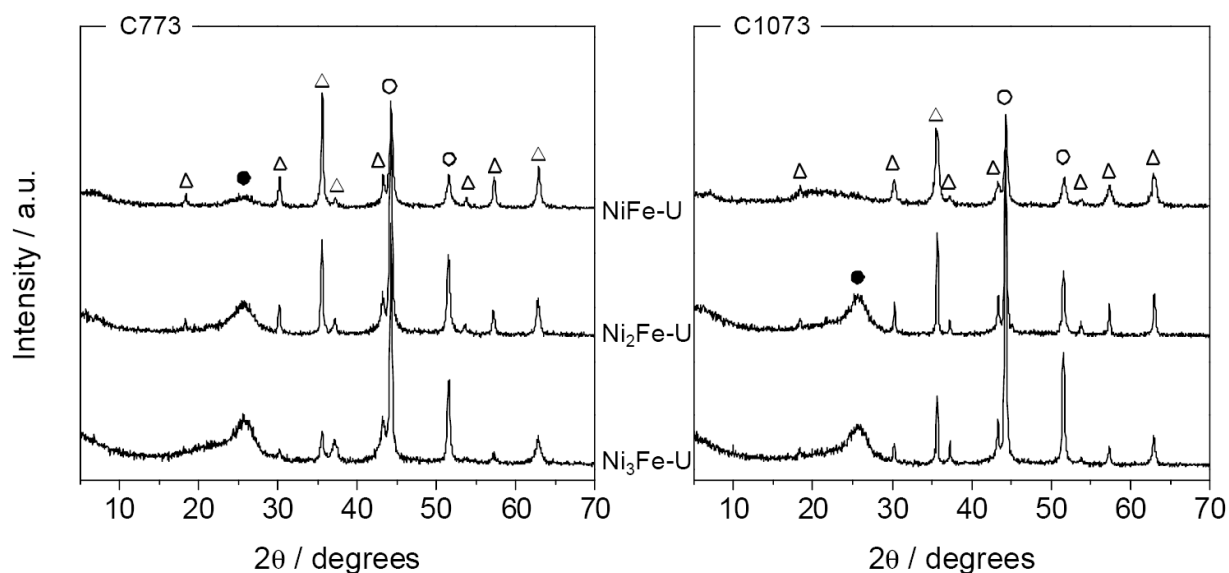


Figure 2.6. XRD patterns of the used Ni-Fe oxides. Crystalline phases: (○) Ni, (Δ) NiFe₂O₄ (or Fe₃O₄), (●) graphite.

Table 2.3: Characterization data of the used catalysts and average carbon balance during the reforming experiments.

Sample code	Phase composition ^a / %			Crystallite size ^b / nm			Carbon balance ^c / %
	Ni(Fe)O _x	NiFe ₂ O ₄	Ni ⁰	Ni(Fe)O _x	NiFe ₂ O ₄	Ni ⁰	
Ni ₃ Fe-U-C773	27.3	16.0	56.7	7.3	21.0	26.6	95.4
Ni ₂ Fe-U-C773	6.4	34.8	58.8	6.8	31.6	20.4	94.2
NiFe-U-C773	0	57.7	42.3	-	23.1	13.9	98.4
Ni ₃ Fe-U-C1073	7.7	23.6	68.7	9.8	47.8	33.3	93.6
Ni ₂ Fe-U-C1073	0	44.7	55.3	-	52.1	25.4	96.3
NiFe-U-C1073	0	67.7	32.3	-	12.4	16.0	97.0

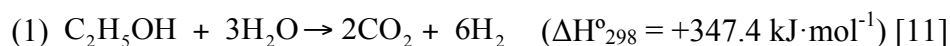
^aCrystalline phase composition determined by Rietveld refinement. ^bAverage crystallite size obtained by refinement of the whole profile. ^cDetermined in the first 8 h of reaction.

As expected, Ni⁰ crystallites in samples calcined at 773 K and used in the reaction are smaller than in used samples calcined at 1073 K, due to the fact that the size of the metal is somehow inherited from the size of the nickel oxide precursor. Besides, the Ni⁰ crystallite size decreases when the Ni/Fe ratio decreases (from 26.6 in Ni₃Fe-U-C773 to 13.9 nm in NiFe-U-C773, and from 33.3 in Ni₃Fe-U-C1073 to 16 nm in NiFe-U-C1073), which indicates a slightly lower

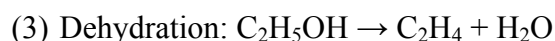
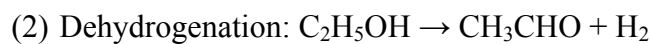
sintering of the metal in the NiFe-U-C773 catalyst upon reaction. The broad diffraction peak at $2\theta 26^\circ$ represent the formation of deposited carbon upon reaction (JCPDS: 41-1487) [20]. Interestingly, the intensity of this diffraction peak is lower in the NiFe-U-C773 sample than in the other two samples, thus indicating a lower tendency for coke formation as the amount of iron increases.

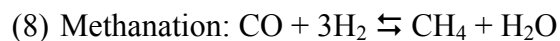
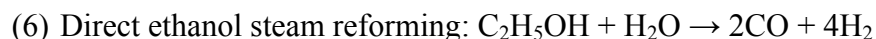
2.3.2. Steam reforming performance

Ideally, the ethanol steam reforming process is able to convert one mole of ethanol into six moles of hydrogen.



However, the whole overall process is a complex set of elementary steps involving several organic intermediates and various reaction pathways, depending on the catalyst and operating conditions [9,65]. Ethanol decomposes mainly through two different routes. The first route dehydrogenates ethanol towards acetaldehyde, which can be further decomposed to CH_4 and CO . This decomposition leads to CO_2 and H_2 through steam reforming and water-gas-shift. The second route dehydrates ethanol into ethylene, which is strongly adsorbed on the catalyst active sites. This easily induces coke deposition via polymerization. All these intermediates can suffer different transformations, which amplify the number of products following the set of reactions listed below:





Accordingly, high catalyst stability with low content on carbon deposits and high hydrogen production are facilitated when the dehydrogenation route takes place.

To compare the activity of the catalysts, experiments using a $\text{H}_2\text{O}/\text{ethanol} = 6$ (steam to carbon molar ratio = 3) have been performed during a period time of 24 h at 773 K. Liquid products other than acetaldehyde, such as acetone, were not detected. In our results, the products observed were H_2 , CO , CO_2 , CH_4 , CH_3CHO , and C_2H_4 , suggesting that most of the reactions listed above occur to a certain extent. C_2H_2 and C_2H_6 were only detected in trace amount (maximum 1% selectivity).

2.3.2.1 Effect of Ni/Fe molar ratio

The conversion of ethanol and the distribution of products in terms of selectivity with time on stream over the reevesite-derived catalysts calcined at 773 K are presented in Figure 2.7. The ethanol conversion remains 100% for the first 3 hours of reaction in all cases. A first inspection of the H_2 selectivity initially denotes a clear difference, that is, H_2 selectivity decreases from ca. 80 to 40% in the first 3 hours over $\text{Ni}_3\text{Fe-C773}$. A similar trend occurs with CO_2 , and no acetaldehyde is produced. As previously mentioned, it is generally accepted that the initial steps in ESR can be reactions (2) and (3). Considering the low WHSV used in this work, reactions (2i) and (2ii) take place, thus explaining the absence of acetaldehyde in the initial product mixture. Meanwhile, the amounts of CO and CH_4 increase, indicating that

reactions (2i) and (2ii) compete, and particularly, reaction (2ii) likely becomes the predominant reaction due to the higher amount of CO at the initial stages, when the content of Ni/Fe is higher. Besides, the involvement of cracking (reaction 4) cannot be totally discarded, although higher amounts of methane would be expected if this reaction was predominant.

The decrease in H₂ and CO₂ may also indicate that both methanation (reaction 8) and reverse water gas shift (reverse of reaction 7) take place to a certain extent, thus increasing the amount of CH₄ and CO at the initial stages of the reaction. Eventually, CO methanation and reverse WGS can lead to CO₂ methanation. This behavior is consistent with the highest amount of Ni in this catalyst, which induces a higher activity towards methanation [17], as compared to the others materials.

In this first period, it is therefore likely that metallic nickel and coke deposits start to form in the beginning of the reaction, and that the formation of these species is faster over the catalysts with high nickel content (those with higher Ni/Fe ratio), leading to high activity in ethanol dehydrogenation, reverse water gas shift and CO hydrogenation (methanation).

After 2 hours of reaction, the selectivity of CH₄, CO, CO₂, and H₂ over the Ni₃Fe-C773 catalyst decrease in parallel to the increase in acetaldehyde, which reaches 45% at ca. 3 hours of reaction. The reason for this decrease can be attributed to the increase in the amount of carbonaceous deposits and Ni⁰ particle size with time on stream, which may lead to reduction in ethanol dehydrogenation, reverse water gas shift, and methanation activity. Besides, reaction (2i) can be also hindered at longer time on stream, thus explaining the growth in acetaldehyde and the decrease in CH₄ and CO.

After this time, the ethanol conversion declines abruptly to 38% at 20 hours of reaction, and remains stable near the end of the reaction. Simultaneously to this activity decay, the selectivity to H₂ and CO₂ progressively increase to 56 and 45%, respectively, at the expenses of CO, and the level of acetaldehyde slightly decreases to 35%.

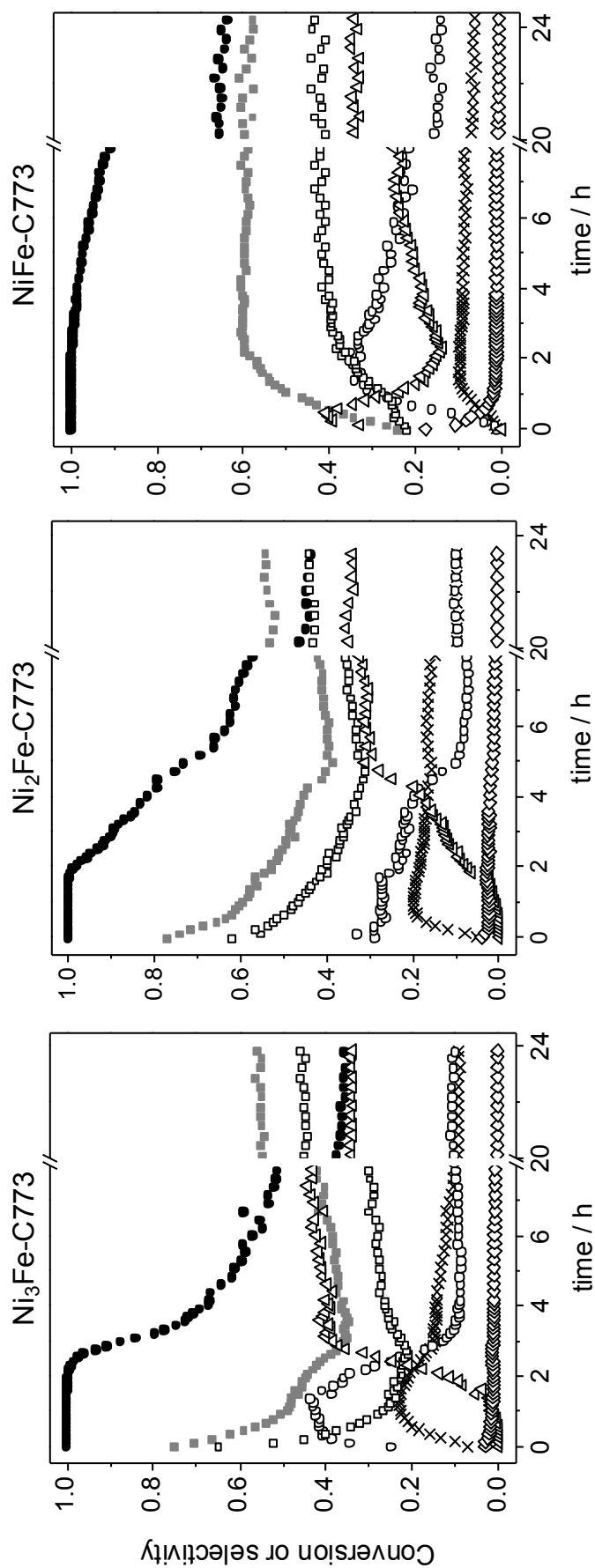


Figure 2.7 Ethanol conversion (●) and selectivity to the different products (■ H₂, × CH₄, ○ CO, □ CO₂, △ CH₃CHO, ◇ C₂H₄) vs time during ethanol steam reforming over the Ni-Fe catalysts calcined at 773 K. Reaction conditions: H₂O/C₂H₅OH ratio = 6, T = 773 K, WHSV = 147.45 mol ethanol h⁻¹ kg_{cat}⁻¹, and P = 1 bar.

The latter observations suggest that direct reforming reactions like the WGS (7) and reaction (2ii) become dominant with increasing time on stream, which finally contribute to higher hydrogen and carbon dioxide selectivity at the end of the reaction.

The behavior of the Ni₂Fe-C773 catalyst follows a very similar progression of the reaction, although changes in products selectivity occur somewhat later than in the previous catalyst (Ni₃Fe-C773). It is important to notice that the selectivity to ethylene was very low over both catalysts, barely reaching a maximum of 3%.

Concerning the NiFe-C773 catalyst, important differences can be derived. In the initial time range of 3 hours, an opposite trend with respect to the other catalysts is clearly manifested. The acetaldehyde selectivity reaches 50% instantaneously, followed by a brusque drop till 15%. In parallel, the H₂ and CO selectivity increase from 37 to 61% and from 0 to 34%, respectively. CH₄ also experiences an increase to 10%, and ca. 17% of ethylene formed in the beginning of the reaction decreases to less than 3%. This contrasts with previous catalysts showing a constant increase in acetaldehyde after 2 hours of reaction. It seems that reaction (2i) is activated within the first 2 hours over this catalyst, leading to decreased acetaldehyde and increased methane selectivity. These observations suggest that the decomposition reaction (2i) is attributed to the presence of metallic nickel particles, which are formed slowly over the NiFe-C773 catalyst. This would indicate that the NiFe-C773 catalyst exhibits the longest induction period. Besides, the slow formation of metallic nickel particles would be accompanied by certain hindering of CO methanation (reaction 8), even in the beginning of the reaction as concluded from the gradual increase in H₂ and CO, which are not consumed by the reaction.

Also, a certain degree of ethanol dehydration to ethylene occurs when the reactant contacts the catalyst. The high C₂H₄ selectivity in the beginning of the reaction would imply the presence of abundant and active Lewis acid sites (Ni²⁺ and Fe³⁺), which would be responsible for dehydration (reaction 3). This behavior would be also in agreement with the slow

formation of Ni^0 particles, and evidences that Ni^{2+} species are the active species in the beginning of the reaction, which are transformed into Ni^0 upon time-on-stream, the latter becoming active species for acetaldehyde reforming.

The high WGS (7) and acetaldehyde steam reforming (2ii) activity over this catalyst would be a consequence of the promotion effect of Fe/Fe^{2+} species on the metallic Ni^0 particles with time on stream. After this time, the H_2 , CO_2 and CH_4 selectivity remain stable till the end of the reaction. In contrast, the CO selectivity decreases concomitantly to the increase in acetaldehyde, while the ethanol conversion experiences a progressive drop. This implies a lower activity towards acetaldehyde decarbonylation (2i) with time on stream, motivated by the slow formation of coke deposits.

In summary, catalysts calcined at 773 K show good stability only in the first 3 h on stream. However, the initial activity declines with increasing the Ni content. The NiFe-C773 catalyst shows the best catalytic performance in the reaction period of 24 h. This can be in part due to the less reducible character of this sample as observed by TPR experiments (Figure 2.5), and the fact that small metallic nickel particles slowly formed during the reaction can remain in the suitable dispersed state, resulting in long-term stability for the reforming reaction.

The selectivity to acetaldehyde increases in all cases but at different time on stream, suggesting that at certain times of the reaction, the catalysts point to a decreased activity for acetaldehyde conversion, concomitantly to variations in H_2 , CO , CO_2 and CH_4 . As concluded from XRD observations in Figure 2.6, a sufficient amount of active Ni^0 sites is guaranteed in all catalysts due to the gradual *in situ* NiO reduction at the initial stage of the reaction. The percentage of phases $\text{Ni}(\text{Fe})\text{O}_x + \text{NiFe}_2\text{O}_4$ in the C773 catalysts before reaction is mainly guided towards a mixture containing an increasing amount of NiFe_2O_4 upon decreasing the Ni/Fe ratio. Most of the $\text{Ni}(\text{Fe})\text{O}_x$ is therefore reduced into Ni^0 by the H_2 produced by ethanol dehydrogenation and acetaldehyde reforming, as concluded from the different compounds observed in the beginning of the reaction with the different catalysts. Changes in acetaldehyde

selectivity suggest the different velocity for *in situ* catalyst conditioning or activation leading to Ni⁰, in parallel to the growing of NiFe₂O₄ crystals. As mentioned in section 3.1.3, the intensity of the NiFe₂O₄ diffraction lines increases with the decrease in Ni/Fe content. Overall, the NiFe-C773 catalyst performs better due to its high activity and increasing hydrogen selectivity during the 24 h of reaction. The cause of this improved performance can be attributed to the fact that lower Ni/Fe ratios induce the slow formation of metallic nickel particles and coke deposits, and strongly promote ethanol dehydrogenation and acetaldehyde reforming. That is the case of the NiFe-C773 catalyst, which presents the highest iron content. This result is consistent with a previous study on nickel-based catalysts doped with iron (10%) in auto-thermal reforming of ethanol, in which iron plays a key role for enhancing the catalytic activity and hydrogen selectivity via promotion of ethanol dehydrogenation [39]. However, our material has a limited activity to transform acetaldehyde to C1 products after longer time on stream, which adversely affects H₂ yields and catalyst stability. This is likely due to partial deactivation of those sites by coking.

In order to confirm the above mentioned conclusions, an additional experiment using a higher WHSV of 1474.5 mol ethanol h⁻¹ kg_{cat}⁻¹ and keeping constant the other parameters was performed with the NiFe-C773 catalyst. As shown in Figure 2.SI1 of the Appendix for chapter 2, similar observations in terms of product distribution can be derived, coupled to the expected decrease in ethanol conversion due to higher space velocity. The initial acetaldehyde selectivity reaches more than 80% and sharply decreases below 40% in the first 2 hours of reaction. Similarly to the results attained with low WHSV, reaction (2i) is activated within this time period with the corresponding decrease in acetaldehyde and increased methane selectivity. H₂ and CO₂ selectivity experience exactly the same trend than with lower WHSV, while CO and CH₄ selectivity values are lower due to the slow consumption of acetaldehyde under these conditions. This behavior also confirms that Ni⁰ particles are formed slowly over the NiFe-C773 catalyst, with the longest induction period.

Figure 2.8 depicts the conversion and product selectivity with time on stream over the Ni/Fe catalysts calcined at 1073 K. The ethanol conversion remains 100% over Ni₃Fe-C1073 and Ni₂Fe-C1073 only for ca. 1.5 hours, and immediately decreases over NiFe-C1073. This is the first important difference with respect to all catalysts calcined at 773 K, thus implying a better performance of the catalysts with mixtures Ni(Fe)O_x + NiFe₂O₄ with higher surface area (Table 2.2). Trends in H₂, CO₂ and CO selectivity are more or less similar in Ni₃Fe-C1073 and Ni₂Fe-C1073 during the first 3 hours of reaction, that is, all of them gradually decrease from the beginning of the reaction. However, other differences in these two catalysts appear, i.e. the CH₄ selectivity increases from 15% to 25% over Ni₃Fe-C1073 in the same time range, while it remains at ca. 10% till the end of the reaction in Ni₂Fe-C1073. It appears that the Ni₃Fe-C1073 catalyst, with the highest amount of Ni⁰ (Table 2.3 and Figure 2.SI2 in Appendix for chapter 2), exhibits a clear tendency for methanation using CO, CO₂ and H₂ present in the stream as reactants. Similarly to the catalysts Ni₃Fe and Ni₂Fe calcined at 773 K, this can be somehow expected attending to the high activity of nickel for methanation reactions of CO and CO₂ [17,66].

After 3 hours of reaction, the amount of CO₂ increases and it remains stable until the end of the reaction at a selectivity level of ca. 40%, while the H₂ content continues to decrease till 33%. It can be seen from the decrease in CO selectivity and increase in CO₂ that a certain degree of the water-gas-shift reaction (reaction 7) probably occurs in this time range. In parallel, acetaldehyde selectivity is growing, reaching a selectivity value of 20% at 5 hours of reaction, indicating that reaction (2ii) can be also hindered at longer reaction times. This explains the growth in acetaldehyde and the decrease in H₂ and CO.

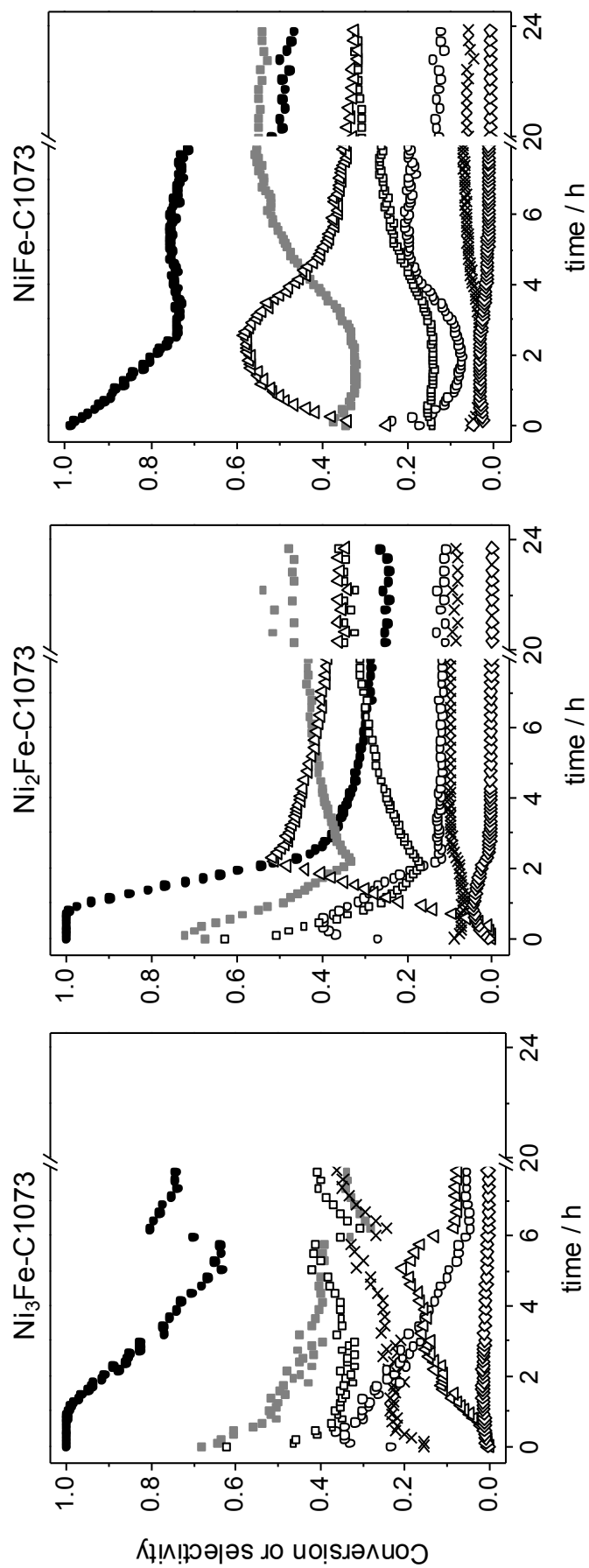


Figure 2.8. Ethanol conversion (\bullet) and selectivity to the different products (\times CH₄, \circ CO, \square CO₂, \triangle CH₃CHO, \diamond C₂H₄) vs time during ethanol steam reforming over the Ni-Fe catalysts calcined at 1073 K. Reaction conditions: H₂O/C₂H₅OH ratio = 6, $T = 773$ K, WHSV = 147.45 mol ethanol h⁻¹ kg_{cat}⁻¹, and $P = 1$ bar.

From this moment, the acetaldehyde content is reduced below 10%, and the amount of CH₄ keeps its growing tendency. This behavior suggests that the active sites for dehydrogenation and reforming experience a fast deactivation, thus decreasing the hydrogen productivity. The increased amount of CH₄ during the whole process occurring concomitantly to the CO decrease may indicate that only those sites responsible for methanation reaction persist over this catalyst. Also, an unexpected pressure rise occurred after 8 hours on stream, which forced to stop the reaction, caused by the clogging of the catalyst bed due to massive carbon deposition. As discussed later in section 3.2.3, the Ni₃Fe-C1073 catalyst experienced the largest carbon accumulation, and the high CH₄ selectivity over this catalyst may be attributed to the hydrogenation of carbonaceous deposits (reaction 9). However, it can be inferred that the low amount of ethylene may also suggest the fast polymerization into coke (reaction 3i).

When the amount of iron in the catalyst increases, i.e. using Ni₂Fe-C1073, the acetaldehyde selectivity increases into a maximum value of 51%, followed by a drop to ca. 36%. At this maximum point, the H₂ and CO₂ change their decreasing tendencies and gradually increase to ca. 46% and 32%, respectively. This behavior implies a high dehydrogenation activity towards acetaldehyde, followed by steam reforming and water-gas-shift, which are motivated by the decrease in Ni/Fe ratio of the catalyst.

Finally, the NiFe-C1073 catalyst appears to be rapidly deactivated due to the progressive decrease in ethanol conversion at the starting point of the reaction. In parallel, the amount of acetaldehyde increases to a maximum value of ca. 58% during the first 2 hours on stream. Meanwhile, H₂, CO and CO₂ experience the opposite effect, thus going through a minimum, which suggests the absence of acetaldehyde consumption by reaction (2i) and (2ii) in the beginning of the reaction. After this time, the ethanol conversion experiences a less pronounced drop, and the acetaldehyde decreases to 35% and remains constant till the end of the reaction. Due to the higher amount of iron in this catalyst, the catalyst becomes effective for acetaldehyde decarbonylation and steam reforming after 2 hours of reaction, as concluded

from the increase in H_2 , CO , CO_2 and CH_4 . Besides, the water-gas-shift can be also considered as an active reaction. It seems that, similarly to the NiFe-C773 catalyst, the induction period over the NiFe-C1073 catalyst is also relatively longer compared to catalysts with higher Ni/Fe ratios. Direct reforming reactions like (2ii) and reaction (7) become predominant with increasing time-on-stream, thus leading to higher hydrogen selectivity.

2.3.2.2 Effect of calcination conditions

In order to compare the different materials, Figure 2.9 plots the conversion and product distribution in terms of selectivity of all six catalysts at a fixed time on stream of 8 hours.

The selection of this time has been done based on the non-stable behavior of these catalysts, while considering a period of time in which major changes in gas composition have already arisen. From the previous results, it is worth noticing that the presence of a higher content in iron is beneficial for the production of H_2 and CO_2 , while keeping a high activity level. Iron is known to be active in CH_4 reforming [37], and this is probably the reason for the decreased CH_4 selectivity upon decreasing the Ni/Fe ratio from 3 to 1, whatever the calcination temperature (Figures 2.7 and 2.8). Besides, Ni exhibits a high CH_4 reforming capacity, as confirmed in previous works in the literature [30,36], which is boosted by the presence of higher Fe content.

Regarding the influence of the calcination temperature (773 or 1073 K), it appears that the catalysts calcined at the lowest temperature are more active and produce more H_2 and less CH_4 than the catalysts obtained after thermal treatment at 1073 K, especially in those materials containing a higher amount of Fe. In fact, general trends concerning the calcination temperature cannot be directly attained, as each material is supposed to be greatly affected by the presence of iron. That is, the Ni₃Fe-C1073 catalyst is more active (higher ethanol conversion) than the Ni₃Fe-C773 at 8 hours of reaction (Figure 2.9), while the opposite trend occurs with the other materials. It is important to remind that the catalysts are not pre-reduced.

As evidenced by XRD results in Figure 2.6 (and Figure 2.SI3 in Appendix for chapter 2), catalysts are conditioned under reaction conditions leading to metallic nickel after 24 h. Although the H₂ production does not seem to be affected by the calcination temperature for each series of catalysts, the relative amounts of CO, CO₂, CH₃CHO, and CH₄ vary in more or less extent whether the catalysts have been calcined at 773 K or at 1073 K, but also depend on the amount of iron. For example, after 8 hours of reaction, more acetaldehyde is produced with Ni₃Fe-C773 than with Ni₃Fe-C1073, and the contrary effect is observed with NiFe-C773 and NiFe-C1073 (Figure 2.9). Therefore, the catalyst activity has no clear correlation with calcination temperature. This result implies that the state of the nickel species under reaction conditions may be significantly different among catalysts. A calcination temperature of 773 K provided a suitable nickel state over Ni(Fe)O_x+ NiFe₂O₄ phase for steam reforming. The subsequent *in situ* reduction during reaction leads to the formation of Ni⁰ stabilized into the NiFe₂O₄ phase (as Ni(Fe)O_x is completely reduced in NiFe-C773, for example). As concluded from the Ni⁰ crystallite sizes in Table 2.3, large nickel sizes exist on the surface of catalysts calcined at 1073 K after reaction. In contrast, fine nickel crystallites are highly dispersed in catalysts calcined at 773 K and used in the reaction. This result is even more pronounced over catalysts with lower Ni/Fe ratios. Figure 2.SI2 in the Appendix for chapter 2 displays the distribution of phases calculated by means of XRD (Table 2.3). The catalyst showing a better performance in terms of conversion and selectivity (NiFe-C773) is the one containing less amount of metallic nickel and no Ni(Fe)O_x. In fact, nickel in the mixed oxide phase has been totally reduced upon reaction, leading to small Ni⁰ crystallites well dispersed in the NiFe₂O₄ matrix. In parallel, the amount of spinel is only slightly below that of the fresh catalyst (from 63 % to 57.7% in Tables 2.2 and 2.3), thus confirming the less reducible character of the NiFe₂O₄ phase. In contrast, higher amounts of metallic nickel (Ni₃Fe and Ni₂Fe catalysts, whatever the calcination temperature) are negative for the reaction since they rapidly induce deactivation (Figures 2.7, 2.8 and 2.9).

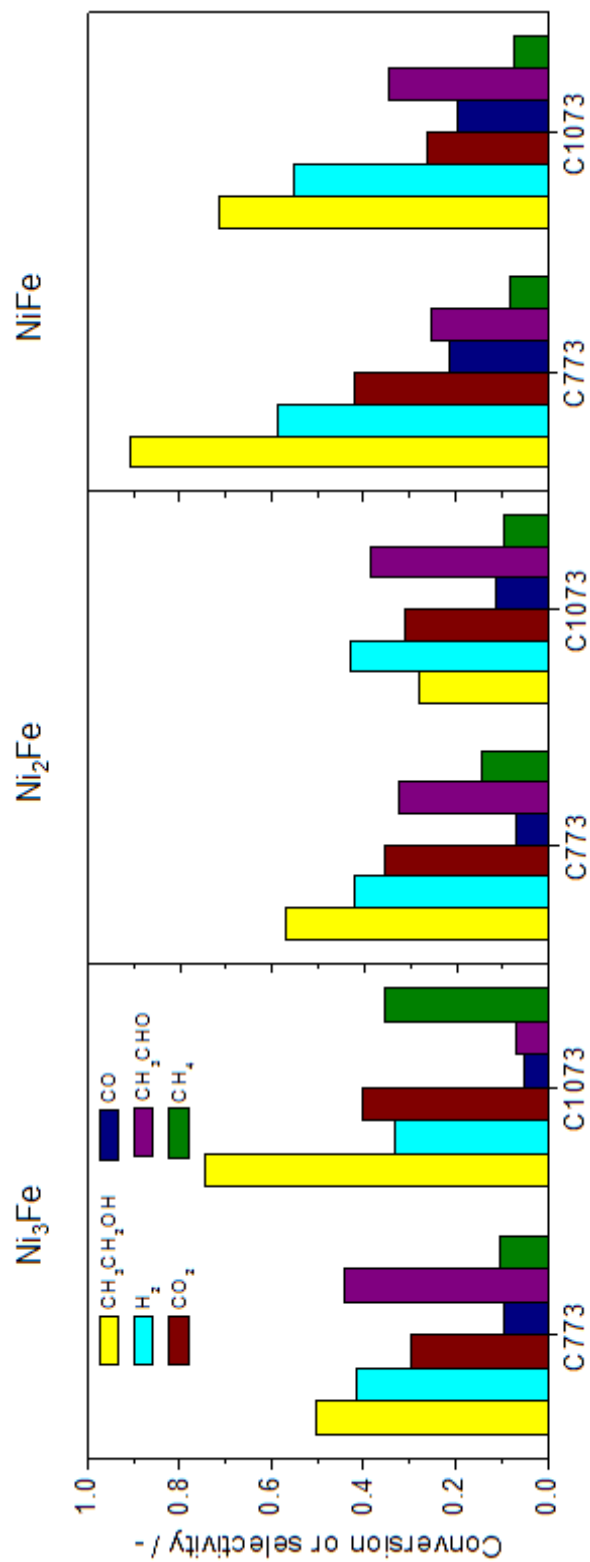


Figure 2.9. Ethanol conversion and selectivity to the different products during ethanol steam reforming over all Ni-Fe catalysts. Data represent averaged values of the 8 h reaction period in [Figures 2.7](#) and [2.8](#). Reaction conditions: H₂O/C₂H₅OH ratio = 6, T = 773 K, WHSV = 147.45 mol ethanol h⁻¹ kg_{cat}⁻¹, and P = 1 bar.

The difference in nickel crystallite size and its dispersion, and the differences in specific surface area of the original oxidic nickel phase should be responsible for the catalytic activity observed. The NiFe-C773 catalyst, which exhibited the highest surface area before reaction ($183 \text{ m}^2 \text{ g}^{-1}$) and smallest Ni^0 crystallite size upon reaction (13.9 nm) attained higher ethanol conversion, high H_2 and CO_2 selectivity and low amount of CH_4 than the other catalysts. Consequently, the presence of a higher amount of iron in this catalyst and the lower calcination temperature significantly affect the size of metallic nickel particles and their dispersion, which are dominant factors for ethanol steam reforming. These observations are in line with previous studies with Ni-based spinel oxides [47].

2.3.2.3 Characterization of used catalysts

The steam reforming performance over the Ni-Fe catalysts is determined by the nature of the oxidic nickel phase, which is induced by the calcination temperature leading to the formation of very small $\text{Ni}(\text{Fe})\text{O}_x$ and NiFe_2O_4 crystallites, and the Ni/Fe molar ratio. The complexity in the changes in product selectivity and the loss of activity of the different catalysts suggest that various types of sites and even different deactivation mechanisms may contribute to the overall reaction. In fact, the dominant reaction mechanism changes after approximately 3 hours on stream as observed in all cases. To appraise the changes in structure of the catalysts during the catalytic tests, the used materials were subsequently analyzed by TEM, TGA, Raman spectroscopy, and XRD as earlier presented.

One of the major issues in the catalytic reforming of hydrocarbons is catalyst deactivation caused by carbon deposition on the catalyst surface. This is in fact one of the main challenges for the industrial use of the ESR [11,13]. Sintering of the active metal is typically another reason for catalyst deactivation [19]. Taking into account that the catalysts are not reduced before the reforming reaction, the degree of sintering of metallic nickel particles from XRD (Figure 2.6) cannot be quantified, and therefore, deactivation by sintering cannot be

discarded. However, as shown in the Appendix for chapter 2 (Figure 2.SI3), the XRD pattern of the used NiFe-C773 catalyst after reaction at 773 K for 1 h displays the presence of metallic nickel reflections with lower intensity compared to those obtained after 24 h of reaction. This also confirms the slow *in situ* conditioning of the NiFe-C773 catalyst, which contains a lower amount of Ni⁰ at the expenses of Ni(Fe)Ox than the catalyst recovered after 24 h of reaction. The average crystallite size of this sample amounts 15 nm, which is very close to the average size obtained upon reaction for 24 h. In this sense, deactivation by sintering can be excluded at least in catalysts with Ni/Fe = 1, while this may be the cause for deactivation in catalysts with higher Ni/Fe ratios as larger Ni⁰ crystallite sizes are obtained.

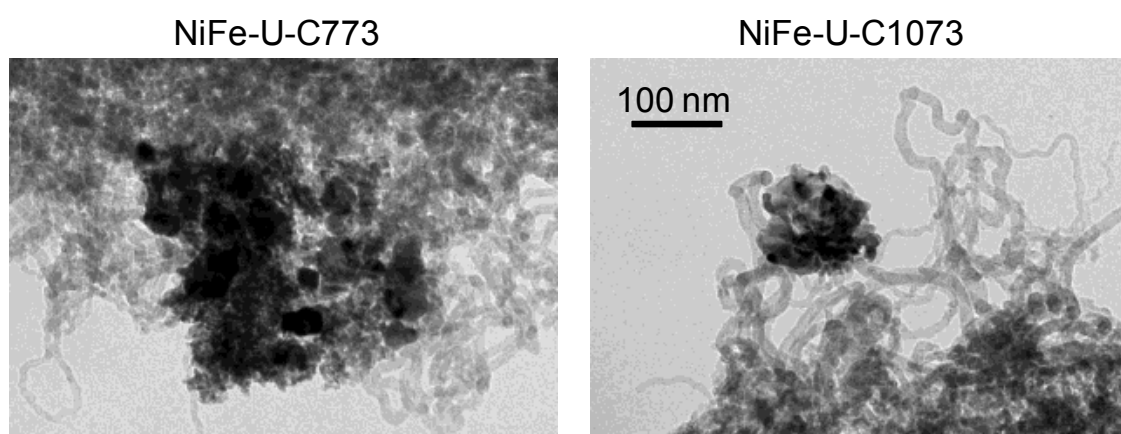


Figure 2.10. Selected transmission electron micrographs of the NiFe-U-C773 and NiFe-UC1073 samples. The same scale bar applies to both micrographs.

From inspection of all spent catalysts by TEM, it was apparent that carbonaceous deposits in the most common form of filaments (whiskers) [7] were present on all Fe-containing solids (Figure 2.10). Ni particles located at the tip apexes of the fibers are also clearly observed. As previously reported [67], this type of carbon does not immediately lead to catalyst deactivation. Whisker carbon results from adsorbed carbon atoms on a Ni particle, which diffuse and nucleate into a fiber. Normally, most of the nickel crystal is still active and only part of it is blocked by the growing of the carbon fiber. That would explain the gradual

deactivation of the catalysts in our ESR experiments. In contrast, the NiFe-C1073 sample deactivates more rapidly than the other catalysts. This can perhaps be explained by the formation of gum carbon (not discernible by TEM), caused by carbon encapsulation of the metal [67]. The fast degradation of catalytic activity in the catalysts calcined at 1073 K is in agreement with the work by Muroyama et al., in which a NiFe_2O_4 catalyst is quickly deactivated by its high tendency for coke formation [47].

An attempt was made to analyze the coke content on the used materials by means of TGA (not shown). However, the oxidation of metallic nickel during treatments in air interfered substantially, and therefore, an accurate quantification of the carbon content was difficult to achieve.

Average carbon balances during the reforming experiments were above 90% in all runs. Typically, carbon balances were worst during the first few hours of the experiment, and tended to improve at longer time on stream. This indicates that most of the carbon deposition took place during the in situ catalyst-conditioning period. Considering the average carbon balance for the first 8 hours of reaction (Table 2.3), the tendency towards carbon deposition of the catalysts was $\text{NiFe-U-C773} < \text{NiFe-U-C1073} < \text{Ni}_2\text{Fe-U-C1073} < \text{Ni}_3\text{Fe-U-C773} \sim \text{Ni}_2\text{Fe-U-C773} \sim \text{Ni}_3\text{Fe-U-C1073}$. This order agrees with the general trend in decay of catalytic activity shown in Figure 2.7 and 2.8, and with the larger amount of metallic nickel on the surface of catalysts with higher Ni/Fe ratios. Also, the size of Ni particles exerts a direct implication on carbon nucleation. As demonstrated by thermogravimetric experiments with two Ni catalysts having the same activity but different metal dispersion, the initiation of coke formation is retarded on the small nickel crystallites [68]. This would be in agreement with the lower carbon content on the NiFe-U-C773 and NiFe-U-C1073 samples, with small crystallite sizes (Table 2.3). XRD patterns of the used catalysts provided in Figure 2.6 also verified this trend. As mentioned in section 3.1.3, graphitic carbon was identified on the surface of the Ni_3Fe and Ni_2Fe catalysts calcined at 773 or 1073 K, while the intensity of the carbon band in the NiFe

catalysts was significantly lower. The latter observation is in agreement with the higher stable performance of the NiFe-C773 catalyst. Although the amount of carbon in NiFe-U-C1073 is relatively small compared to the other catalysts, this material displays an important and continuous decrease in ethanol conversion at the starting point of the reaction and an increase in acetaldehyde yield, thus pointing to a longer induction period to activate reactions (2i) and (2ii).

After 2 hours of reaction, the conversion becomes stable at ca. 70% and the steam reforming of acetaldehyde takes place. The decreased performance of this catalyst in terms of conversion could then be likely related to the presence of only 32% of metallic nickel (Table 2.3), which is much inferior to the percentage of Ni⁰ in the other catalysts.

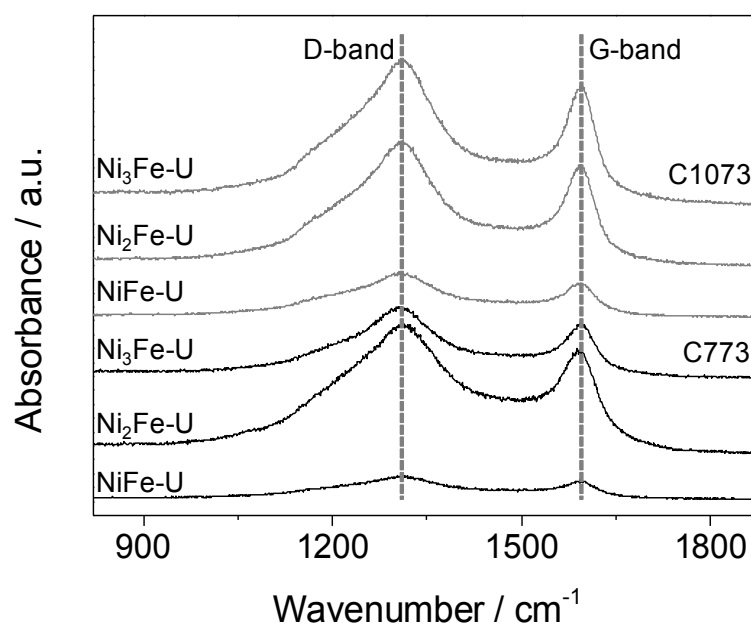


Figure 2.11. Raman spectra of the Ni-Fe catalysts after 24 h of reaction. Black and grey lines correspond to samples calcined at 773 K and 1073 K, respectively.

The nature and characteristics of carbon deposits were also studied by Raman spectroscopy. In Figure 2.11, the Raman spectra of used samples are shown in the range of 900-1900 cm⁻¹. Two intense bands at 1310 cm⁻¹ (typically called the D-band), which is associated with the vibrations of carbon atoms in disordered graphite planes, and at 1590 cm⁻¹

(called the G-band), assigned to the stretching mode of carbon sp^2 bonds of the typical graphite [69]. The band at 1353 cm^{-1} exhibits a higher intensity than the band at 1590 cm^{-1} . This indicates that disordered structures like amorphous carbon, carbon nanoparticles or filamentous carbon predominate in all the cases. The integrated intensity ratio of these two major bands ($R = I_D/I_G$) leads to the degree of graphitization of the carbon deposited on the catalysts. In fact, the R values decrease as the degree of graphitization of the carbon increases [70]. The spectra of the NiFe-U-C773 sample shows bands with low intensity, practically matching the spectra of the fresh catalyst (not shown), which is a clear evidence that carbon deposition is practically negligible. The order of R values for the other samples displays the order NiFe-U-C1073 > NiFe-U-C773 > Ni₃Fe-U-C773 > Ni₂Fe-U-C773 > Ni₂Fe-U-C1073 > Ni₃Fe-U-C1073. This sequence indicates the higher tendency of the fresh Ni₃Fe-C1073 sample to produce more graphitized carbon under reaction conditions, due to the larger amount of Ni⁰ on the catalyst (68.7% based in the percentage of crystalline phases in Table 2.3), and the larger size (33.3 nm) and low dispersion of such particles.

In summary, the results attained for this series of catalysts are in agreement with previous studies using iron-doped cobalt based catalysts, in which iron promotes acetaldehyde reforming, and suppresses carbon deposition [71].

2.4. Conclusions

The steam reforming of ethanol over Ni-Fe mixed oxides derived from reevesites (Ni-Fe hydrotalcites) was investigated, and the influence of the iron content and the calcination temperature on the catalytic performance was evaluated. Proper selection of the activation conditions, that is, calcination of the reevesite precursors, is critical for the catalytic behavior, as it determines the nature of the oxide (the percentage of crystalline phases, i.e. Ni(Fe)Ox and NiFe₂O₄) and affects the final size and dispersion of nickel species formed during the reaction. Also, the chemical and activity properties of the derived mixed oxides are affected

by the amount of iron, which exhibits a positive role in nickel-based catalysts. This is due to the enhancement of catalytic activity and hydrogen selectivity induced by the improved dispersion of nickel and the alleviation in carbon deposition. The best catalyst, with a Ni/Fe ratio of 1 and calcined at 773 K, rendered high and stable hydrogen selectivity of up to ca. 60%, low methane content, and consisted of a mixture of Ni(Fe)O_x solid solution and NiFe₂O₄ with very small crystallites. Crystallization and growing of NiFe₂O₄ at high calcination temperature (1073 K) associated with higher carbon deposition and probably Ni⁰ sintering lead to lower activity and fast deactivation. Lower Ni/Fe ratios strongly promote ethanol dehydrogenation and acetaldehyde decarbonylation followed by steam reforming likely due to the promotion effect of Fe/Fe²⁺ on the metallic nickel particles. However, after some time on stream, all catalysts point to a poor activity for acetaldehyde conversion, concomitantly to variations in H₂, CO, CO₂ and CH₄, which indicates their limited activity to transform acetaldehyde to C1 products. High surface area, higher iron content, lower reducibility of nickel species and small nickel crystallite size lead to a higher activity in ethanol dehydrogenation, acetaldehyde decarbonylation and reforming, and WGS. The derived nickel-iron hydrotalcite catalysts show great potential to be used in the ethanol steam reforming, with high activity and selectivity for hydrogen production. Some aspects need to be studied to increase the stability of these materials, and they are actually under current investigation.

2.5. References

- [1] U.S. Energy Information Administration, "Annual Energy Review 2010" to be found under <http://www.eia.gov/totalenergy/data/annual/index.cfm> (accessed March 2012).
- [2] M. Ball, M. Wietschel (Eds.), *The Hydrogen Economy. Opportunities and Challenges*, Cambridge University Press, New York, 2009.
- [3] International Energy Agency, "Key World Energy Statistics" to be found under http://www.iea.org/textbase/nppdf/free/2011/key_world_energy_stats.pdf (accessed February 2012).
- [4] A. Demirbas, *Biofuels. Securing the Planet's Future Energy Needs*, Springer-Verlag, New York, 2009.
- [5] R.B. Gupta, A. Demirbas, *Gasoline, diesel, and ethanol biofuels from grasses and plants*, Cambridge University Press, New York, 2010.
- [6] M. Ni, D.Y.C. Leung, M.K.H. Leung, *Int. J. Hydrogen Energy* 32 (2007) 3238-3247.
- [7] R.M. Navarro, M.A. Peña, J.L.G. Fierro, *Chem. Rev.* 107 (2007) 3952-3991.
- [8] L. De Rogatis, P. Fornasiero, in: P. Barbaro, C. Bianchini (Eds.), *Catalysis for Sustainable Energy Production*, Wiley-VCH Verlag, Weinheim, 2009, p. 171.
- [9] K. Egeblad, J. Rass-Hansen, C.C. Marsden, E. Taarning, C.H. Christensen, in: J.J. Spivey, K.M. Dooley (Eds.), *Catalysis*, The Royal Society of Chemistry, Cambridge, 2009, pp. 13-50.
- [10] A.J. Vizcaíno, A. Carrero, J.A. Calles, *Int. J. Hydrogen Energy* 32 (2007) 1450-1461.
- [11] A. Haryanto, S. Fernando, N. Murali, S. Adhikari, *Energy Fuels* 19 (2005) 2098-2106.
- [12] A. Bshish, Z. Yakoob, B. Narayanan, R. Ramakrishnan, A. Ebshish, *Chem. Papers* 65 (2011) 251-266.
- [13] P.D. Vaidya, A.E. Rodrigues, *Chem. Eng. J.* 117 (2006) 39-49.
- [14] A. Denis, W. Grzegorzczak, W. Gac, A. Machocki, *Catal. Today* 137 (2008) 453-459.
- [15] A.N. Fatsikostas, X.E. Verykios, *J. Catal.* 225 (2004) 439-452.
- [16] G.F. Froment, *Catal. Rev.* 50 (2008) 1-18.
- [17] R.R. Davda, J.W. Shabaker, G.W. Huber, R.D. Cortright, J.A. Dumesic, *Appl. Catal. B* 56 (2005) 171-186.
- [18] C. Resini, T. Montanari, L. Barattini, G. Ramis, G. Busca, S. Presto, P. Riani, R. Marazza, M. Sisani, F. Marmottini, U. Costantino, *Appl. Catal. A* 355 (2009) 83-93.
- [19] L. He, H. Berntsen, E. Ochoa-Fernández, J.C. Walmsley, E.A. Blekkan, D. Chen, *Top. Catal.* 52 (2009) 206-217.
- [20] X.-P. Yu, W. Chu, N. Wang, F. Ma, *Catal. Lett.* 141 (2011) 1228-1236.
- [21] W.T. Reichle, *J. Catal.* 94 (1985) 547-557.
- [22] F. Cavani, F. Trifirò, A. Vaccari, *Catal. Today* 11 (1991) 173-301.
- [23] D. Tichit, C. Gérardin, R. Durand, B. Coq, *Top. Catal.* 39 (2006) 89-96.
- [24] D. Tichit, B. Coq, *CATTECH* 7 (2003) 206-217.
- [25] A. Vaccari, *Catal. Today* 41 (1998) 53-71.

- [26] J. Comas, M.L. Dieuzeide, G. Baronetti, M. Laborde, N. Amadeo, *Chem. Eng. J.* 118 (2006) 11-15.
- [27] V. Mas, M.L. Dieuzeide, M. Jobbágy, G. Baronetti, N. Amadeo, M. Laborde, *Catal. Today* 133-135 (2008) 319-323.
- [28] I.O. Cruz, N.F.P. Ribeiro, D.A.G. Aranda, M.M.V.M. Souza, *Catal. Commun.* 9 (2008) 2606-2611.
- [29] V. Mas, G. Baronetti, N. Amadeo, M. Laborde, *Chem. Eng. J.* 138 (2008) 602-667.
- [30] G. Busca, U. Costantino, T. Montanari, G. Ramis, C. Resini, M. Sisani, *Int. J. Hydrogen Energy* 35 (2010) 5356-5366.
- [31] M. Li, X. Wang, S. Li, S. Wang, X. Ma, *Int. J. Hydrogen Energy* 35 (2010) 6699-6708.
- [32] A.F. Lucrédio, J.D.A. Bellido, E.M. Assaf, *Appl. Catal. A* 388 (2010) 77-85.
- [33] A. Romero, M. Jobbágy, M. Laborde, G. Baronetti, N. Amadeo, *Catal. Today* 149 (2010) 407-412.
- [34] A.J. Vizcaíno, M. Lindo, A. Carrero, J.A. Calles, *Int. J. Hydrogen Energy* (2012) 1985-1992.
- [35] Z. Ping Xu, J. Zhang, M.O. Adebajo, H. Zhang, C. Zhou, *Appl. Clay Sci.* 53 (2011) 139-150.
- [36] R. Guil-López, R.M. Navarro, M.A. Peña, J.L.G. Fierro, *Int. J. Hydrogen Energy* 36 (2011) 1512-1523.
- [37] L. Huang, Q. Liu, R. Chen, A.T. Hsu, *Appl. Catal. A* 393 (2011) 302-308.
- [38] L. Huang, J. Xie, R. Chen, D. Chu, W. Chu, A.T. Hsu, *Int. J. Hydrogen Energy* 33 (2008) 7448-7456.
- [39] L. Huang, J. Xie, W. Chu, R. Chen, D. Chu, A.T. Hsu, *Catal. Commun.* 10 (2009) 502-508.
- [40] S.A. de Waal, E.A. Viljoen, *Amer. Miner.* 56 (1971).
- [41] A.S. Bookin, V.I. Cherkashin, V.A. Drits, *Clays Clay Miner.* 41 (1993) 631-634.
- [42] E. Uzunova, D. Klissurski, S. Kassabov, *J. Mater. Chem.* 4 (1994) 153-159.
- [43] S. Abelló, S. Mitchell, M. Santiago, G. Stoica, J. Pérez-Ramírez, *J. Mater. Chem.* 20 (2010) 5878-5887.
- [44] K.T. Ehlissen, A. Delahaye-Vidal, P. Genin, M. Figlarz, P. Willmann, *J. Mater. Chem.* 3 (1993) 883-888.
- [45] F.B.D. Saiah, B.-L. Su, N. Bettahar, *Macromol. Symp.* 273 (2008) 125-134.
- [46] M. Tu, J. Shen, Y. Chen, *Thermochim. Acta* 302 (1997) 117-124.
- [47] H. Muroyama, R. Nakase, T. Matsui, K. Eguchi, *Int. J. Hydrogen Energy* 35 (2010) 1575-1581.
- [48] L.E. Alzamora, J.H. Ross, E.C. Kruissink, L.L. van Reijen, *J. Chem. Soc. Faraday Trans.* 77 (1981) 665-681.
- [49] O. Clause, B. Rebours, E. Merlen, F. Trifiró, A. Vaccari, *J. Catal.* 133 (1992) 231-246.

- [50] D.C. Puxley, I.J. Kitchener, C. Komodromos, N.D. Parkyns, in: G. Poncelet, P. Grange, P.A. Jacobs (Eds.), *Preparation of Catalysts III*, Stud. Surf. Sci. Catal., Elsevier Science, 1983, pp. 237-271.
- [51] S. Abelló, D. Verboekend, B. Bridier, J. Pérez-Ramírez, *J. Catal.* 259 (2008) 85-95.
- [52] A.L. McKenzie, C.T. Fishel, R.J. Davis, *J. Catal.* 138 (1992) 547-561.
- [53] F. Basile, G. Fornasari, M. Gazzano, A. Vaccari, *Appl. Clay Sci.* 16 (2000) 185-200.
- [54] M. del Arco, P. Malet, R. Trujillano, V. Rives, *Chem. Mater.* 11 (1999) 624-633.
- [55] R.L. Frost, K.L. Erickson, *J. Thermal Anal. Calorim.* 76 (2004) 217-225.
- [56] L. Ma, K. Zhou, Z. Li, Q. Wei, L. Zhang, *Corrosion Sci.* 53 (2011) 3712-3724.
- [57] J.A.C. de Paiva, M.P.F. Graça, J. Monteiro, M.A. Macedo, M.A. Valente, *J. Alloys Compd.* 485 (2009) 637-641.
- [58] A. Ahlawat, V.G.Sathe, V.R.Reddy, A. Gupta, *J. Magn. Magn. Mater.* 323 (2011) 2049-2054.
- [59] J. Nan, Y. Yang, Z. Lin, *Electrochim. Acta* 51 (2006) 4873-4879.
- [60] K.V.R. Chary, P.V.R. Rao, V. Vishwanathan, *Catal. Commun.* 7 (2006) 974-978
- [61] O. Clause, M.G. Coelho, M. Gazzano, D. Matteuzzi, F. Trifirò, A. Vaccari, *Appl. Clay Sci.* 8 (1993) 169-186.
- [62] M.S. Lee, J.Y. Lee, D.-W. Lee, D.J. Moon, K.-Y. Lee, *Int. J. Hydrogen Energy* 37 (2012) 11218-11226.
- [63] R. Benrabaa, A. Löfberg, A. Rubbens, E. Bordes-Richard, R.N. Vannier, A. Barama, *Catal. Today* (2013) 188-195.
- [64] Z. Yu, D. Chen, M. Rønning, T. Vrålstad, E. Ochoa-Fernández, A. Holmen, *Appl. Catal. A* 338 (2008) 136-146.
- [65] D. Montané, E. Bolshak, S. Abelló, *Chem. Eng. J.* 175 (2011) 519-533.
- [66] I. Chorkendorff, J.W. Niemantsverdriet, *Concepts of Modern Catalysis and Kinetics*, Wiley-VCH Verlag GmbH & Co, Weinheim, 2003.
- [67] J. Rass-Hansen, C.H. Christensen, J. Sehested, S. Helveg, J.R. Rostrup-Nielsen, S. Dahl, *Green Chem.* 9 (2007) 1016-1021.
- [68] H.S. Bengaard, J.K. Nørskov, J.S. Sehested, B.S. Clausen, L.P. Nielsen, A.M. Molenbroek, J.R. Rostrup-Nielsen, *J. Catal.* 209 (2002) 365-384.
- [69] A.E. Galetti, M.F. Gomez, L.A. Arrúa, M.C. Abello, *Appl. Catal. A* 348 (2008) 94-102.
- [70] P. Lespade, A. Marchand, M. Couzi, F. Cruege, *Carbon* 22 (1984) 375-385.
- [71] A. Kazama, Y. Sekine, K. Oyama, M. Matsukata, E. Kikuchi, *Appl. Catal. A* 383 (2010) 96-101.

2.6. Appendix for chapter 2:

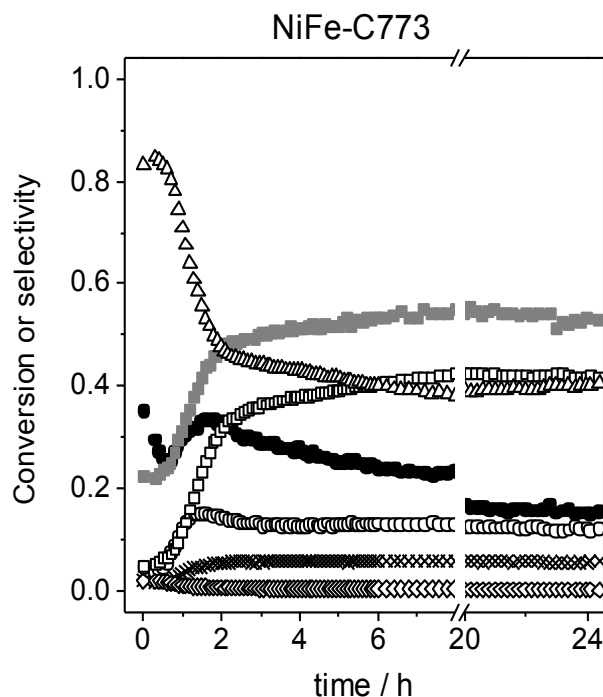


Figure 2.SI1. Ethanol conversion (●) and selectivity to the different products (■ H_2 , × CH_4 , ○ CO , □ CO_2 , △ CH_3CHO , ◇ C_2H_4) vs time during ethanol steam reforming over the NiFe-C773. Reaction conditions: $\text{H}_2\text{O}/\text{C}_2\text{H}_5\text{OH}$ ratio = 6, $T = 773$ K, $\text{WHSV} = 1474.5$ mol ethanol $\text{h}^{-1} \text{kg}_{\text{cat}}^{-1}$, and $P = 1$ bar.

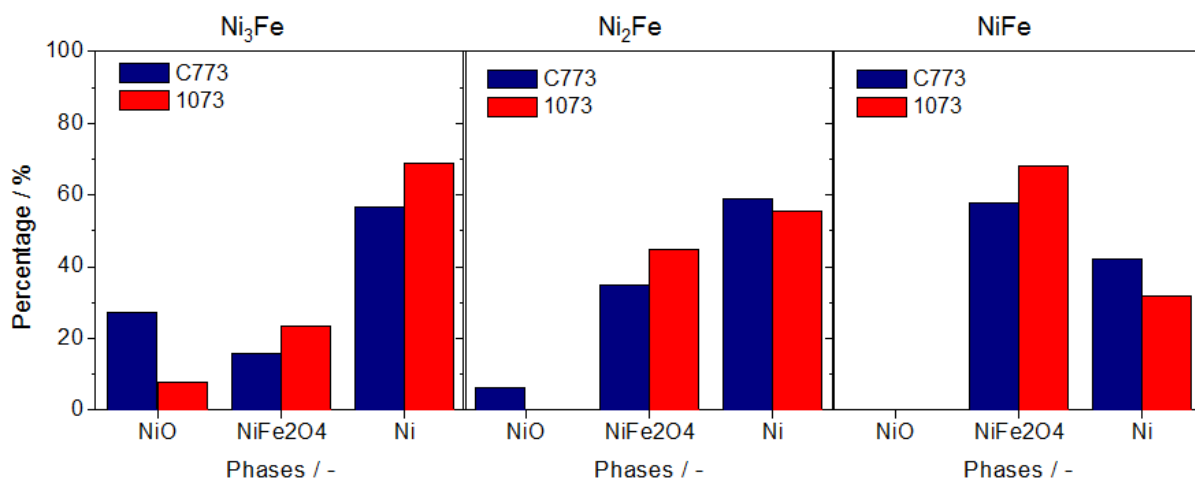


Figure 2.SI2. Percentage of crystalline phases determined by XRD Rietveld refinement of the catalysts after a 24 h reaction period.

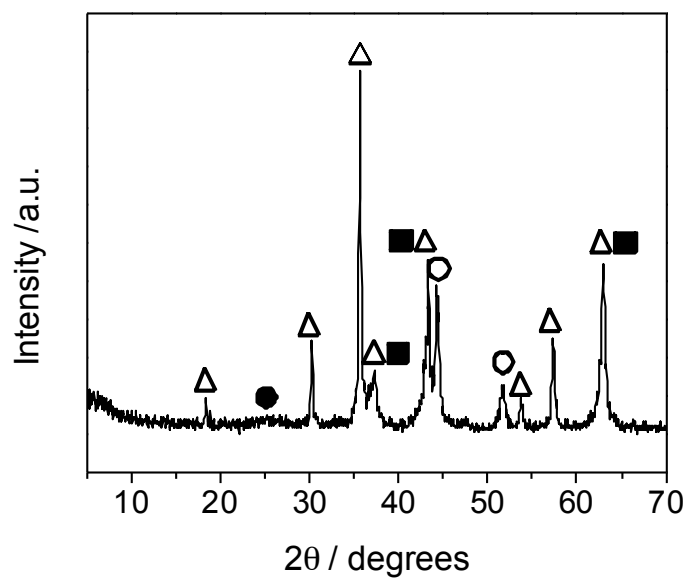


Figure 2.SI3. XRD patterns of the used NiFe-C773 sample after reaction at 773 K for 1 h.
Crystalline phases: (○) Ni, (Δ) NiFe₂O₄ (and/or Fe₃O₄).

Chapter 3

Ethanol steam reforming over Ni-Fe-based hydrotalcites: effect of iron content and reaction temperature

Ethanol steam reforming has been evaluated over nickel-iron based hydrotalcite-like compounds with Ni/Fe molar ratios of 1 and 0.5. Calcined materials have been characterized by XRD, TEM, BET and TPR. The introduction of iron leads to the formation of a mixture of Ni(Fe)O_x and spinel phase upon calcination, which results in variations of structural and catalytic properties. With a Ni/Fe ratio of 1, a remarkable improvement in catalytic activity as well as selectivity to hydrogen is observed with respect to the catalyst with Ni/Fe ratio of 0.5. This is due to the enhanced nickel dispersion, the high surface area, and small Ni⁰ crystallite size over the Ni(Fe)O_x + NiFe₂O₄ mixture. However, a further increase in iron content leads to the formation of a low surface area spinel phase (NiFe₂O₄), which results in lower activity and faster deactivation in the reaction through Ni⁰ sintering. The effect of reaction temperature has been evaluated over the most active catalyst (Ni/Fe=1).

This chapter is based on the following publication:

E. Bolshak, S. Abelló, D. Montané. *Int. J. Hydr. Energy*, 38:14, (2013) 5594-5604

3.1. Introduction

Hydrogen is considered to be a potential energy vector from an economic, technical, and environmental point of view since it can be obtained from renewable sources through thermal or catalytic processes [1,2]. The generation of hydrogen from bio-ethanol can be catalytically carried out in the presence of steam ($C_2H_5OH + 3H_2O \rightarrow 2CO_2 + 6H_2$), and exhibits the additional advantage of being nearly CO_2 neutral if ethanol is produced from dedicated, non-food energy crops and waste biomass [3]. A cost-effective application is for autonomous hydrogen generators (fuel processors) to produce hydrogen *in situ* in power systems based on low-temperature fuel cells [4,5].

Ethanol steam reforming can be performed with several groups of catalysts. The most common catalysts are normally based on metals (Co, Ni, Ni/Cu and noble metals) supported on single metal oxides or mixed oxides. The catalysts most stable and selective to hydrogen are those based on noble metals (mainly Rh and Ru) supported on different metal-oxides (like La_2O_3 , CeO or MgO) [3]. They reach complete ethanol conversion and more than 90% selectivity to hydrogen at 700°C. The support plays a determinant role not only because of its high surface area and proper metal dispersion, but also because of its chemical nature [6,7]. The major drawback of noble metal-based catalysts is their high cost, even with relatively small metal loadings (1-3%), which make their industrial-scale application for ethanol reforming uncertain. Another important group of ethanol reforming catalysts is based on non-noble metals supported on metal oxides. Cobalt is one of the active metals that has been studied in detail, either alone [8, 9] and with the addition of dopants such alkali metals [10], Fe or Mn [11]. Nickel is particularly interesting for steam reforming reactions since it favors the scission of C-C bonds and promotes hydrogenation/dehydrogenation reactions. Although it exhibits high activity and low cost, it suffers from deactivation by sintering of the metal and coke deposition [6]. Ethanol reforming at low temperature (i.e., below 500°C) has been investigated with Ni on several metal oxide supports [12-15]. Nickel-containing spinels,

consisting of binary mixtures of ZnAl_2O_4 and NiAl_2O_4 spinel with several ratios, were also tested showing complete conversion of ethanol and good selectivity towards hydrogen and carbon monoxide with Ni loadings above 18% [16].

One of the challenges to develop successful catalysts for ethanol reforming is, however, to combine the properties of the support and active metals into a stable structure, a catalyst that can withstand the harsh conditions of temperature and water concentration employed for reforming, while preventing deactivation by sintering and carbon deposition. Among different strategies, precursor materials based on layered double hydroxides (LDH) are simple and inexpensive to synthesize on laboratory and industrial scales [17], and yield oxide mixtures upon calcination with very high metal interdispersion and surface area [18,19]. Various combinations of metals have been used to prepare oxides derived from LDH for ethanol reforming. In our previous work [20], we found that Ni-Fe mixed oxides were active catalysts for the reaction. The effect of increasing the iron amount (from a molar ratio Ni/Fe 3 to 1) on the resulting oxides was found to be decisive to enhance the catalytic activity and hydrogen selectivity by the improved nickel dispersion and reduced coke deposition; that is, the best catalyst was obtained with a 1:1 Ni/Fe molar ratio. Besides, the calcination temperature exerted an important role in the reforming performance, thus producing a $\text{Ni(Fe)O}_x + \text{NiFe}_2\text{O}_4$ mixture upon calcination at 500°C , with high surface area, lower reducibility of nickel species, small Ni^0 crystallites, and a significant content of spinel (ca. 60%). This contrasted with the lower activity and faster deactivation upon treatment of the precursor at 900°C , which induced the formation of a low surface area NiFe_2O_4 spinel-supported Ni catalyst. This was also the cause for deactivation in the work by Muroyama et al. [21]. In their work, H_2 and CO_2 selectivity decreased soon after the reaction started due to carbon deposition, which was caused by ethanol dehydration over a spinel-based catalyst.

Judging from the significant content of spinel phase in the $\text{Ni(Fe)O}_x + \text{NiFe}_2\text{O}_4$ mixture and its high surface area, it is interesting to evaluate the effect of further increasing

the iron content for spinel formation at low calcination temperature in the steam reforming performance. Following our previous study, we expand the range of Ni/Fe ratios below 1 to systematically investigate the formation of Ni⁰ supported spinel-based Ni-Fe catalysts. Activity measurements have been complemented by detailed characterization techniques (XRD, TEM, TPR, and Raman) to derive conclusions on the appropriate phase composition for H₂ production. In addition, the influence of reaction temperature on the selectivity of the different products has been evaluated over the most active catalyst.

3.2. Experimental

3.2.1. Catalyst preparation and activation

Nickel-iron hydrotalcites with nominal molar ratios of 1 and 0.5 were synthesized by coprecipitation at constant pH. Briefly, aqueous solutions of 1M of Ni(NO₃)₂·6H₂O and 1M of Fe(NO₃)₃·9H₂O and the precipitating agent (NaOH/Na₂CO₃, 1M of each) were simultaneously fed into a vessel by a 905 Titrand® automated titrator (Metrohm AG) equipped with two 800 Dosino® dosing systems. The pH was maintained at a constant value of 10 (±0.2). The resulting slurry was aged at 30°C for 15 h under vigorous stirring. The precipitate was filtered and washed with deionized water and then dried at 80°C during 12 hours. The samples were calcined in static air at 500°C for 6 h using a heating rate of 5°C min⁻¹. Along the manuscript, the materials are identified as precursor (Ni_xFe-P), calcined (Ni_xFe-C) and after use in the reaction (Ni_xFe-U), where x denotes the Ni/Fe molar ratio (1 or 0.5).

3.2.2. Catalyst characterization

The chemical composition of the solids was determined by inductively coupled plasma-optical emission spectroscopy (ICP-OES) in a in a Spectro Arcos 165 spectrophotometer. Before analysis, the solids were dissolved in 1% HNO₃ aqueous solution. Powder X-ray

diffraction patterns were acquired in a Siemens D5000 diffractometer with Bragg-Brentano geometry using Ni-filtered Cu-K α radiation. Data were collected in the 2θ range of 5-70° with an angular step of 0.05° and a counting time of 3 s per step. The quantitative phase content and crystallite sizes were determined by a multiphase Rietveld refinement using the Diffrac-Plus Topas software (Bruker AXS GmbH, Germany, version 4.0). Transmission electron microscopy (TEM) was carried out in a JEOL JEM-1011 microscope operated at 100 kV (or 80kV for precursor samples). A few droplets of the sample suspended in ethanol were placed on a carbon-coated copper grid followed by evaporation at ambient conditions. N₂ adsorption isotherms were measured on a Quantachrome Quadrasorb-SI gas-adsorption analyzer at 77 K. Prior to the measurements, the as-prepared and calcined samples were degassed in vacuum at 120°C and 300°C for 10 h, respectively. Thermogravimetric analysis-differential scanning calorimetry (TGA-DSC) was measured in a Mettler Toledo TGA/DSC 1 microbalance. Analyses were performed in air (20 cm³ STP min⁻¹) increasing the sample temperature from 25°C to 1000°C at 5°C min⁻¹. Temperature-programmed reduction with hydrogen (H₂-TPR) was measured in a ChemBet Pulsar TPR/TPD unit equipped with a thermal conductivity detector. Ca. 50 mg of Ni-Fe oxide obtained by calcination of the hydrotalcite precursors at 500°C were loaded in the U-quartz microreactor, pretreated in air (20 cm³ STP min⁻¹) at 300°C for 1 h, and cooled to 50 °C in the same atmosphere. The analysis was carried out in a mixture of 5 vol% H₂ in N₂ (20 cm³ STP min⁻¹), ramping the temperature from 50°C to 900°C at 10 K min⁻¹. Raman spectra were recorded at room temperature using a Renishaw InVia Raman Spectrometer equipped with confocal DM 2500 Leica optical microscope, a CCD detector, and a diode laser operating at 785 nm. The applied power of the laser beam focusing on the sample was 3 mW. The spectra were measured in the 90-2000 cm⁻¹ range in single scan with 30 s of exposure time.

3.2.3. Catalytic tests

Ethanol steam reforming was carried out at atmospheric pressure in a fixed-bed stainless steel reactor (internal diameter of 10 mm), which has been described elsewhere [20]. The reactor was filled with 0.5 g of catalyst particles sieved to 100-300 μm , diluted with 10 grams of SiO_2 particles of the same size. The reagent feed was an ethanol and water mixture with a molar ratio of 1:6 (a steam to carbon ratio, S/C, of 3:1). The feed rate was 0.2 mL min^{-1} , which corresponded to a weight hourly space velocity (WHSV) of $147.45 \text{ mol ethanol h}^{-1} \text{ kg}_{\text{cat}}^{-1}$. Each sample of catalyst was tested for at least 24 h at constant conditions, and the spent catalyst was then collected for further characterization. The reaction temperature was varied from 400 to 600 $^{\circ}\text{C}$ in selected experiments. Reaction products were quantified with an on-line gas chromatograph (Agilent 3000A microGC). A constant flow of N_2 (500 NmL min^{-1}) was added at the reactor outlet to dilute the products and avoid condensation of water in the microGC internals and the sampling line, which was heat-traced at 120°C .

Ethanol conversion (X_{EtOH}), product selectivity (S_k) and carbon balance (%CB) were calculated with equations 1 to 4, where F_j is the molar flow of product j , and nC_j is the number of carbon atoms in product j .

$$X_{\text{EtOH}} = \frac{F_{\text{EtOH},0} - F_{\text{EtOH}}}{F_{\text{EtOH},0}} \quad (\text{eq. 3.1})$$

$$S_j = \frac{nC_j \cdot F_j}{2(F_{\text{EtOH},0} - F_{\text{EtOH}})} \quad (\text{eq. 3.2})$$

$$S_{\text{H}_2} = \frac{F_{\text{H}_2}}{6(F_{\text{EtOH},0} - F_{\text{EtOH}})} \quad (\text{eq. 3.3})$$

$$\%CB = \frac{\sum_j (nC_j \cdot F_j)}{2(F_{\text{EtOH},0} - F_{\text{EtOH}})} \quad (\text{eq. 3.4})$$

3.3. Results and discussion

3.3.1 Characterization of as-synthesized and calcined samples.

Figure 3.1 shows the XRD patterns of the samples NiFe-P and Ni_{0.5}Fe-P and their corresponding products of calcination at 500°C – NiFe-C and Ni_{0.5}Fe-C. The as-synthesized samples display the characteristic reflections of reevesite with formula Ni₆Fe₂(OH)₂(CO₃)₁₆·4H₂O. However, broader and less intense peaks compared to the pure reevesite sample [22] are observed, namely as a consequence of the lower crystallinity in these samples. This is in part motivated by the non-typical stoichiometry of the as-prepared samples. No reflections associated with single metal hydroxides were visible in any of the samples. However, part of iron may exist as an amorphous hydroxide carbonate phase. Chemical analysis showed that the Ni/Fe molar ratio in the solids was 0.52 and 1.02 for Ni_{0.5}Fe-P and NiFe-P, respectively.

The solids calcined at 500°C showed reflections of the NiO structure (bunsenite, powder diffraction file 03-065-2901 from ICDD) and NiFe₂O₄ spinel (trevorite, powder diffraction file 54-0964 from ICDD). As concluded in our previous work [20], calcination of the hydrotalcite structure leads to the formation of a metastable mixed oxide phase, recognized as Ni(Fe)O_x, which is transformed into NiFe₂O₄, especially at high calcination temperature. Here, the diffraction lines related to NiFe₂O₄, which are coincident in 2θ position with those of NiO, are clearly discerned at 500°C and are far more intense in the Ni_{0.5}Fe-C sample. This is explained by the non-typical stoichiometry of the hydrotalcite precursor, which is defective in Ni atoms, thus leading preferentially to the spinel structure upon calcination.

A quantitative analysis of the phases present in the calcined samples was performed by Rietveld refinement (Table 3.1). Based on the crystalline phases, trevorite was the main phase (94.9%) in Ni_{0.5}Fe-C, while it only reaches 62% in NiFe-C. As expected, the increase in iron content in the reevesite precursors induced a lower amount of NiO upon calcination [20].

Interestingly, the Ni_{0.5}Fe-C sample showed a considerable presence of hematite (α -Fe₂O₃), which was never detected in samples with higher Ni/Fe ratios. Table 3.2 displays the average crystallite size of the calcined samples obtained from the refinement method. The NiFe-C sample showed NiO crystallites with sizes around 3.5 nm and smaller sizes of spinel. In contrast, the Ni_{0.5}Fe-C sample presented larger NiFe₂O₄ crystallites (of around 10 nm) and bigger Fe₂O₃ crystallites.

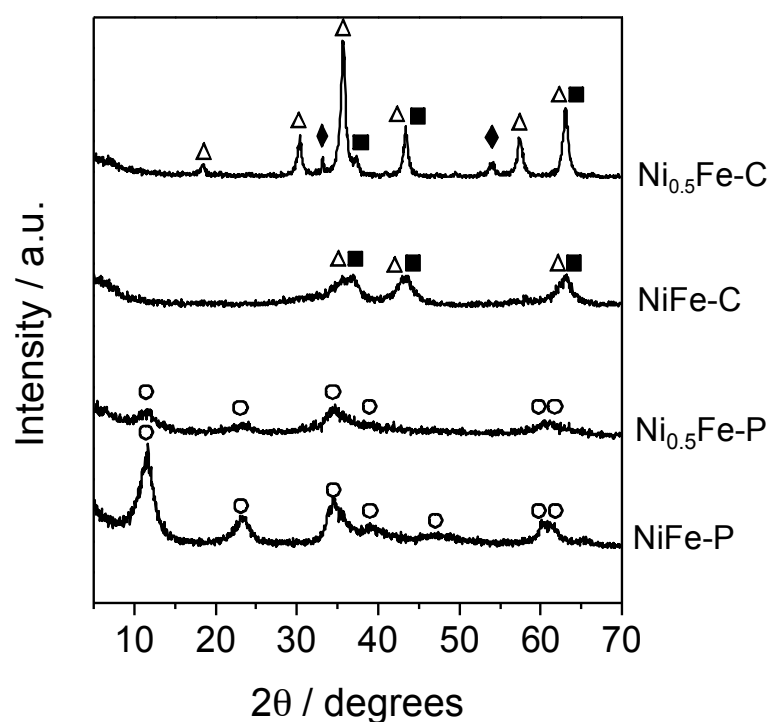


Figure 3.1. XRD patterns of precursors and calcined samples with Ni/Fe ratios 1:1 and 0.5:1. Crystalline phases: (■) NiO, (Δ) NiFe₂O₄, (○) reevesite, (◆) Fe₂O₃.

Table 3.1: Crystalline phase composition of the different catalysts.

Sample	Phase composition / %			
	NiO	NiFe ₂ O ₄	Ni	Fe ₂ O ₃
NiFe-C	37.1	62.9	-	-
Ni _{0.5} Fe-C	-	94.9	-	5.1
Ni _{0.5} Fe-U	-	84.7	15.3	-
NiFe-U, T = 400°C	-	59.1	40.9	-
NiFe-U, T = 500°C	-	57.7	42.3	-
NiFe-U, T = 600°C	-	53.6	46.4	-

Figure 3.2 shows the results of thermogravimetric analysis for both precursors. The NiFe-P sample shows the typical two-step decomposition of the reevesite precursor associated with the elimination of physically bounded water (180-200°C) and the dehydroxylation and decarbonation step (~280°C). In contrast, the Ni_{0.5}Fe-P sample displays the removal of interlayer water at the same temperature interval, while the second step is not clearly discerned and shifted to lower temperature. Probably, the presence of amorphous hydroxide (carbonate) phases in this sample was responsible for the different decomposition profile. In fact, as concluded from XRD, α -Fe₂O₃ could be detected over Ni_{0.5}Fe-C; therefore it is likely that part of iron may exist as FeO(OH) in the reevesite precursor, thus leading to the sequence $2\text{FeO}(\text{OH}) \rightarrow \gamma\text{-Fe}_2\text{O}_3 \rightarrow \alpha\text{-Fe}_2\text{O}_3$ upon calcination [23]. These results were also substantiated by DSC analysis. The total weight losses amounted to 30 and 24% for the NiFe-P and Ni_{0.5}Fe-P, respectively, which were significantly lower than the theoretical weight losses based upon their chemical formulae (37.8 and 42 % for NiFe and Ni_{0.5}Fe pure samples, respectively.) The lower total weight loss obtained likely refers to the presence of additional phases formed during the synthesis of precursors, and the incomplete synthesis of the hydrotalcite samples with the expected Ni/Fe ratio.

The TEM micrographs in Figure 3.3 reveal huge differences in morphology of the calcined samples. NiFe-C consisted of aggregations of uniform nanoparticles, which did not exceed 8-10 nm in diameter, combined with some platelet-like particles, while the Ni_{0.5}Fe-C sample was composed by rounded particles with an average diameter of 10-45 nm. The formation of larger spinel particles in Ni_{0.5}Fe-C was in agreement with the much lower surface area of this sample (42 m² g⁻¹) with respect to the NiFe-C sample (183 m² g⁻¹). From these results, it can be anticipated that differences in catalytic activity could be expected, as the dispersion of metallic nickel particles will be lower over the low-surface area catalyst.

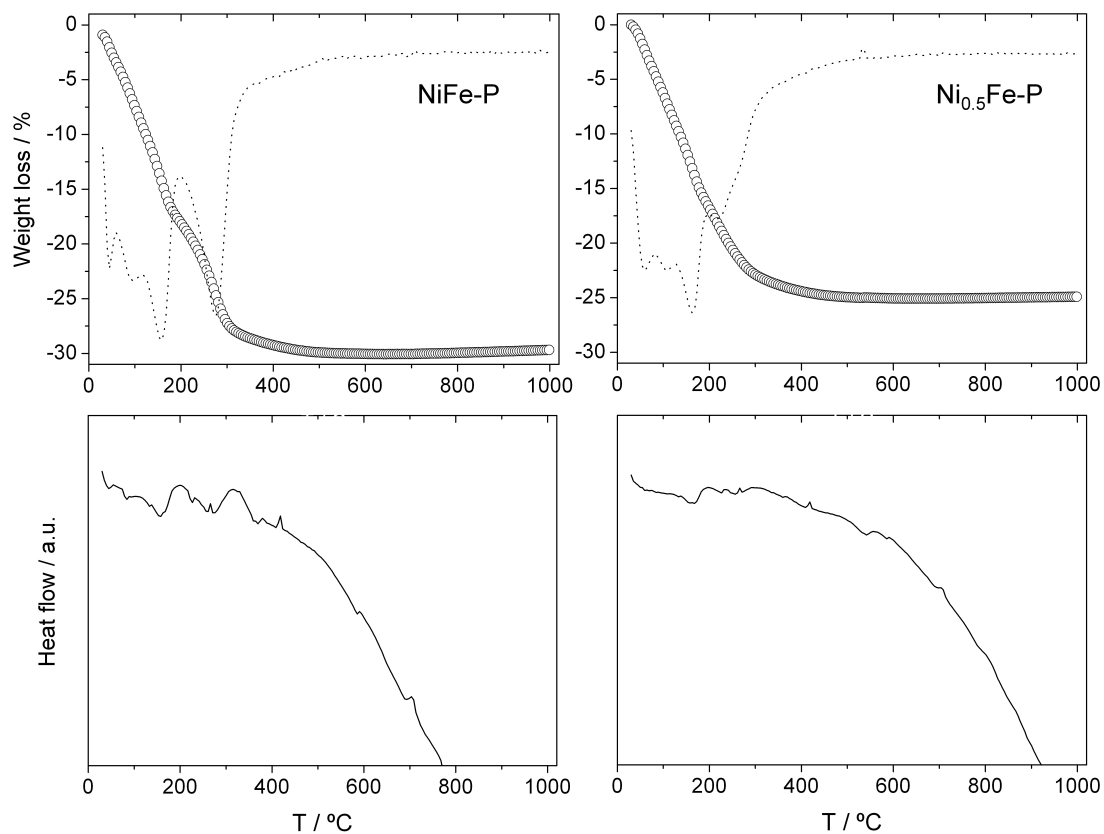


Figure 3.2. Thermogravimetric and calorimetric profiles of the as-synthesized reevesite samples with Ni/Fe ratios 1:1 and 0.5:1 in air and derivative of the weight loss.

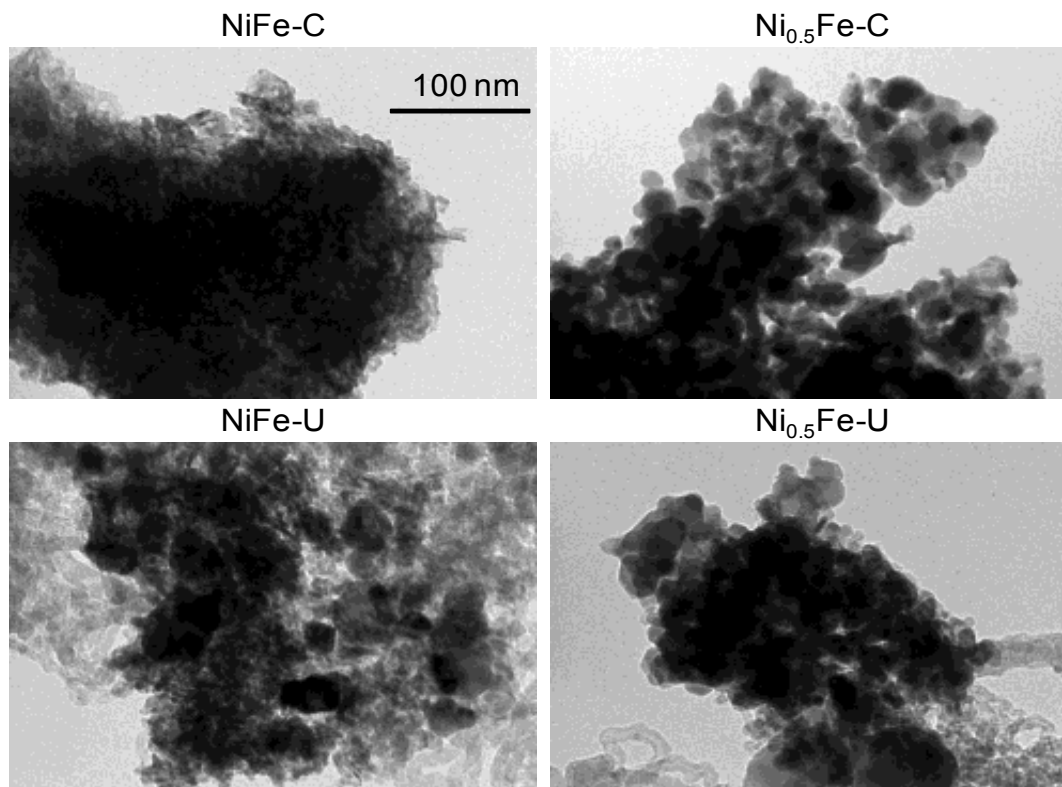


Figure 3.3. Transmission electron micrographs of calcined and reacted samples with Ni/Fe ratios 1:1 and 0.5:1. The scale bar applies to all micrographs.

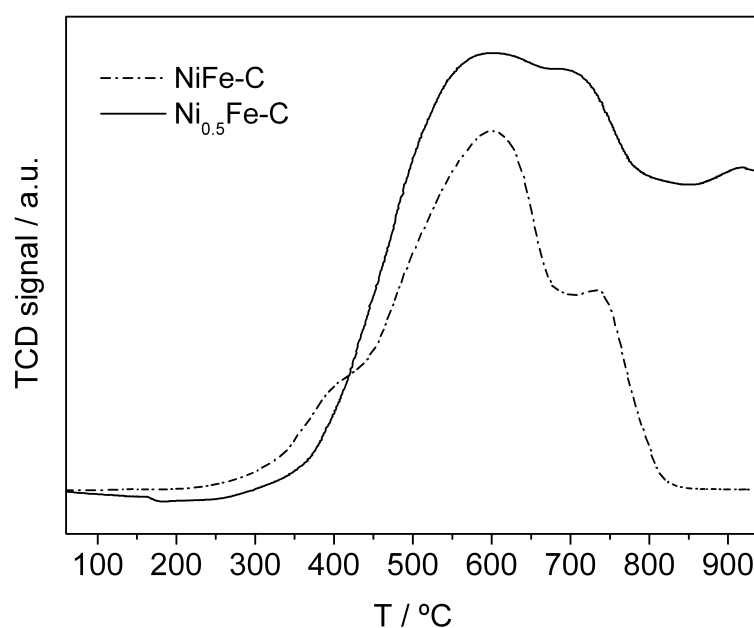


Figure 3.4. H₂-TPR profiles of the NiFe-C and Ni_{0.5}Fe-C samples.

Temperature programmed reduction profiles of the calcined samples are shown in Figure 3.4. Similarly to our previous work [20], the reduction occurred in the wide temperature range of ca. 300-1000°C. The peaks of hydrogen consumption displayed a slightly different profile depending on the Ni/Fe molar ratio.

Also, the whole signal for the Ni_{0.5}Fe-C sample was shifted to higher temperature, indicating that this particular sample was less reducible. The NiFe-C sample exhibited a complex reduction pattern with peaks centered at 600 and 730°C, and a small shoulder at around 395°C. This shoulder may be assigned to the reduction of pure NiO, which typically displays a single peak located at 340-400°C [24-25]. The reduction of nickel in the mixture Ni(Fe)O_x + NiFe₂O₄ was hindered by the presence of iron, which caused a shift to higher reduction temperature with respect to pure NiO. The reduction of Fe₂O₃ also occurred over almost the same temperature range. For example, the reduction of iron oxides may proceed in various steps, in the order Fe₂O₃→Fe₃O₄→FeO→Fe⁰, in the temperature range 300-730°C [26]. Other authors have observed that the reduction of Fe³⁺ to Fe²⁺ displays a sharp peak at

ca. 430°C, while a continuous broad peak corresponds to reduction of Fe^{2+} to Fe^0 , which is even not complete at 1000°C [27]. According to the literature, the peak at 600°C in the NiFe-C sample could be attributed to reduction of Fe^{3+} reduction into Fe_3O_4 , together with reduction of Ni(Fe)Ox species. The high-temperature peak at 730°C, which is likely assigned to NiFe_2O_4 reduction, grown and shifted to higher temperature (ca. 900°C) with the increase in iron content. This is in agreement with the higher percentage of spinel in the $\text{Ni}_{0.5}\text{Fe-C}$ sample (ca. 94%, Table 3.1). Besides, a high-intensity peak centered at 684°C was also present in the $\text{Ni}_{0.5}\text{Fe-C}$ sample, which may also account for the reduction of Fe_2O_3 species. This is supported by the work of Lin et al. [28], who observed the reduction of iron oxide within the temperature range 650-850°C. The fact that the reduction of Fe_2O_3 and NiO usually take place over the same temperature range (300-700°C), limits the precise identification of the individual reduction peaks of Fe and Ni in the catalysts.

3.3.2 Activity tests

3.3.2.1 Effect of the nickel to iron molar ratio

Ethanol conversion and product selectivity are shown in Figure 3.5 for NiFe-C and $\text{Ni}_{0.5}\text{Fe-C}$ catalysts during 24 hours reaction tests at 500°C. Both materials presented differences in conversion and selectivity. The NiFe-C catalyst maintained complete conversion for less than 3 h and then started to deactivate gradually, until it reached a steady conversion of around 65% after 15 h. Significant changes in product selectivity could be observed during the first time period: hydrogen and carbon dioxide selectivities grew from 40% and 30% at the beginning of the experiment till 65% and 40%, respectively. Simultaneously, selectivity to acetaldehyde decreased from 70% to 15%, while methane and carbon monoxide grew to 10% for CH_4 and to 35% for CO. Ethylene was only detected during the first hour of the reaction and it drop from 20% to 0%. This indicates that dehydrogenation and dehydration were the main ethanol conversion pathways on the surface

of the fresh catalyst, but selectivity shifted gradually and after only 1 h, acetaldehyde was subsequently converted through decarbonylation and steam reforming. As previously reported [20], this behavior suggests that metallic nickel particles were formed slowly over this catalyst in parallel to the growing of NiFe₂O₄ crystals, thus activating the decarbonylation reaction, and therefore leading to decreased acetaldehyde and increased methane selectivity. The initial ethylene selectivity was attributed to the presence of active Lewis acid sites (Ni²⁺ and Fe³⁺), which are responsible for dehydration. After 4 h of time on stream selectivity tended to stabilize, and after 20 h it was 60% for hydrogen, 35% for acetaldehyde, 45% for CO₂, 15% for CO, and less than 5% for methane. As concluded from previous work, the small metallic nickel particles formed slowly upon reaction, together with the high surface area of the fresh catalyst and the promotion effect by Fe/Fe²⁺ species induced a high activity for ethanol dehydrogenation, acetaldehyde decarbonylation and reforming [20].

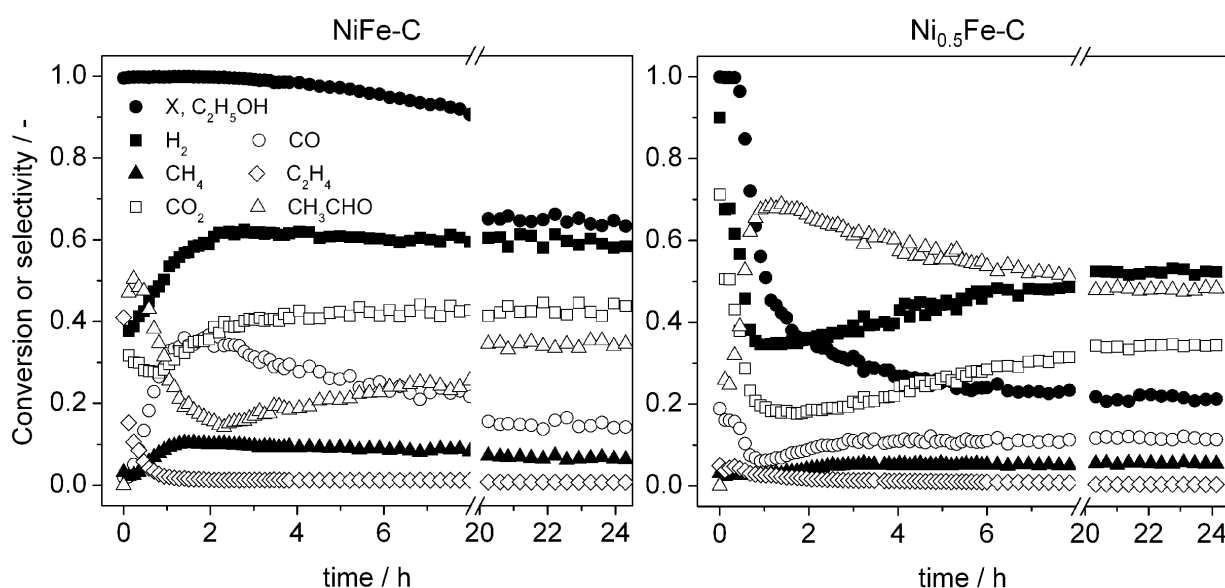


Figure 3.5. Ethanol conversion and selectivity to the different products vs time during ethanol steam reforming over calcined samples with Ni/Fe ratios 1:1 and 0.5:1. Conditions: H₂O/C₂H₅OH ratio = 6, T = 500°C, WHSV = 147.45 mol ethanol h⁻¹ kg_{cat}⁻¹, and P = 1 bar.

In contrast to the above behavior over NiFe-C, complete conversion was only observed for less than 30 min over Ni_{0.5}Fe-C, decreased to around 25% after 6 h, and

stabilized at around 20% after 10 h of catalyst time on stream. During the rapid deactivation period (first hour) hydrogen and carbon dioxide selectivity dropped sharply from 90% and 70% till 35% and 20% respectively, whereas acetaldehyde selectivity grew from 0 to 65%. Carbon monoxide selectivity decreased from 20% to 6%, methane only reached 2-3%, and ethylene dropped from 5% to 2%. This behavior is coherent with ethanol steam reforming being the main reaction on the fresh catalyst, although it rapidly shifted towards dehydrogenation to acetaldehyde. Beyond 1 h of time on stream, selectivity towards acetaldehyde decreased continuously while that of hydrogen, carbon dioxide and carbon monoxide increased again, pointing to an increase in the capacity of the catalyst to steam reform acetaldehyde.

After 10 h of operation conversion and selectivity stabilized, the latter reaching values of 52%, 35%, 10%, 5% and 48% for hydrogen, carbon dioxide, methane, carbon monoxide and acetaldehyde, respectively. No ethylene was detected on the gas products after 4 h of catalyst time on stream. These results suggest some differences with respect to the previous catalyst, being motivated by the less reducible character of the $\text{Ni}_{0.5}\text{Fe-C}$ catalyst. That is, the higher amount of iron in this sample led to a higher percentage of spinel upon calcination, while upon in situ reduction less amount of metallic nickel was formed (15% in $\text{Ni}_{0.5}\text{Fe-U}$ vs 42% in NiFe-U , Table 3.1). The spinel phase exhibits a lower propensity to be reduced under reaction conditions, and therefore, less Ni^0 particles were present on the catalyst surface. Larger metallic nickel particles were present in $\text{Ni}_{0.5}\text{Fe-U}$, which in turn displayed a lower surface area. The induction period over this catalyst was relatively long, as concluded by its less reducible character, and therefore, acetaldehyde steam reforming was more effective with extended time on stream, thus increasing hydrogen selectivity. On the other hand, ethanol conversion dropped suddenly, probably due to fast carbon deposition. In view of the strong activity decay observed in the beginning of the reaction, it is likely that a certain amount of acid Lewis sites (Ni^{2+} and Fe^{3+}) were present in this catalyst, which induced ethanol

dehydration to a lower extent than in the NiFe-C catalyst, but further promoted polymerization into coke. This was confirmed by the absence of ethylene, and through characterization of used catalysts (see below). Besides, deactivation by Ni⁰ sintering can also be considered. Similar observations in terms of carbon deposition were found by Muroyama et al. [21] when using a NiFe₂O₄ catalyst. They attributed the decreased ethanol conversion to coke formation through the dehydration pathway.

In order to assess the above observations, both catalysts were further characterized after reaction. Considering that no reduction pretreatment was performed over the calcined catalysts before reaction, nickel species in both catalysts were progressively reduced under reaction conditions. This was confirmed by the XRD pattern of the used samples, shown in Figure 3.6 for those tested during 24 h at 500°C.

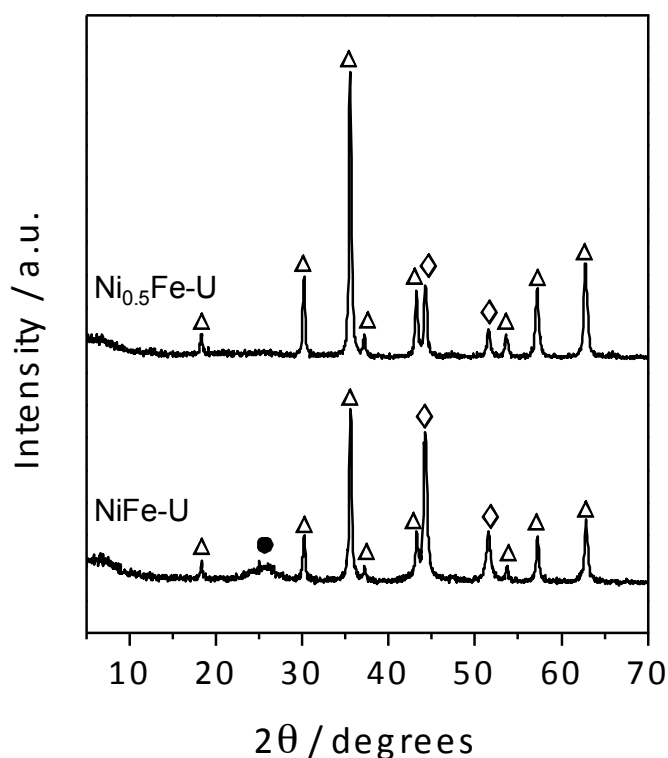


Figure 3.6. XRD patterns of NiFe and Ni_{0.5}Fe samples after reaction. Crystalline phases: (△) NiFe₂O₄, (●) carbon depositions, (◇) metallic Ni.

After the test, Ni(Fe)Ox reflections in the NiFe-U sample disappeared and the two reflections at 2θ 44° and 52° associated with Ni^0 appeared (powder diffraction file 4-850 from ICDD). The average crystallite size of metallic nickel in this sample reached 13.9 nm (Table 3.2). Diffraction lines related to NiFe_2O_4 were also present. Based on the percentage of phases (Table 3.1), a slight variation between ca. 58% and 62% of NiFe_2O_4 manifested in NiFe-U and NiFe-C, respectively. However, the intensity of the diffraction lines greatly increased from NiFe-C (diffraction lines are coincident in 2θ with those of NiO) to NiFe-U. This was consequence of NiFe_2O_4 particle growing, as confirmed by the increase in average crystallite size from ca. 2 nm to 23 nm after reaction (Table 3.2). As expected from the metal ratio in the samples, the intensity of the NiFe_2O_4 reflections increased with the increase in Fe content, that is, in the $\text{Ni}_{0.5}\text{Fe-U}$ sample. This was not only related to the larger NiFe_2O_4 average crystallite size (from ca. 10 in $\text{Ni}_{0.5}\text{Fe-C}$ to 23 nm in $\text{Ni}_{0.5}\text{Fe-U}$), but also to the higher percentage of this phase in the sample (ca. 84.7%) compared to the NiFe-U sample. Particularly, the percentage of metallic nickel in the $\text{Ni}_{0.5}\text{Fe-U}$ sample was around three times lower than in NiFe-U, which suggested the less reducible character of samples with higher iron content [20]. This was also confirmed by TPR (Figure 3.4) showing a broad reduction profile in the $\text{Ni}_{0.5}\text{Fe-C}$ sample extended to a temperature above 1000°C . The fact that the average crystallite size of metallic nickel in this sample was higher than in NiFe-U could be related to a higher tendency of nickel to sinter in the NiFe_2O_4 matrix. No other metallic or oxidized iron species were detected in any of the samples. It is important to notice that only the NiFe-U sample exhibited a diffraction peak at 2θ 26° , assigned to the formation of deposited carbon upon reaction (powder diffraction file 41-1487). This is in agreement with the formation of carbon deposits over this catalyst, which are likely responsible for deactivation.

Table 3.2: Average crystallite size of the different catalysts.

Sample	Crystallite size / nm			
	NiO	NiFe ₂ O ₄	Ni	Fe ₂ O ₃
NiFe-C	3.5	1.99	-	-
Ni _{0.5} Fe-C	-	9.9	-	26
Ni _{0.5} Fe-U	-	23.7	20.3	-
NiFe-U, T = 400°C	-	23.7	2.8	-
NiFe-U, T = 500°C	-	23.1	13.9	-
NiFe-U, T = 600°C	-	13.6	23.0	-

TEM analyses were performed to check differences in particle morphology and the eventual formation of carbon deposits (Figure 3.3). These deposits can be divided by their morphology in two groups: “foam”-shaped carbon and “worms” or nanotubes [29-31]. Both of them were present in our samples. Particle sintering was also observed in both samples.

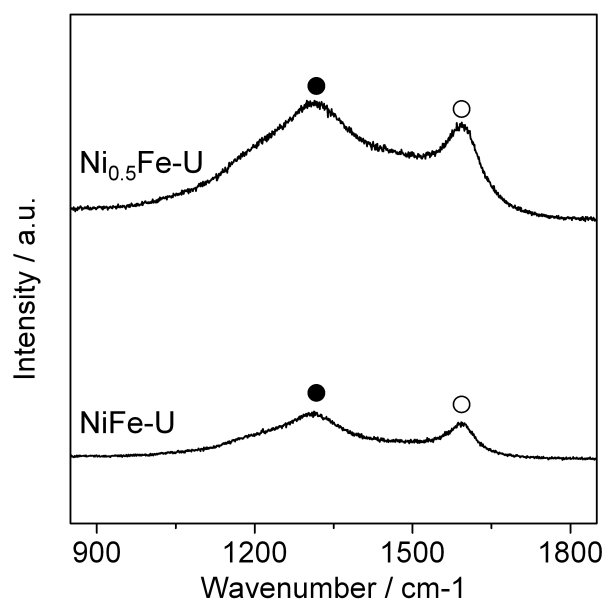


Figure 3.7. Raman spectra of NiFe and Ni_{0.5}Fe samples after reaction. Phases: (△) NiFe₂O₄, (●) disordered carbon, (○) graphitized carbon, (■) NiO.

Raman spectra define the nature of the carbon deposited on the catalyst surface (Figure 3.7). Two broad bands in the range 1000-1700 cm⁻¹ can be observed in both samples. The band at 1310 cm⁻¹ is associated with the vibrations of disordered structures like amorphous carbon, carbon nanoparticles or filamentous carbon (D-band), and the band at

1590 cm^{-1} (G-band) is responsible for graphite formation [32]. Since the intensity of the former band was higher than the latter, disordered carbon species predominated in both catalysts.

The degree of graphitization of the carbon deposited ($R = I_D/I_G$), as determined by the integrated intensity ratio of these two bands, was very similar in both cases, which implies the same carbon formation mechanism. However, the amount of deposited carbon was higher in the $\text{Ni}_{0.5}\text{Fe-U}$ sample, as compared to the NiFe-U sample. This could be the reason for the fast deactivation of the $\text{Ni}_{0.5}\text{Fe-C}$ catalyst, which is in agreement with the activity decay observed by Muroyama et al. [21] for a NiFe_2O_4 -based catalyst, and attributed to the high tendency of the spinel for coke formation.

In summary, the differences in (i) Ni^0 crystallite size (Table 3.2), (ii) its dispersion over a matrix with important differences in specific surface area ($183 \text{ m}^2 \text{ g}^{-1}$ in NiFe-C vs $42 \text{ m}^2 \text{ g}^{-1}$ in $\text{Ni}_{0.5}\text{Fe-C}$), (iii) the different percentage of crystalline phases (Table 3.1), and (iv) the amount of coke formed over the spinel, are responsible for the variation in catalytic activity. Therefore, as previously concluded, the best performing catalyst consists of a mixture of Ni(Fe)O_x solid solution and NiFe_2O_4 with very small crystallites, which will be further investigated in detail at different reaction temperatures.

3.3.2.2 Effect of the reaction temperature

Catalyst NiFe-C was further studied to assess the influence of temperature on its selectivity towards ethanol steam reforming products. This material was selected because of better performance than other catalysts containing different nickel-to-iron ratios (0.5, 2 and 3) [20]. Figure 3.8 shows the evolution of conversion and selectivity with catalyst time-on-stream at three selected temperatures. At 400°C the catalyst showed a low activity period of about 2 h in which conversion was only 23 to 25%. Ethanol dehydrogenation was the dominant reaction giving a selectivity to acetaldehyde of 80 to 98%. Selectivity to CO_2 was only around 5%, and

carbon monoxide and methane were not detected. Ethanol dehydration to ethylene was also significant in the first minutes of reaction, but ethylene selectivity decreased steadily from 15% to 0% within 2 hours. After this time, ethanol conversion and selectivity towards hydrogen, carbon oxides and methane grew sharply, while acetaldehyde selectivity fell to a minimum of 5% at 4 h of time on stream. The initial behavior of the catalyst is explained by the capacity of nickel oxides (Ni^{2+} species) to catalyze ethanol dehydrogenation (see below). However, the hydrogen released during the first 2 h of experiment prompted the reduction of Ni^{2+} to Ni^0 . Once enough nickel was reduced, it catalyzed the reforming and acetaldehyde decarbonylation reactions thus producing the shift in conversion and selectivity.

This behavior indicates the slow conditioning of the catalyst. After 5 hours, ethanol conversion started to fall till it stabilized around 70% after 20 h of time on stream. Simultaneously, acetaldehyde grew from 5% to 30%. Methane and carbon monoxide also decreased suggesting that the activity towards decarbonylation was dropping. Since methane selectivity was higher than that of CO, and carbon dioxide and hydrogen reach a stable value, we may conclude that steam reforming of acetaldehyde and ethanol were taking place.

The catalyst was also tested at 600°C for 24 hours (Figure 3.8). At this higher temperature in-situ reduction of the catalyst was much faster. Complete conversion of ethanol and the presence of reforming products such as carbon oxides, methane and hydrogen, were observed from the beginning of the experiment, while acetaldehyde was not detected during the first hour. However, ethanol dehydration to ethylene was also significant at the beginning (15% selectivity), and a local maximum was also observed at around 4 hours of time on stream (3%).

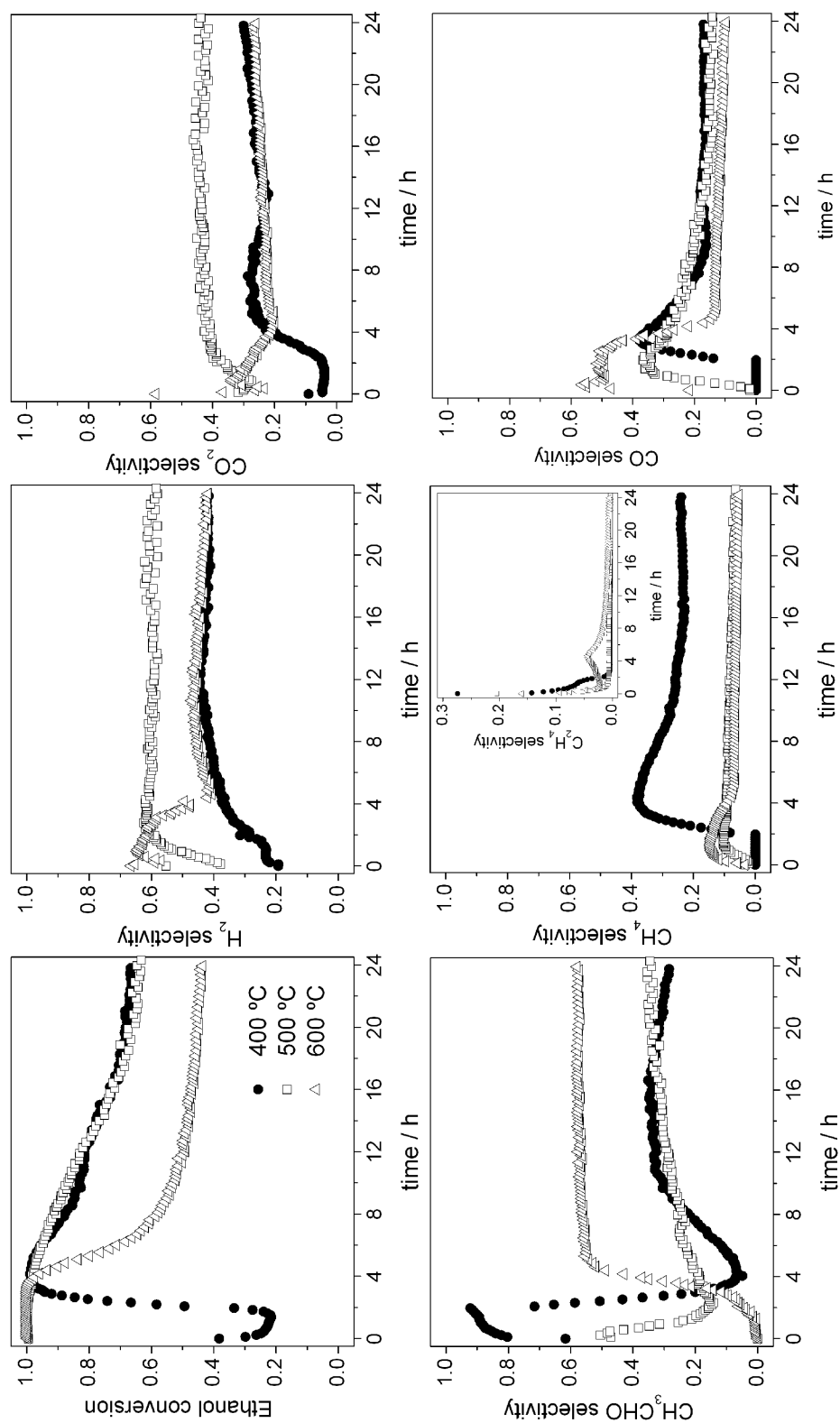


Figure 3.8. Ethanol conversion and selectivity to the different products vs time during ethanol steam reforming over NiFe-C at different temperatures. Conditions: $\text{H}_2\text{O}/\text{C}_2\text{H}_5\text{OH}$ ratio = 6, WHSV = $147.45 \text{ mol ethanol h}^{-1} \text{ kg}_{\text{cat}}^{-1}$, and $P = 1 \text{ bar}$. Inset in CH_4 graph: C_2H_4 selectivity.

These facts indicate that the reaction initially proceeded through ethanol dehydrogenation coupled with steam reforming of acetaldehyde, acetaldehyde decarbonylation, methanation, and ethanol dehydration. After two hours, however, acetaldehyde selectivity grew sharply which indicates that acetaldehyde steam reforming was hindered at longer reaction time and high reaction temperature. This also explained the decrease in H₂ and CO. After 20 h of time on stream ethanol conversion stabilized at around 45%, with acetaldehyde (56% selectivity), hydrogen (43%), carbon dioxide (25%) and monoxide (11%), and methane (8%) as main products. Ethylene was no longer detected at this point.

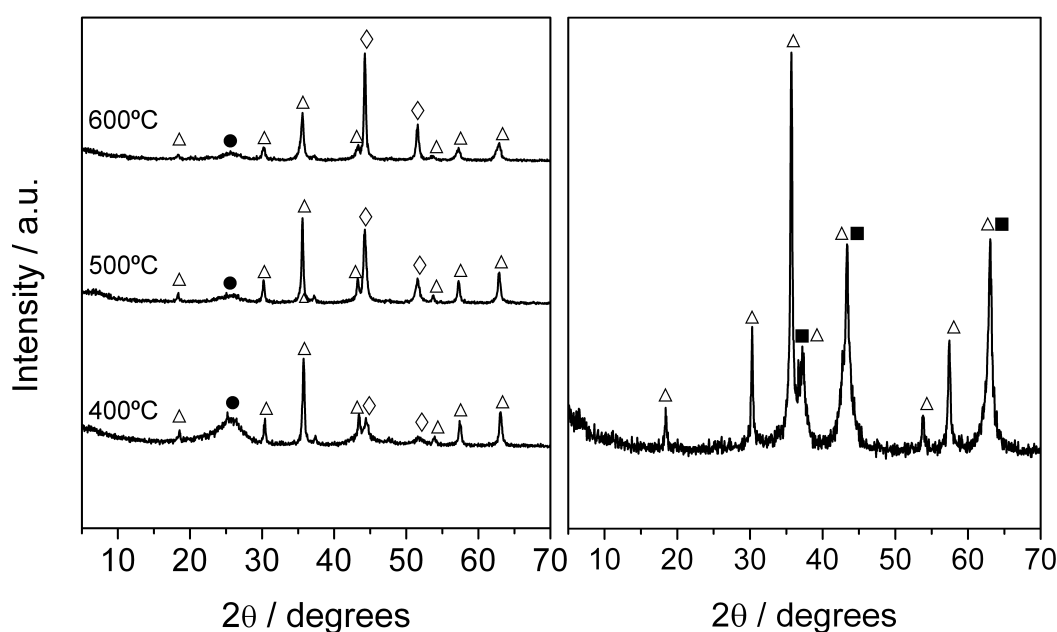


Figure 3.9. XRD patterns of the NiFe-C sample after reaction for 24 h at different temperatures ($T=400^{\circ}\text{C}$, $T=500^{\circ}\text{C}$ and $T=600^{\circ}\text{C}$, left) and after reaction for 3 h at 400°C (right). Crystalline phases: (■) NiO, (Δ) NiFe₂O₄, (●) carbon, (\diamond) Ni metallic.

Catalysts used after reaction at the three temperatures were characterized by XRD and TEM. The XRD patterns of the NiFe-C catalyst after reaction tests at the three temperatures are shown in Figure 3.9, left. It reveals the reflections assigned to NiFe₂O₄ and the two reflections at 2θ 44° and 52° associated with metallic nickel. Increasing the reaction

temperature slightly incremented the percentage of metallic nickel from 40 to 46% (Table 3.1), but also resulted in the increase of the Ni⁰ average crystallite size from 2.8 nm at 400°C to 23.0 nm at 600°C (Table 3.2). This was due to sintering of metallic nickel particles under more severe reaction conditions, which finally led to decreased ethanol conversion and hampered acetaldehyde reforming. The fact that the percentage of NiFe₂O₄ remained practically invariable at these three temperatures stresses the low reducibility of the spinel phase, thus requiring temperatures above 600°C for reduction (Figure 3.4).

By comparison of the crystalline phases present at 400°C with the catalytic performance at the same temperature (Figure 3.8), we can conclude that before 3 h of reaction, the ethanol conversion was only around 25% and the acetaldehyde selectivity reached 85%. As previously mentioned, during this period the active sites should be related to Ni²⁺ species, which were slowly reduced *in situ* into Ni⁰, thus activating acetaldehyde decarbonylation and reforming reactions. This was confirmed by the XRD pattern of the catalyst after a 3 h reaction test (Figure 3.9, right), showing the diffraction lines related to the mixture NiFe₂O₄+NiO, and the absence of Ni⁰ diffraction lines. The reflection at 2θ 26° attributed to coke with graphite-like structure appeared in all cases. Considering that the intensity of the carbon diffraction line is proportional to the coke amount, less carbon deposits were formed upon increasing reaction temperature. TEM micrographs in Figure 3.10 showed carbon nanofibers over all catalysts, but especially in the catalyst after reaction at 400°C. These results are in agreement with XRD observations.

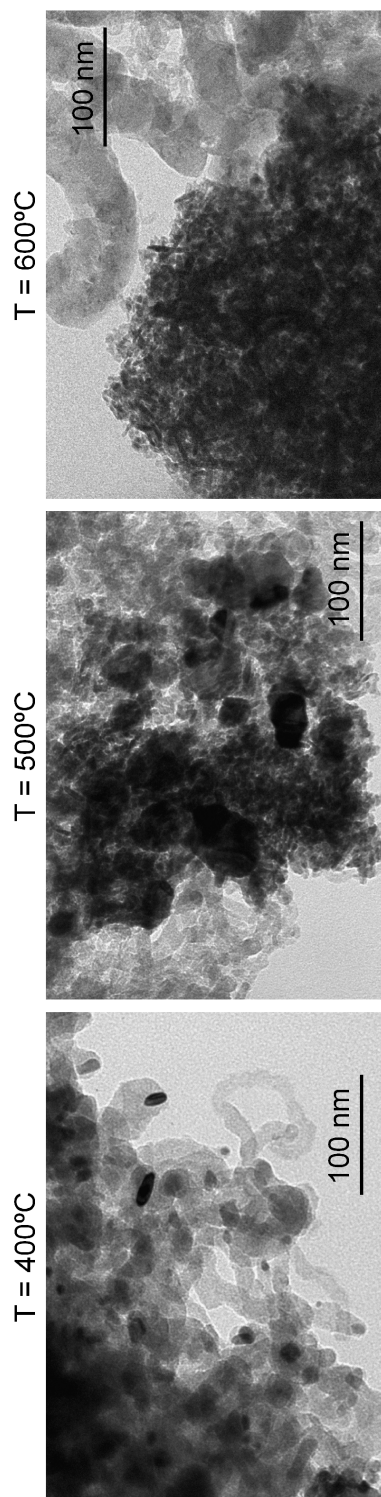


Figure 3.10. Transmission electron micrographs of the NiFe-U sample after reaction at different temperatures. The scale bar applies to all micrographs.

3.4. Conclusions

Activation treatments at low calcination temperature together with increasing amount of iron play an important role to enhance the catalytic activity and hydrogen selectivity of nickel-based spinel catalysts in ethanol reforming. This is due to the improved nickel dispersion and reduced carbon deposition, motivated by the presence of iron, and the high surface area and small Ni⁰ crystallite size over the Ni(Fe)O_x + NiFe₂O₄ mixtures. However, an excess of iron in the sample precursor, i.e. Ni/Fe ratios of 0.5, induces the formation of a low surface area spinel phase (NiFe₂O₄), even at low calcination temperature. This results in lower activity and faster deactivation in the reaction. The variations in Ni⁰ crystallite size and dispersion, and the difference in surface area prompted by the different percentage of crystalline phases (Ni(Fe)O_x and NiFe₂O₄) are therefore decisive for improved catalytic performance.

Increasing the reaction temperature from 400°C to 600°C over the best catalyst (Ni/Fe =1) generated less carbon deposits and favored ethanol dehydrogenation combined with steam reforming of acetaldehyde, acetaldehyde decarbonylation, methanation, and ethanol dehydration. However, partial deactivation is present at longer time on stream due to nickel sintering. The optimum temperature for higher ethanol dehydrogenation and acetaldehyde reforming, coupled with lower methane production was 500°C. Under these conditions, the best catalyst reached a stable hydrogen selectivity of up to 60%.

3.5. References

- [1] T. Abbasi, S.A. Abbasi, *Renew. Sustain. Energy Rev.* 15 (2011) 3034–3040.
- [2] D.B. Levin, R. Chahine, *Int. J. Hydrogen Energy* 35 (2010) 4962-4969.
- [3] M. Ni, D.Y.C Leung, M.K.H. Leung, *Int. J. Hydrogen Energy* 32 (2007) 3238-3247.
- [4] L.F. Brown, *Int. J. Hydrogen Energy* 26 (2001) 381-397.
- [5] J. Xuan, M.K.H. Leung, D.Y.C. Leung, M. Ni, *Renew. Sustain. Energy Rev.* 13 (2009) 1301-1313.
- [6] A. Haryanto, S. Fernando, N. Murali, S. Adhikari, *Energy Fuels* 19 (2005) 2098-2106.
- [7] M. Toth, M. Domok, J. Raskox, A. Hancz, A. Erdohelyi, *Chem. Eng. Trans.* 4 (2004) 229-234.
- [8] F. Haga, T. Nakajima, H. Miya, S. Mishima, *Catal. Lett.* 48 (1997) 223-227.
- [9] J. Llorca, N. Homs, J. Sales, P. Ramírez de la Piscina, *J. Catal.* 209 (2002) 306-317.
- [10] J. Llorca, N. Homs, J. Sales, J.L.G. Fierro, P. Ramírez de la Piscina, *J. Catal.* 222 (2004) 470-480.
- [11] J.A. Torres, J. Llorca, A. Casanovas, M. Domínguez, J. Salvadó, D. Montané, *J. Power Sources* 169 (2007) 158-166.
- [12] F. Frusteri, S. Freni, V. Chiodo, L. Spadaro, O. Di Blasi, G. Bonura, S. Cavallaro, *Appl. Catal. A* 270 (2004) 1-7.
- [13] W.T. Zhu, J. Sun, X.P. Qiu, F.Wu, *Int. J. Hydrogen Energy* 30 (2005) 437-445.
- [14] J. Comas, F. Mariño, M. Laborde, N. Amadeo, *Chem. Eng. J.* 98 (2004) 61-68.
- [15] Y. Yang, J. Ma, F. Wu, *Int. J. Hydrogen Energy* 31 (2006) 877-882.
- [16] M.N. Barroso, M.F. Gomez, L.A. Arrua, M.C. Abello, *Appl. Catal. A* 304 (2006) 116-123.
- [17] F. Trifirò, A. Vaccari. Hydrotalcite-like anionic clays (layered double hydroxides). In: Alberti G, Bein, editors. *Comprehensive Supramolecular Chemistry*, Oxford: Elsevier; 1996, p.251-291.
- [18] F. Cavani, F. Trifirò, A. Vaccari, *Catal. Today* 11 (1991) 173-301.
- [19] S. Kannan, *Catal. Surv. Asia* 10 (2006) 117-137.
- [20] S. Abelló, E. Bolshak, D. Montané, *Appl. Catal. A* 450 (2013) 261-274
- [21] H. Muroyama, R. Nakase, T. Matsui, K. Eguchi, *Int. J. Hydrogen Energy* 35 (2010) 1575-1581.
- [22] M. Tu, J. Shen, Y. Chen, *Thermochim. Acta.* 302 (1997) 117-124.
- [23] V. Balek, J. Subrt, *Pure Appl. Chem.* 67 (1995) 1839-1842.
- [24] M. Li, X. Wang, S. Li, S. Wang, X. Ma, *Int. J. Hydrogen Energy* 35 (2010) 6699-6708.
- [25] K.V.R. Chary, P.V.R. Rao, V. Vishwanathan, *Catal. Commun.* 7 (2006) 974-978.
- [26] M.S. Lee, J.Y. Lee, D.W. Lee, D.J. Moon, K.Y. Lee, *Int. J. Hydrogen Energy* 37 (2012) 11218-11226.

- [27] Z. Yu, D. Chen, M. Rønning, T. Vrålstad, E. Ochoa-Fernández, A. Holmen, *Appl. Catal. A* 338 (2008) 136-146.
- [28] H.Y. Lin, Y.W. Chena, C. Li, *Thermochim. Acta.* 400 (2003) 61-67.
- [29] G. Zeng, Q. Liu, R. Gu, L. Zhang, Y. Li, *Catal. Today* 178 (2011) 206-213.
- [30] F. Wang, Y. Li, W. Cai, E. Zhan, X. Mu, W. Shen, *Catal. Today* 146 (2009) 31-36.
- [31] S.M. de Lima, A.M. da Silva, L.O.O. da Costa, U.M. Graham, G. Jacobs, B.H. Davis, L.V. Mattos, F.B. Noronha, *J. Catal.* 268 (2009) 268-281.
- [32] A.E. Galetti, M.F. Gomez, L.A. Arrúa, M.C. Abello, *Appl. Catal.* 348 (2008) 94-102.

Chapter 4

Ternary Ni-Al-Fe catalysts for ethanol steam reforming

Ternary mixed oxides prepared from takovite/reevesite $\text{Ni}_3\text{Al}_{1-x}\text{Fe}_x$ precursors were tested in ethanol steam reforming for hydrogen production. The influence of the trivalent cation (Al^{3+} or Fe^{3+}) on phase composition and derived catalytic performance of the resulting oxides was studied. The physico-chemical properties of the hydrotalcite-like precursors and related oxides were characterized by ICP, XRD, TGA-DSC, Raman, H_2 -TPR, and TEM analyses. Compared to pure binary systems (Ni_3Al and Ni_3Fe), the ternary systems showed the best performance in ethanol reforming, leading to a high and stable hydrogen selectivity of up to ca. 70% in 100 h-reaction tests. The increase in activity can be attributed to a cooperative effect between aluminum and iron, favoring ethanol dehydrogenation as the primary step, followed by acetaldehyde reforming and/or cracking, reverse water gas shift, and methanation, and concomitantly limiting the dehydration route to ethylene.

-
This chapter is based on the following publication:

S. Abelló, E. Bolshak, F. Gispert-Guirado, X. Farriol and D. Montané. Ternary Ni–Al–Fe catalysts for ethanol steam reforming. *Catal. Sci. Technol.*, 2014, 4, 1111

4.1. Introduction

Catalytic steam reforming is a key process to obtain hydrogen from renewable liquid biofuels such as ethanol, the focus being on the cost-effective synthesis of hydrogen in fuel-processors coupled to low-temperature fuel cells for high-efficiency power production in stationary and transportation applications [1-3]. Steam reforming of ethanol on metal-based heterogeneous catalysts involves a complex set of reactions, which in summary comprise ethanol dehydration into ethylene, ethanol dehydrogenation to acetaldehyde, cracking of ethanol and acetaldehyde, reforming of C₂ species into hydrogen and carbon oxides, together with the methanation and water-gas shift equilibrium reactions [4]. Carbon deposition by ethylene polymerization and other mechanisms may also take place to a significant extent, depending on the nature of the catalyst, temperature and the steam to carbon ratio [4-6]. Many supported-metal catalysts have been investigated for ethanol steam reforming, the most active being those based on noble metals (Pt, Rh, Pd and Ru), followed by Ni- and Co-based [6-10]. So far, nickel-based catalysts had shown the best combination of effective cost and high activity to C-C and O-H scission and H₂ formation [5, 11]. Metallic nickel, however, shows susceptibility to sinter and to form carbonaceous deposits in contact with hydrocarbons, two negative trends that may lead to severe deactivation [12, 13]. A large variety of supports have been tested, the most common involving combinations of Al₂O₃, La₂O₃, MgO, CeO₂, and ZnO, with occasional doping with K, Mn, Fe or other metals to improve metal dispersion and stability, and decrease coke formation.

The *hydrotalcite route* (coprecipitation) has been adopted as an efficient way to attain highly dispersed multimetallic mixed oxides by combination of two or more metals [14, 15]. These oxides combine high surface area, high metal loading and dispersion, good thermal stability, and controllable acid/base/redox properties [16, 17]. This has been used to prepare hydrotalcite catalysts for ethanol steam reforming, usually having Ni as the main active phase, and other metals to achieve some kind of cooperative effects to enhance the hydrogen

selectivity and reduce coke formation [18-29]. Elementary catalytic systems like takovite, the Ni-Al hydrotalcite, have been explored in the reaction with boosted performance with respect to conventional Ni/Al₂O₃ prepared by impregnation [6, 30]. Despite the high dispersion of nickel crystallites upon calcination and reduction, the presence of an alumina matrix induces ethanol dehydration through its acid sites, leading to coke formation [6]. On the other hand, we recently explored the preparation of Ni-Fe catalysts from hydrotalcite precursors, and their performance for ethanol steam reforming [31, 32]. It was found that both the amount of iron and the selection of activation conditions exert a positive influence on the performance as they determine the size and dispersion of nickel species, and the nature of the oxide, respectively. With those two systems in mind, i.e. Ni-Al and Ni-Fe, it was interesting to analyze whether a ternary system Ni-Al-Fe would improve the performance of the separate binary oxides.

In this paper, trimetallic Ni₃Al_{1-x}Fe_x catalysts have been prepared by coprecipitation and subsequent calcination to the corresponding oxides, and the effect of chemical composition on their performance in ethanol steam reforming investigated.

4.2. Experimental

4.2.1. Catalyst preparation.

Nickel-aluminum-iron hydrotalcite precursors Ni₃Al_{1-x}Fe_x (x = 0-1) were synthesized by coprecipitation at constant pH. Aqueous solutions of the metal nitrates (1M of Ni(NO₃)₂·6H₂O, 1M of Al(NO₃)₃·9H₂O and 1M of Fe(NO₃)₃·9H₂O) and the precipitating agent (NaOH/Na₂CO₃, 1M of each) were simultaneously fed into a vessel by a 905 Titrand® automated titrator (Metrohm AG) equipped with two 800 Dosino® dosing systems. The pH was kept at a constant value of 10 (±0.2). The resulting slurries were aged at 303 K overnight under vigorous stirring. The precipitates were filtered and washed with deionized water and

then dried at 353 K during 12 hours. The samples were calcined in static air at 723 K for 6 h using a heating rate of 5 K min⁻¹.

4.2.2. Catalyst characterization

The chemical composition of the solids was determined by inductively coupled plasma-optical emission spectroscopy (ICP-OES) in a Spectro Arcos 165 spectrophotometer. Before analysis, the solids were dissolved in 1% HNO₃ aqueous solution. XRD measurements were made using a Siemens D5000 diffractometer (Bragg-Brentano parafocusing geometry and vertical goniometer) fitted with a curved graphite diffracted-beam monochromator, incident and diffracted -beam Soller slits, aperture/divergence slit angle 0.5, scattered-radiation slit angle 0.5, a 0.06 receiving slit and scintillation counter as a detector. The angular 2 θ diffraction range was between 5.0 and 70.0. The data were collected with an angular step of 0.05° at 3 s per step. Cu_k radiation was obtained from a copper X-ray tube operated at 40 kV and 30 mA. The quantitative phase content of the catalysts before reaction was determined by a multiphase Rietveld refinement [33] using TOPAS [34] software. The conventional quantitative phase analysis with the Rietveld method is carried out with the equation 1, [35] where S_{α} is the refinable Rietveld scale factor, Z is the number of formula units in unit cell, M is the molecular mass of formula unit, V is unit cell volume and W_{α} is the weight fraction for phase α . Equation 1 can only be used if the crystal structures of all phases are known. In the present case the analyzed samples exhibited a significant amount of non-crystalline carbon formed upon reaction. Therefore, the ZMV term for this phase is unknown and thus the conventional quantitative analysis cannot be performed. In such cases the quantitative method PONKCS (Partially or not known crystal structure) can be applied [36]. The method consists on adding a known quantity of a crystalline standard (W_s) to a pure sample of the phase problem or with a high content of this phase and then applying equation 2, where $(ZM)_{\alpha}$ have

no physical meaning but allows to estimate W_α in the sample problem and V_α is the unit cell volume (arbitrary or not).

$$W_\alpha = \frac{S_\alpha (ZMV)_\alpha}{\sum_{k=1}^n S_k (ZMV)_k} \quad (\text{eq. 4.1})$$

$$(ZM)_\alpha = \frac{W_\alpha S_\alpha (ZMV)_\alpha}{W_\alpha S_\alpha V_\alpha} \quad (\text{eq. 4.2})$$

In our case, we used Si (NIST SRM 640b) as internal standard. Due to the process itself of non-crystalline carbon formation upon reaction in the samples, it was impossible to obtain a pure sample of non-crystalline carbon. So, we used a sample with a high content of non-crystalline carbon as the spiked sample with Si for estimating $(ZM)_\alpha$. The crystallite size (more accurately, the volume weighted mean crystallite size) was also estimated with the software TOPAS (that works with the Double-Voigt Approach) by considering the instrumental contribution to the peak width (Fundamental Parameters Approach) [37] and fitting only the Lorentzian contribution to the crystallite size peak broadening, thus not considering microstrain peak broadening in the phases, and finally applying the Scherrer formula.

Transmission electron microscopy (TEM) was carried out in a JEOL JEM-1011 microscope operated at 100 kV. A few droplets of the sample suspended in ethanol were placed on a carbon-coated copper grid followed by evaporation at ambient conditions. N_2 adsorption data was measured on a Quantachrome Quadrasorb-SI gas-adsorption analyzer at 77 K. Prior to the measurements, the as-prepared and calcined (used) samples were degassed in vacuum at 393 K and 573 K for 10 h, respectively. Thermogravimetric analysis-differential scanning calorimetry (TGA-DSC) was measured in a Mettler Toledo TGA/DSC 1 microbalance. Analyses were performed in air ($20 \text{ cm}^3 \text{ STP min}^{-1}$) increasing the sample temperature from 298 to 1273 K at 5 K min^{-1} . Temperature-programmed reduction with hydrogen (H_2 -TPR) was measured in a ChemBet Pulsar TPR/TPD unit equipped with a thermal conductivity detector. Ca. 50 mg of calcined samples were loaded in the U-quartz

microreactor, pretreated in air ($20 \text{ cm}^3 \text{ STP min}^{-1}$) at 573 K for 1 h, and cooled to 50 K in the same atmosphere. The analysis was carried out in a mixture of 5 vol% H_2 in N_2 ($20 \text{ cm}^3 \text{ STP min}^{-1}$), ramping the temperature from 323 to 1173 K at 10 K min^{-1} . Raman spectra were recorded at room temperature using a Renishaw InVia Raman Spectrometer equipped with confocal DM 2500 Leica optical microscope, a CCD detector, and a diode laser operating at 785 nm. The applied power of the laser beam focusing on the sample was 3 mW. The spectra were measured in the $90\text{-}1000 \text{ cm}^{-1}$ range in single scan with 30 s of exposure time.

4.2.3. Catalytic tests

Ethanol steam reforming was carried out at atmospheric pressure in a fixed-bed stainless steel reactor (internal diameter of 10 mm), which has been described elsewhere [31]. The reactor was filled with 50 mg of catalyst particles sieved to 100-300 μm , diluted with 10 grams of SiO_2 particles of the same size. The reagent feed was an ethanol and water mixture with a molar ratio of 1:6 (a steam to carbon ratio, S/C, of 3:1). The feed rate was $0.2 \text{ cm}^3 \text{ min}^{-1}$, which corresponded to a weight hourly space velocity (WHSV) of $147.45 \text{ mol ethanol h}^{-1} \text{ kg}_{\text{cat}}^{-1}$. Each sample of catalyst was tested for 100 hours at constant conditions, and the spent catalyst was then collected for further characterization. The reaction temperature was varied from 773 to 873 K in selected experiments. Reaction products were quantified with an on-line gas chromatograph (Agilent 3000A microGC). A constant flow of N_2 ($500 \text{ Ncm}^3 \text{ min}^{-1}$) was added at the reactor outlet to dilute the products and avoid condensation of water in the microGC and sampling line, which was heat-traced at 393 K.

Ethanol conversion (X_{EtOH}), product selectivity (S_k) and carbon balance (CB) were calculated with equations 3 to 6, where F_j is the molar flow of product j , and nC_j is the number of carbon atoms in product j .

$$X_{\text{EtOH}} = \frac{F_{\text{EtOH},0} - F_{\text{EtOH}}}{F_{\text{EtOH},0}} \quad (\text{eq. 4.3})$$

$$S_j = \frac{nC_j \cdot F_j}{2(F_{EtOH,0} - F_{EtOH})} \quad (\text{eq. 4.4})$$

$$S_{H_2} = \frac{F_{H_2}}{6(F_{EtOH,0} - F_{EtOH})} \quad (\text{eq. 4.5})$$

$$\%CB = \frac{2F_{EtOH} + \sum_j (nC_j \cdot F_j)}{2F_{EtOH,0}} = 1 - X_{EtOH} \left(1 - \sum_{j \neq H_2} S_j \right) \quad (\text{eq. 4.6})$$

4.3. Results and discussion

4.3.1. Catalyst characterization.

The $Ni_3Al_{1-x}Fe_x$ precursors with $x = 0-1$ were synthesized by coprecipitation at pH 10. The molar Ni/Al/Fe ratios in the samples determined by ICP-OES were close to the nominal ratios (Table 4.1), indicating a proper metal incorporation in the precipitates. Figure 4.1 shows the XRD patterns of the coprecipitated materials and their corresponding products of calcination at 723 K. The Ni_3Al as-synthesized sample display the characteristic reflections of takovite ($Ni_6Al_2(OH)_2(CO_3)16 \cdot 4H_2O$, (15-0087 ICDD pattern). The progressive incorporation of iron in the structure leads to the reevesite pattern in Ni_3Fe , i.e. the Ni-Fe hydroxycarbonate $Ni_6Fe_2(OH)_2(CO_3)16 \cdot 4H_2O$, (40-0215 ICDD pattern).

Table 4.1. Characterization data of the as-synthesized catalysts.

Sample	Ni^{2+}/M^{3+} ^a	Ni:Al:Fe molar ratio ^a / -	$V_p / \text{cm}^3 \text{g}^{-1}$	$S_{BET} / \text{m}^2 \text{g}^{-1}$
Ni_3Al	2.97	3:1.01:0	0.126	37
$Ni_3Al_{0.8}Fe_{0.2}$	3.25	3:0.74:0.18	0.113	29
$Ni_3Al_{0.5}Fe_{0.5}$	3.24	3:0.46:0.47	0.074	22
Ni_3Fe	3.03	3:0:0.99	0.062	23

^a Molar metal ratio in solid by ICP-OES.

As both materials are well identified members of the hydrotalcite family, the building of positively charged brucite-like layers contain Ni, Al, and Fe intermingled with the appropriate ratios in the final solids. All samples are mesoporous, with a low BET surface area in the range 22-34 m² g⁻¹. Thermogravimetric analysis in air (Figure 4.2) shows the typical two-step decomposition pattern of anionic clays. The transition temperature associated with removal of interlayer water appears in the narrow range 434-440 K. The dehydroxylation/decarbonation step is slightly shifted to lower temperatures from the pure Ni₃Al to Ni₃Fe (from 594 K to 552 K). These results are in agreement with previous works on takovite and reevesite structures, and their intrinsic stability [31, 38, 39]. The heat flow profiles show the presence of two endothermic transitions (Figure 4.2, bottom), matching in temperature with TGA results. The total weight losses amount 38, 34, 33, and 33% for Ni₃Al, Ni₃Al_{0.8}Fe_{0.2}, Ni₃Al_{0.5}Fe_{0.5}, and Ni₃Fe, respectively, similar to the theoretical weight losses calculated from their chemical formulae.

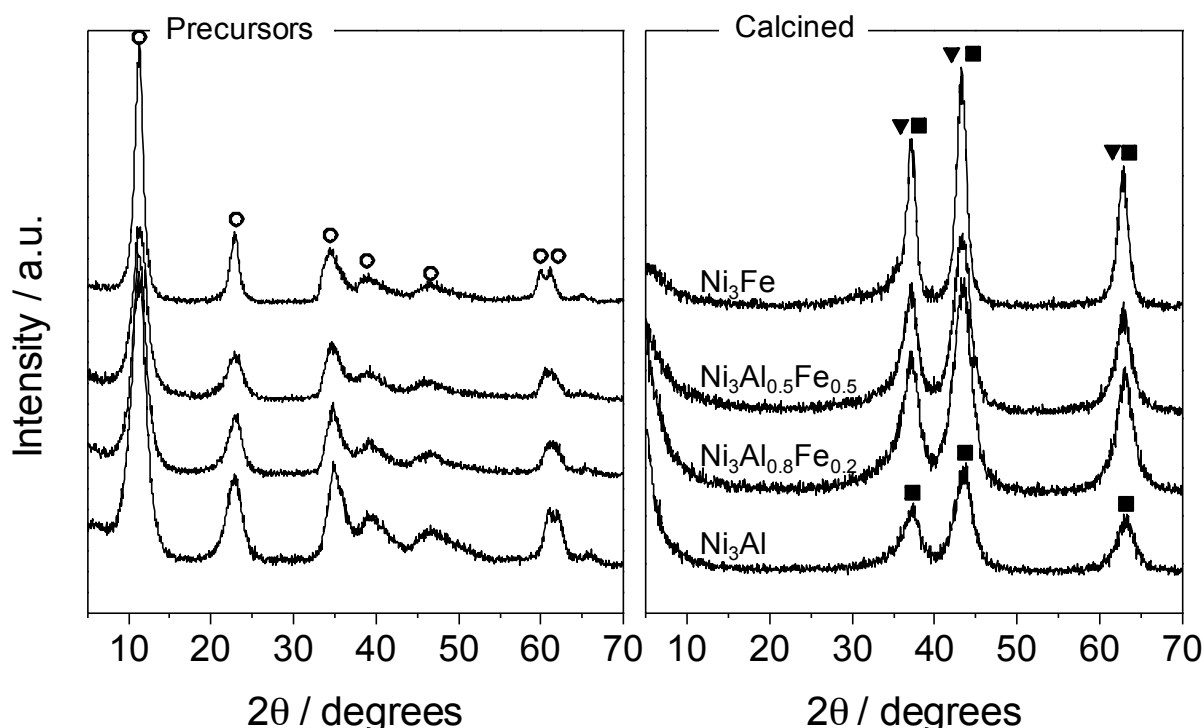


Figure 4.1. XRD patterns of precursors and samples calcined at 723 K. Crystalline phases: (○) hydrotalcite-like phase, (■) Ni(Al/Fe)O, and (▼)Ni_yFe_{1-y}Fe₂O₄ spinel.

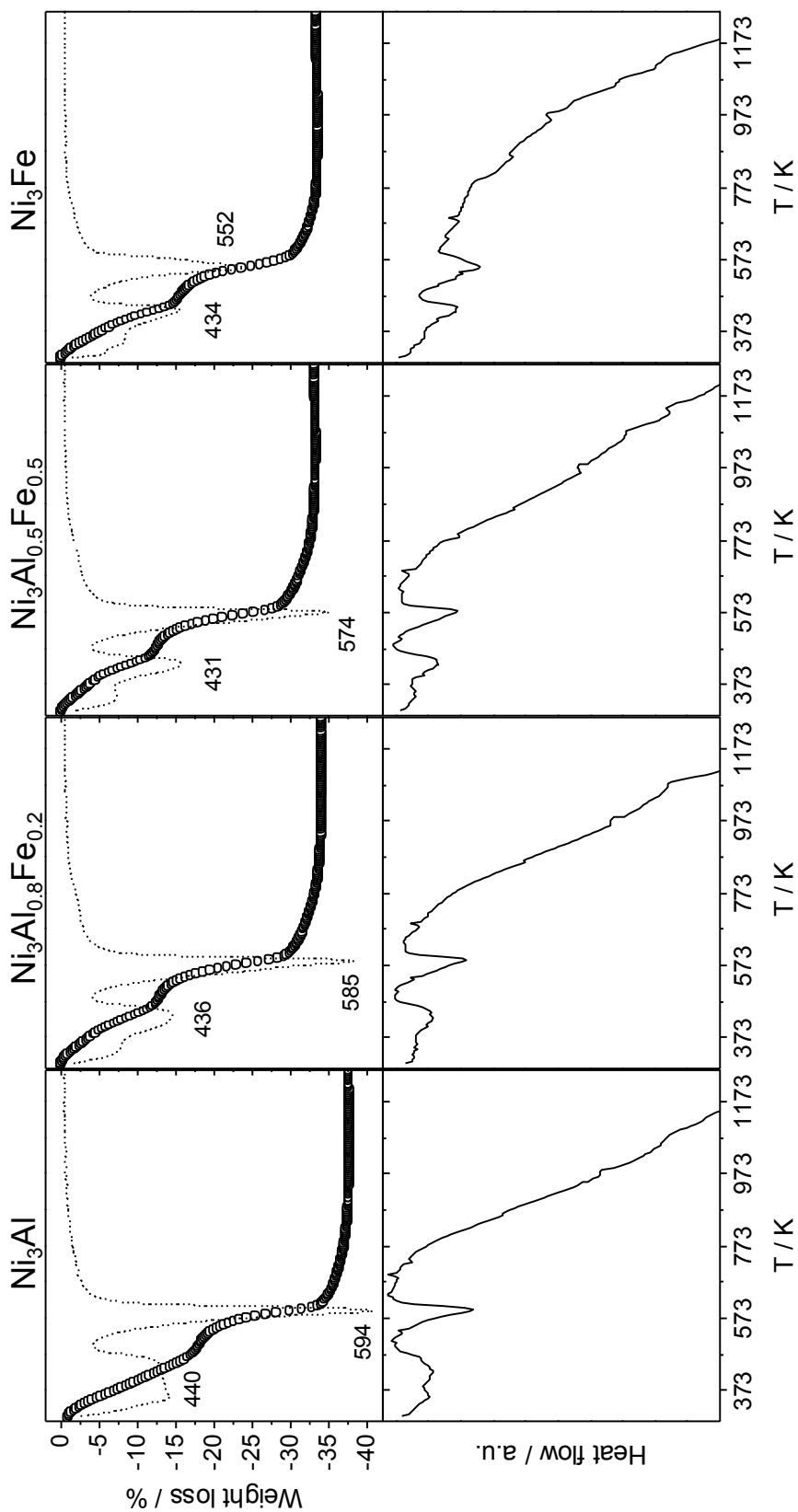


Figure 4.2. Thermogravimetric and calorimetric profiles of the $\text{Ni}_3\text{Al}_{1-x}\text{Fe}_x$ precursors in air and derivative of the weight loss.

The XRD patterns of the solids calcined at 723 K showed characteristic reflections of the NiO-bunsenite structure (47-1049 ICDD pattern) independently of the Ni/M³⁺ (Figure 4.1). Calcination of the takovite and reevesite structures leads to the formation of a solid solution, herein denoted as Ni(Al/Fe)O, with NiO reflections slightly shifted to higher 2 θ values than those corresponding to pure NiO, due to Al³⁺ and/or Fe³⁺ substitution in the nickel oxide lattice [31, 40]. This solid solution was described as a highly disordered metastable mixed oxide phase, [41] intermediate in nature between pure nickel oxide and nickel aluminate. The presence of this metastable phase is confirmed by determination of the cell parameter a of the solid solution in the four samples, which is distinct from that of pure NiO (0.4177 nm) depending on the metal composition (0.4156(4) nm for Ni₃Al, 0.4151(1) nm for Ni₃Al_{0.8}Fe_{0.2}, 0.4164(1) nm for Ni₃Al_{0.5}Fe_{0.5} nm, and 0.4175(1) nm for Ni₃Fe).

As previously observed, [31] the Ni₃Fe sample should comprise a mixture containing Ni(Fe)O and NiFe₂O₄ (trevorite, 54-964 ICDD file, a : 0.8336 nm), which cannot be distinguished from Fe₃O₄ (magnetite, 89-3854 ICDD file a : 0.8394 nm) as they have the same spinel structure type, and the resulting Bragg positions are completely overlapped due to the high peak width. For this reason, the presence of indistinguishable NiFe₂O₄/Fe₃O₄ spinel phases is hereafter referred to as Ni_yFe_{1-y}Fe₂O₄, with y being 0 for magnetite (Fe₃O₄) or 1 for trevorite (NiFe₂O₄).

The quantitative analysis of the phases present in the calcined samples was performed by Rietveld refinement (Table 4.2). Based on the crystalline phases, the amount of Ni_xFe_{1-x}Fe₂O₄ increased upon decreasing the Al/Fe ratio. That is, the spinel structure was found in all iron-containing oxides in a different extent, despite the calcination temperature used (723 K). The percentage of Fe-spinel phase at such low calcination temperature can only be motivated by the presence of increasing loadings of iron. This metal is therefore more prone for spinel formation attending to the stability of the oxide formed (see below). In fact, as long as the amount of iron increases in the calcined samples, the a cell parameter of the NiO phase

approximates that of pure NiO. In the extreme case, the sample with the highest $\text{Ni}_y\text{Fe}_{1-y}\text{Fe}_2\text{O}_4$ content, Ni_3Fe , exhibits an a cell parameter (0.4175(1) nm) that resembles that of pure nickel oxide (0.4177 nm). This suggests that iron is progressively segregated from the solid solution to form the additional $\text{Ni}_y\text{Fe}_{1-y}\text{Fe}_2\text{O}_4$ spinel phase when the amount of iron increases, and the rest of the solid remains as $\text{Ni}(\text{Fe})\text{O}$. Despite the fact that higher temperatures are necessary for pure takovite samples to segregate into NiAl_2O_4 spinel [41, 42] a certain amount of this phase was also detected in the pure Ni_3Al sample. Both NiO and NiAl_2O_4 exhibit a cubic close-packed lattice of O^{2-} ions and differ in the way in which the cation vacancies are filled: Ni^{2+} occupy octahedral sites in NiO and tetrahedral sites in a normal spinel NiAl_2O_4 . The concentration of nickel in tetrahedral sites increases with temperature (>1273 K). However, Ni^{2+} ions display a higher tendency for octahedral sites at lower temperature, leading to inverse nickel aluminate spinel.⁴³ Considering the obtained a cell parameter in Ni_3Al , it is plausible that the detected amount of NiAl_2O_4 spinel is in the inverse form, coexisting with $\text{Ni}(\text{Al})\text{O}$, both with Ni^{2+} in octahedral sites.

Replacement of aluminum by iron did not produce noticeable changes in the $\text{Ni}(\text{Al}/\text{Fe})\text{O}$ crystallite size (Table 4.2), which was in the narrow range of 2.9–5.4 nm for the different samples as obtained from the Rietveld refinement method. Nitrogen adsorption reveals similar values of BET surface area upon calcination of the precursors, with the exception of Ni_3Fe , which displays ca. half the surface area of the other counterparts.

The formation of the $\text{Ni}_y\text{Fe}_{1-y}\text{Fe}_2\text{O}_4$ spinel phase was also confirmed by Raman spectroscopy (Figure 4.3). The broad band at 536 cm^{-1} , attributed to the Ni-O stretching mode [44] of the NiO structure is shifted to higher wavenumber with increasing amounts of iron, up to 566 cm^{-1} in the pure Ni_3Fe oxide sample. In the latter sample, a new peak centered at 701 cm^{-1} , was also evident, which is mainly related to the spinel phase [45]. From comparison of the Raman mode frequencies of the Ni_3Fe sample with previous works, the peak appearing at higher wavenumber could be likely ascribed to trevorite (NiFe_2O_4 , A_{1g} mode at 700 cm^{-1} and

T_{2g} mode at 579 cm^{-1}) rather than magnetite (Fe_3O_4 , A_{1g} mode at 668 cm^{-1} and T_{2g} mode at 538 cm^{-1}) [46, 47]

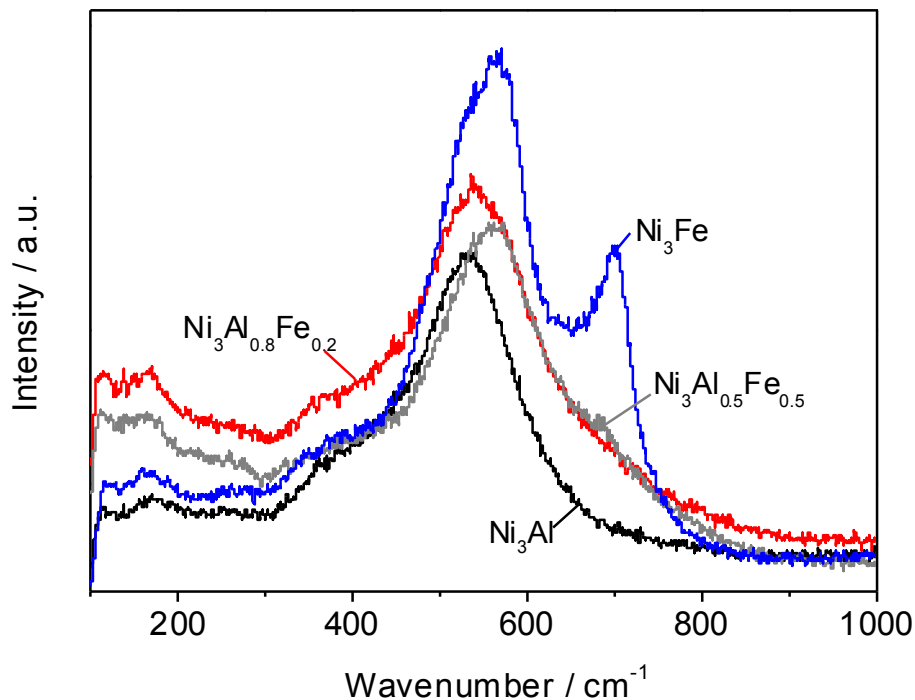


Figure 4.3. Raman spectra of the $\text{Ni}_3\text{Al}_{1-x}\text{Fe}_x$ oxides obtained upon calcination at 723 K. Phases: (■) $\text{Ni}(\text{Al}/\text{Fe})\text{O}$ and (▼) $\text{Ni}_y\text{Fe}_{1-y}\text{Fe}_2\text{O}_4$ spinel.

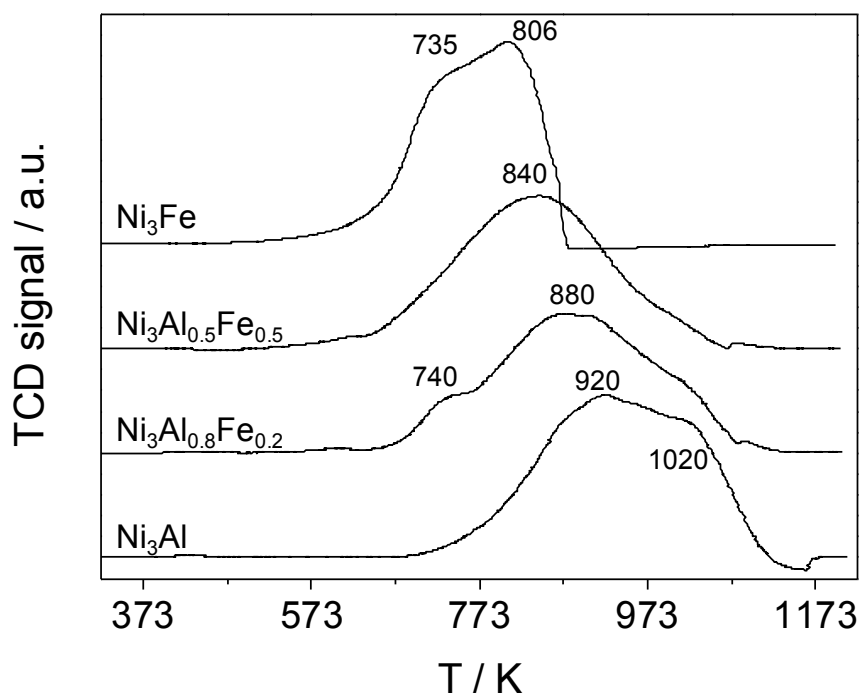


Figure 4.4. H_2 -TPR profiles of the $\text{Ni}_3\text{Al}_{1-x}\text{Fe}_x$ oxides.

Table 4.2. Characterization data of the calcined and used catalysts

Sample code	Phase composition ^a / %						Crystallite size ^b / nm			V_p / cm ³ g ⁻¹	S_{BET} / m ² g ⁻¹
	Ni(Al/Fe)O	NiAl ₂ O ₄	Ni _y Fe _{1-y} Fe ₂ O ₄ spinel ^c	Ni	non-crystalline carbon	Ni(Al/Fe)O	spinel ^d	Ni			
Ni ₃ Al	78.31	21.69	-	-	-	2.96	1.40	-	0.404	163	
Ni ₃ Al _{0.8} Fe _{0.2}	84.26	-	15.74	-	-	2.90	1.24	-	0.371	173	
Ni ₃ Al _{0.5} Fe _{0.5}	81.23	-	18.77	-	-	3.24	1.12	-	0.361	158	
Ni ₃ Fe	75.95	-	24.05	-	-	5.36	1.49	-	0.201	73	
Ni ₃ Al-U	-	-	-	4.32	95.68	-	-	11.48	0.169	126	
Ni ₃ Al _{0.8} Fe _{0.2} -U	-	-	-	3.14	96.86	-	-	10.33	0.257	187	
Ni ₃ Al _{0.5} Fe _{0.5} -U	-	-	-	2.77	97.23	-	-	11.45	0.228	182	
Ni ₃ Fe-U	2.86	-	2.34	4.70	90.1	6.59	36.15	22.91	0.464	170	

^a Crystalline phase composition determined by Rietveld refinement in calcined samples, and by PONCKS in used samples. ^b Average crystallite size obtained by refinement of the whole profile. The weighted residual error was in the range 0.3-3% for both crystallite size and phase composition. ^c $x = 0$ (magnetite, Fe₃O₄) or 1 (trevorite, NiFe₂O₄). ^d Ni_yFe_{1-y}Fe₂O₄ spinel according to phase composition.

Although this is the first indication of the presence of trevorite in the Ni_3Fe sample instead of magnetite, the latter phase cannot be totally discarded.

Temperature programmed reduction profiles of the calcined samples are shown in Figure 4.4. The reduction of nickel occurs in the broad range of 573-1173 K depending on the oxide composition. In fact, the reduction of pure NiO typically displays a single peak at 613-670 K [24]. The reduction of nickel in Ni(Al/Fe)O solid solutions is hindered by both aluminum [42, 48, 49] and iron, [31] producing a shift to higher reduction temperatures with respect to pure NiO. The binary Ni_3Al oxide shows a peak of hydrogen consumption centered at 920 K, with shoulders of noticeable intensity at 870 and 1020 K. This broad reducibility range was previously attributed to the presence of a multiple spectrum of nickel structures in terms of interaction with aluminum [41]. The TPR maximum shifts to lower temperatures upon increasing the iron content in the final oxide, indicating the lower stability of the Fe-containing samples. The reduction of Fe_2O_3 and NiO frequently proceeds over almost the same temperature range (573-973 K), but the reduction of iron oxides may occur in various steps in the order $\text{Fe}_2\text{O}_3 \rightarrow \text{Fe}_3\text{O}_4 \rightarrow \text{FeO} \rightarrow \text{Fe}^0$, from 573 to 1000 K [50]. In sample $\text{Ni}_3\text{Al}_{0.8}\text{Fe}_{0.2}$, a small shoulder at 740 K appears, which was not present in the Al-counterpart. This shoulder may be attributed to Fe^{3+} reduction into Fe^{2+} , and the broad peak centered at 880 K covers the reduction of Ni(Al/Fe)O and $\text{Ni}_y\text{Fe}_{1-y}\text{Fe}_2\text{O}_4$ species, as well as reduction of Fe^{2+} to Fe^0 [31]. This can be confirmed by the increase in intensity of the shoulder at 740 K with the increase in iron content, which appears below the broad curve in $\text{Ni}_3\text{Al}_{0.5}\text{Fe}_{0.5}$, and finally, as a high-intensity shoulder at 735 K in Ni_3Fe . The increment of iron in the samples, and therefore, the decrease in aluminum from $\text{Ni}_3\text{Al}_{0.8}\text{Fe}_{0.2}$ to Ni_3Fe infers that the broad reducibility profile covers the reduction of a lower amount of Ni(Al)O species, and a higher amount of Ni(Fe)O species when the amount of Fe increases. These results suggest an intimate interaction of aluminum/iron and nickel in the solid solution. This is supported by

XRD, as the reflections of NiO appear at higher 2θ values in all samples than in pure NiO, indicating smaller cell parameters (see above).

4.3.2. Steam reforming performance.

The catalytic activity of the four materials was tested for ethanol steam reforming during nearly 95 h of time-on-stream at constant reaction conditions. Experiments were performed at 773 K and atmospheric pressure, using a water-to-ethanol molar ratio of 6 and a weight hourly space velocity (WHSV) of $147.45 \text{ mol ethanol h}^{-1} \text{ kg}_{\text{cat}}^{-1}$. No reduction pretreatment was performed over the calcined catalysts before reaction. Therefore, nickel species were gradually reduced under reaction conditions, as confirmed by XRD (section 3.3). Figure 4.5 shows the conversion and selectivity towards reaction products for the four catalysts with time on stream. Average carbon balances during the reforming experiments were above 90% in all runs.

The activity of the Ni₃Fe catalyst decreased sharply during the first 15 h, from complete conversion to ca. 40%, and decreased very slowly afterwards to a conversion of 30% at 90 h of reaction. The initial change in activity was related to significant variations in product selectivity. Carbon dioxide, hydrogen and carbon monoxide were the dominant products during the initial stages of the experiment, but selectivity shifted towards a maximum in acetaldehyde (ca. 42%) at around 5 h of reaction time, together with the simultaneous decrease of hydrogen and carbon oxides. The incipient decrease in conversion at the beginning of the reaction test suggests that coke deposition takes place during the in situ catalyst conditioning period. During this period, carbon balances were slightly lower, and they improved at longer time on stream. After 15 h, when the catalyst deactivation rate slowed, acetaldehyde selectivity stabilized at around 35%, and that of carbon dioxide and hydrogen increased again. Also, the initial selectivity to ethylene was low (ca. 3%), and decreased monotonically to very small values (0.3% at 30h). Results show that the catalyst favored ethanol dehydrogenation to acetaldehyde instead of direct steam reforming of ethanol or

ethanol dehydration into ethylene, followed by acetaldehyde reforming and/or acetaldehyde cracking to methane and carbon monoxide, combined with the reversible reactions of water-gas shift and methanation. Even if only minor amounts of ethylene were observed, carbon was deposited on the catalyst surface (see below), thus causing the drop in catalyst activity and conversion observed during the first 15 h.

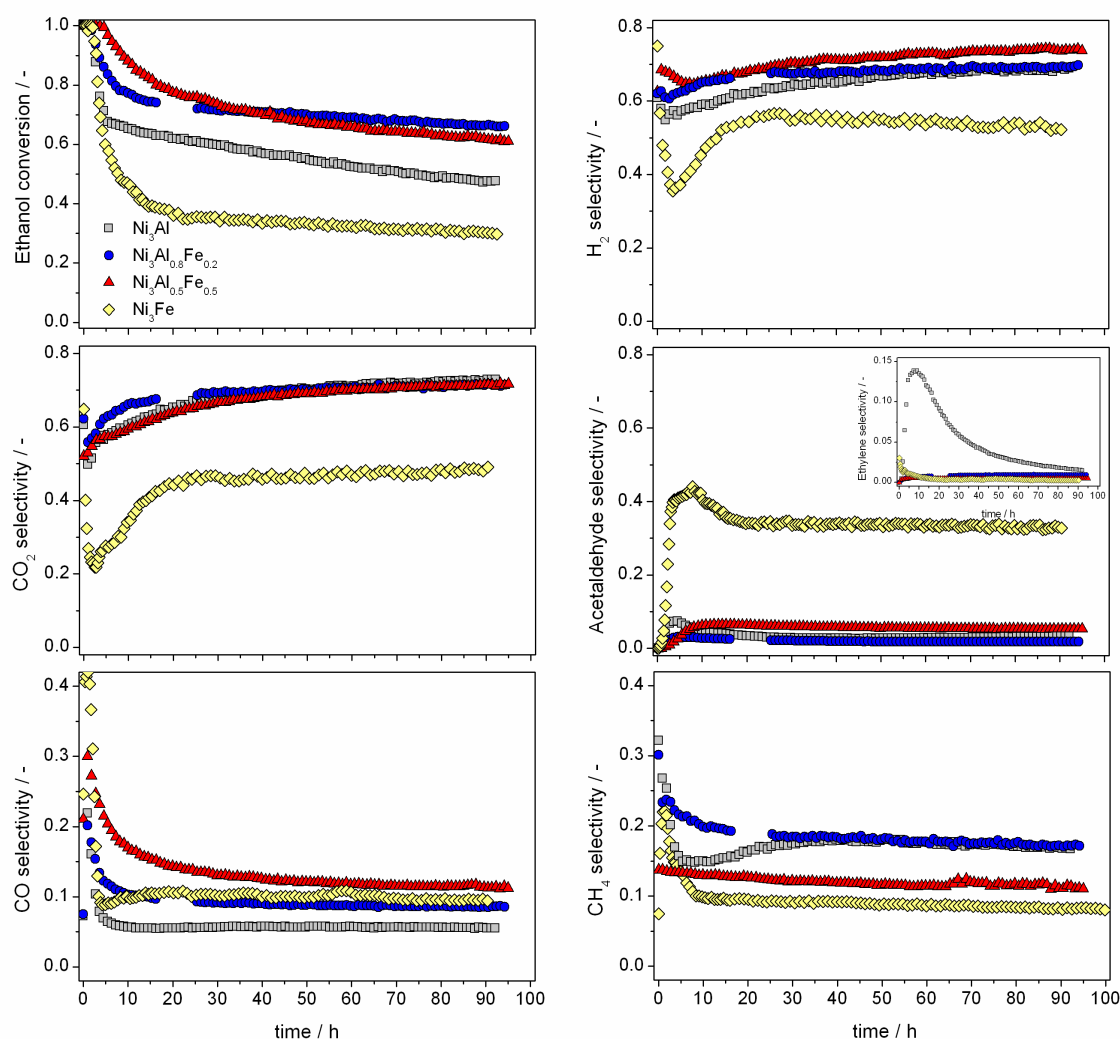


Figure 4.5. Ethanol conversion and selectivity to the different products vs time during ethanol steam reforming over $\text{Ni}_3\text{Al}_{1-x}\text{Fe}_x$ samples calcined at 723 K. Conditions: $\text{H}_2\text{O}/\text{C}_2\text{H}_5\text{OH}$ ratio = 6, $T = 773$ K, $\text{WHSV} = 147.45 \text{ mol ethanol h}^{-1} \text{ kg}_{\text{cat}}^{-1}$, and $P = 1$ bar.

Results suggest that carbon was deposited preferentially on the most reactive sites of the surface, and once those sites were blocked carbon deposition rate decreased substantially. After 30 h, ethanol conversion stabilized at 35 % and selectivity to acetaldehyde at 33%.

Selectivity to hydrogen, carbon dioxide, carbon monoxide and methane were 55%, 47%, 10% and 9%, respectively, at the end of the reaction period. It should be noted that the low ethanol conversion can be in part also due to the lower surface area of the Ni₃Fe catalyst compared to the other catalyst compositions (Table 4.2). However, this is not the only factor affecting the activity as the incorporation of iron in the samples produces a notorious effect in selectivity.

The Ni₃Al catalyst showed the typical behavior of steam-reforming catalysts based on nickel/alumina, the most commonly used support for commercial Ni steam reforming catalysts [51, 52]. The fresh catalyst achieved complete conversion of ethanol producing carbon dioxide and hydrogen as the main products. Ethylene increased steadily and reached a maximum selectivity of 14% at around 10 h of reaction, thus indicating the much more acidic nature of this catalyst, which would be responsible for ethanol dehydration. When reduction is initiated, Ni particles not only nucleate on the surface of the Ni(Al)O rich crystallites, but also aluminum ions diffuse to the surface of the crystallites, and alumina phases nucleate. The alumina phase should exhibit a low crystallinity, as no evidences of such a phase are detected by XRD. This is supported by the model of Alzamora et al.,[30, 49] leading to the presence of active Lewis acid sites in the Ni₃Al catalyst (i.e. Al³⁺ and Ni²⁺).⁵³ This behavior would suggest that Ni²⁺ species are the active species in the beginning of the reaction, which are gradually transformed into Ni⁰ upon time on stream. Once formed, Ni⁰ intermingled with the alumina phase become the active species for dehydrogenation to acetaldehyde and subsequent reforming. The formation of ethylene caused the catalyst to gradually deactivate through the formation of filamentous carbon (see section 3.3). After only 3 h, the conversion dropped to around 70%, although the rate of deactivation was reduced afterwards and conversion decreased steadily with time on stream to a value of 48% after 90 h. The rate of deactivation qualitatively correlated with the decrease in ethylene selectivity with time on stream, which indicates that carbon deposition tended to block the acidic sites, responsible for ethanol dehydration to ethylene [54-56]. The lower the selectivity to ethylene, the higher the

selectivity to hydrogen and carbon dioxide, and the slower the rate of deactivation. Acetaldehyde was also produced by dehydrogenation, but its selectivity reached only a maximum of 8% after 5 h of reaction and decreased steadily further along the experiment. This indicates that ethanol was converted through direct steam reforming and dehydration on the acidic sites, preferentially by dehydrogenation to acetaldehyde, which is a common behavior on Ni/alumina catalysts [5].

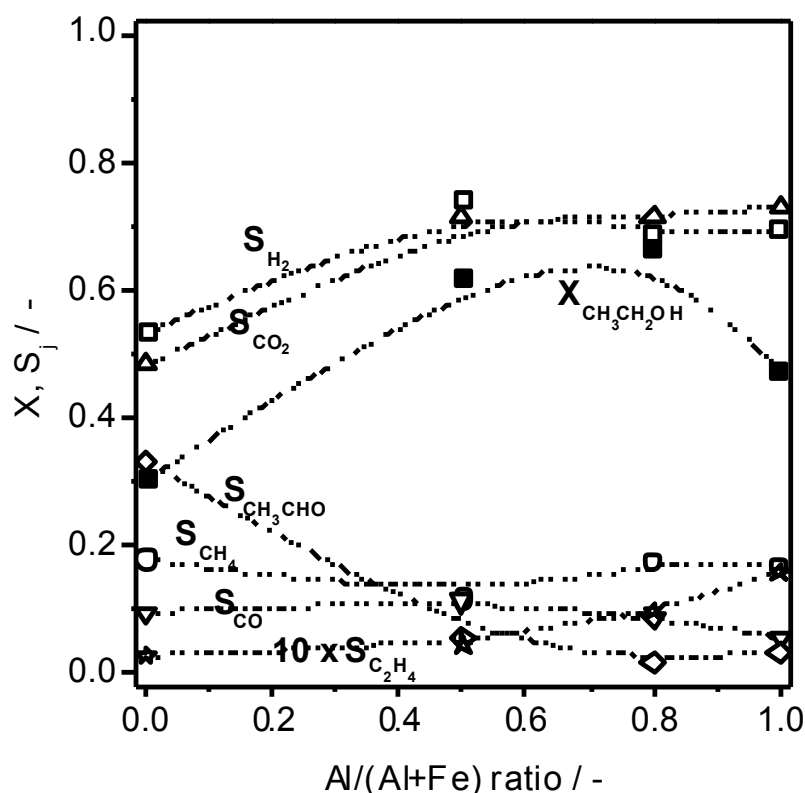


Figure 4.6. Ethanol conversion and selectivity to the different products vs the degree of aluminum replacement by iron in the $\text{Ni}_3\text{Al}_{1-x}\text{Fe}_x$ catalysts. Conditions: $\text{H}_2\text{O}/\text{C}_2\text{H}_5\text{OH}$ ratio = 6, $T = 773 \text{ K}$, $t = 30 \text{ h}$, $\text{WHSV} = 147.45 \text{ mol ethanol h}^{-1} \text{ kg}_{\text{cat}}^{-1}$, and $P = 1 \text{ bar}$.

The two ternary materials ($\text{Ni}_3\text{Al}_{0.8}\text{Fe}_{0.2}$ and $\text{Ni}_3\text{Al}_{0.5}\text{Fe}_{0.5}$) presented similar behavior, but distinct from those of the Ni_3Al and Ni_3Fe catalysts. Both materials experienced partial deactivation at the beginning of the experiment, but maintained higher conversion than the Ni_3Fe and Ni_3Al catalysts. Figure 4.6 compares conversion and product selectivity for the four catalysts after 90 h of time on stream. The binary catalysts, in the two corners of the

graph, showed a final conversion of 47% and 30% for Ni_3Al and Ni_3Fe , respectively. The $\text{Ni}_3\text{Al}_{0.8}\text{Fe}_{0.2}$ catalyst had the highest conversion (66%), closely followed by the $\text{Ni}_3\text{Al}_{0.5}\text{Fe}_{0.5}$ (61%). The latter had a selectivity towards hydrogen and carbon oxides slightly higher than the $\text{Ni}_3\text{Al}_{0.8}\text{Fe}_{0.2}$, and a lower selectivity to methane. Selectivity to acetaldehyde and ethylene was low for both catalysts, the $\text{Ni}_3\text{Al}_{0.8}\text{Fe}_{0.2}$ yielding more ethylene and less acetaldehyde than the $\text{Ni}_3\text{Al}_{0.5}\text{Fe}_{0.5}$. As a general trend, acetaldehyde decreased and ethylene increased with the $\text{Al}/(\text{Al}+\text{Fe})$ ratio, thus supporting the fact that the presence of Fe favors ethanol dehydrogenation while Al tends to promote dehydration. Similar effects were also found in the auto-thermal reforming of ethanol to hydrogen using Ni-based spinel catalysts doped with iron, in which the latter metal exerts a positive role in the enhancement of activity and hydrogen selectivity [28, 57, 58].

Because of its higher conversion and better stability with time on stream, the $\text{Ni}_3\text{Al}_{0.8}\text{Fe}_{0.2}$ catalyst was also tested at 823 and 873 K to determine the effect of reaction temperature on its overall performance, and on the presence of oxygenate products. Figure 4.7 shows the fractional conversion and the product selectivity at the three reaction temperatures for 90 h experiments. A fresh batch of catalyst was used for each experiment. Complete conversion was obtained at 823 K for nearly 90 h but a slight decrease was observed afterwards, coincidentally with the detection and increase of acetaldehyde and ethylene in the reformat gas. In fact, the first indication of catalyst deactivation was observed after 80 h, when the selectivity to carbon monoxide tended to increase and that to carbon dioxide to decrease. Complete conversion was also obtained at 873 K and no deactivation was observed for 95 h. Acetaldehyde and ethylene were not detected in the reformat. Selectivity to hydrogen and carbon oxides was higher than at 823 K and the selectivity to methane lower. The differences in selectivity were caused by temperature, but also influenced by the degree of conversion attained in the reactor. At 773 K, conversion of C2 species was incomplete and carbon oxides and hydrogen, the products from ethanol direct reforming, were predominant over methane.

At 823 K, ethanol conversion was complete and an excess of catalyst was available in the reactor to tend to equilibrate hydrogen, carbon oxides and methane through the methanation reaction. The same was true at 873 K, but because of the higher temperature less methane and more H₂ and CO were formed.

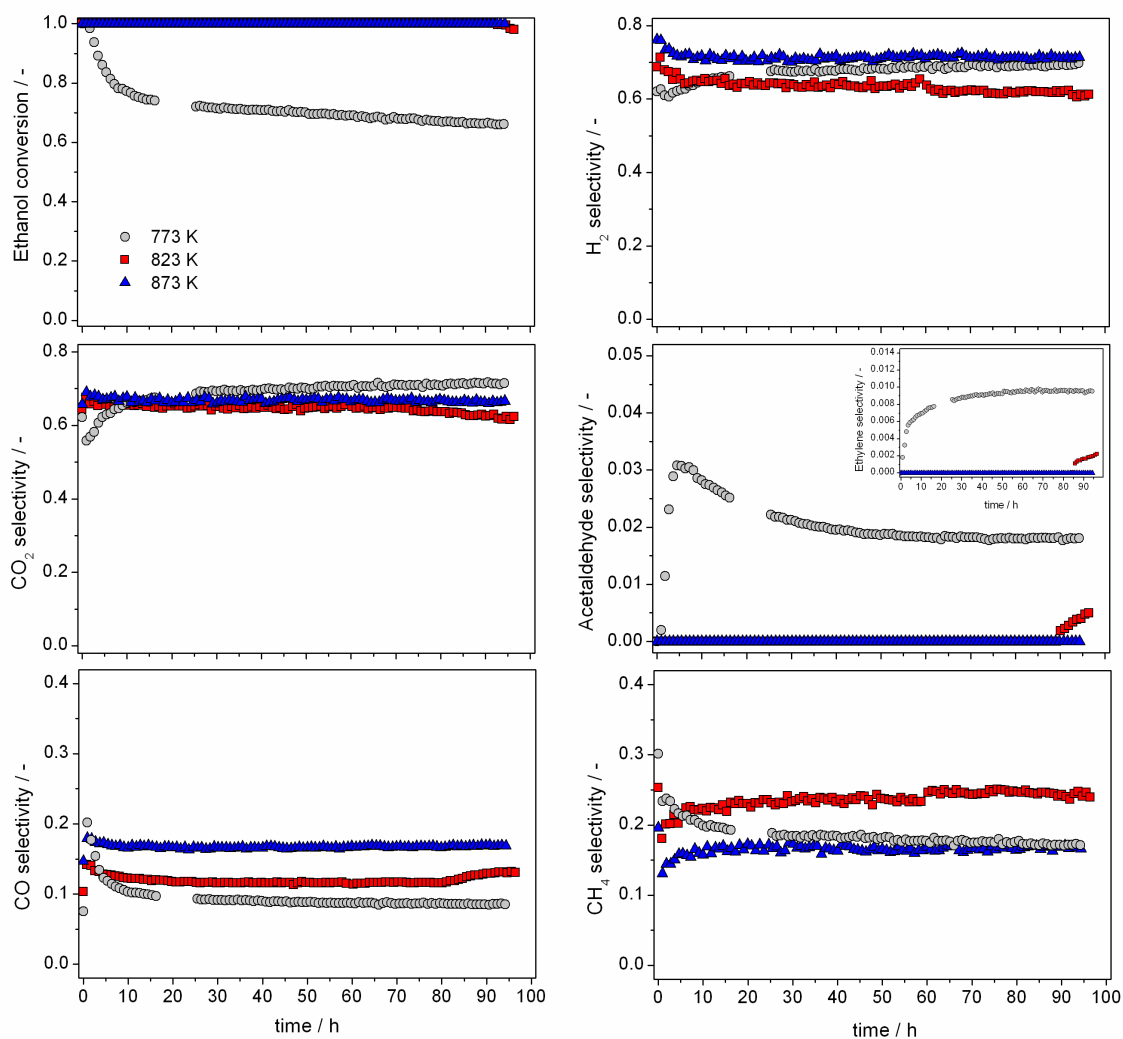


Figure 4.7. Ethanol conversion and selectivity to the different products vs time during ethanol steam reforming at different temperatures over Ni₃Al_{0.8}Fe_{0.2} calcined at 723 K. Conditions: H₂O/C₂H₅OH ratio = 6, WHSV = 147.45 mol ethanol h⁻¹ kg_{cat}⁻¹, and P = 1 bar.

Based on the aforementioned behavior for each catalyst, it seems that the incorporation of Fe during synthesis of the Ni-Al precursor promotes the activity of the mixed oxide catalyst by favoring ethanol dehydrogenation as the primary step, followed by acetaldehyde reforming and/or cracking, reverse water gas shift, and methanation. However, an excess of iron (pure

Ni₃Fe catalyst) results in an increment in the production of acetaldehyde (Figure 4.5), and a subsequently loss of activity of acetaldehyde transformation to C1 products and H₂. This is corroborated by the lower H₂ and CO₂ selectivity and the higher acetaldehyde amount after the 90 h reaction test (Figure 4.6) in the pure Ni-Fe catalyst.

The enhancement in the catalytic activity can be then attributed to a synergic effect by iron-nickel-aluminum on the electronic and structural properties, which is not present in the separate binary counterparts. This effect favors the dehydrogenation route, accompanied by a higher activity of acetaldehyde transformation into CO₂ (and C1 products in general) and H₂, and reduces ethylene formation. The presence of iron in the ternary system improves the reducibility of nickel (as confirmed by the shifting in temperature in the H₂-TPR in Figure 4.4), and likely affects its acidity by replacement of aluminum by iron, as less acid sites from Al⁺³ are present, thus restraining the ethanol dehydration route.

4.3.3. Characterization of used catalysts

All catalysts were characterized after reaction. Since no reduction pretreatment was performed over the calcined catalysts before reaction, nickel species in both catalysts were progressively reduced under reaction conditions, as confirmed by XRD (Figure 4.8). After the 90 h test, the original Ni(Al/Fe)O reflections in the calcined samples are not present in the used catalysts, and two reflections at 2θ 44° and 52° (4-850 ICDD pattern) associated with Ni⁰ emerged. The alumina phase, following the model of Alzamora et al. [49], likely formed upon reduction of the aluminum-containing samples was not detected by XRD, and therefore, it was not considered for calculations. Exceptionally, additional diffraction lines at 2θ 30°, 35.5°, 37.5°, 43°, 57°, and 62° were present in Ni₃Fe, which correspond to the growing of Ni_yFe_{1-y}Fe₂O₄ spinel under reaction conditions, as well as a certain percentage of Ni(Fe)O. The broad diffraction peak at 2θ 25.79° and the small one at 43.25° in all used samples is associated with the formation of deposited non-crystalline carbon upon reaction.

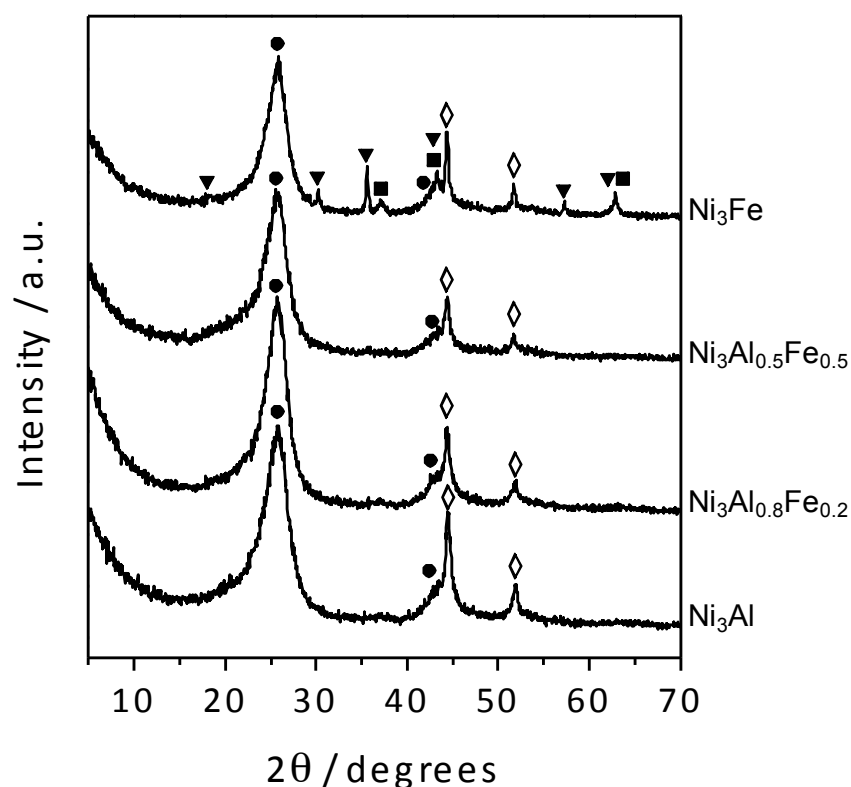


Figure 4.8. XRD patterns of the used $\text{Ni}_3\text{Al}_{1-x}\text{Fe}_x$ samples. Crystalline phases: (■) $\text{Ni}(\text{Al}/\text{Fe})\text{O}$, (▼) $\text{Ni}_y\text{Fe}_{1-y}\text{Fe}_2\text{O}_4$, (◇) metallic Ni, (●) carbon deposition.

These two peaks are similar to the peaks produced by Graphite-2H (41-1487 ICDD pattern) but the diffractogram of the used samples cannot be fitted correctly with the structure of this graphite. The intensity of this diffraction peak is very similar in all cases, suggesting a close tendency for coke formation independently of the M^{3+} composition. Due to the unknown crystal structure of the formed non-crystalline carbon, quantification by Rietveld refinement is not sufficiently accurate to determine both the percentage of phases and Ni crystallite size. Therefore, the recent established PONCKS approach was applied. A sample with a high content of non-crystalline carbon plus Ni was mixed with a 14 wt.% of Si (NIST SRM 640b). The resulting diffractogram was fitted assigning an arbitrary space group and cell parameters to the non-crystalline carbon phase in order to fit perfectly the diffractogram. Once the fitting was finished, all intensities for this phase were fixed and the constant (ZM) was calculated (section 2.2). In subsequent diffractograms, it was only needed to adjust the

Rietveld scale factor for all phases present (including non-crystalline carbon) to estimate their percentage. Figure 4.S1 (Appendix for chapter 4) shows the good agreement between the observed diffractogram and the calculated one as the sum of the individual diffractograms produced by each phase for the $\text{Ni}_3\text{Al}_{0.8}\text{Fe}_{0.2}\text{-U}$ sample. From this method, a low Rietveld agreement factor was achieved, which indicates the good compromise between calculated and original diffractograms. This method also allowed a better estimation of the crystallite size from the peak broadening when a non-crystalline phase is present. Based on the values estimated (Table 4.2), the amount of both $\text{Ni}(\text{Al/Fe})\text{O}$ and $\text{Ni}_y\text{Fe}_{1-y}\text{Fe}_2\text{O}_4$ spinel decrease at the expenses of Ni^0 formation after reaction, and complete reduction is achieved after the 90 h-reaction tests in the aluminum-containing samples. In agreement with previous results [31], a certain amount of $\text{Ni}_y\text{Fe}_{1-y}\text{Fe}_2\text{O}_4$ spinel was still present in the sample with higher iron content, that is, in the pure Ni_3Fe . Despite the lower stability towards reduction of the iron-containing samples with respect to pure Ni_3Al (Figure 4.4), the presence of the Fe-spinel phase ($\text{Ni}_y\text{Fe}_{1-y}\text{Fe}_2\text{O}_4$) hinders the total reduction of Ni species into Ni^0 at 773 K.

The amount of metallic nickel was in the range 2.8-4.7%, being slightly smaller in the ternary systems. The average crystallite size of metallic nickel was around 11 nm in the aluminum-containing samples, but it substantially increased in the used binary $\text{Ni}_3\text{Fe-U}$ sample to ca. 23 nm. Besides, the crystallite size of the spinel phase in this catalyst after reaction is one order of magnitude higher than in the fresh catalyst. These results are interesting as the Ni-Al-Fe samples are more active than the binary counterparts, and reveal that the Ni^0 size and dispersion are more important than the amount of metallic nickel for improved performance. Concomitantly, these samples exhibited the largest amount of carbon deposits. In all cases, the amount of graphite gets over 90%, which is a relatively high value after the 90 h test reaction. The BET surface area of the fresh catalysts was practically unaffected after reaction despite the amount of coke formed.

The drop in activity observed for the Ni_3Fe catalyst in the first 15 h of reaction (Figure 4.5) is indicative of the high tendency for deactivation motivated by sintering of the active metal, together with the large amount of carbon deposits detected by XRD. The deactivation observed in the Ni_3Al catalyst was mainly due to polymerization into coke through ethanol dehydration to ethylene. As observed in section 3.2, this catalyst displayed a significant amount of this product in the first 10 h of reaction (Figure 4.5).

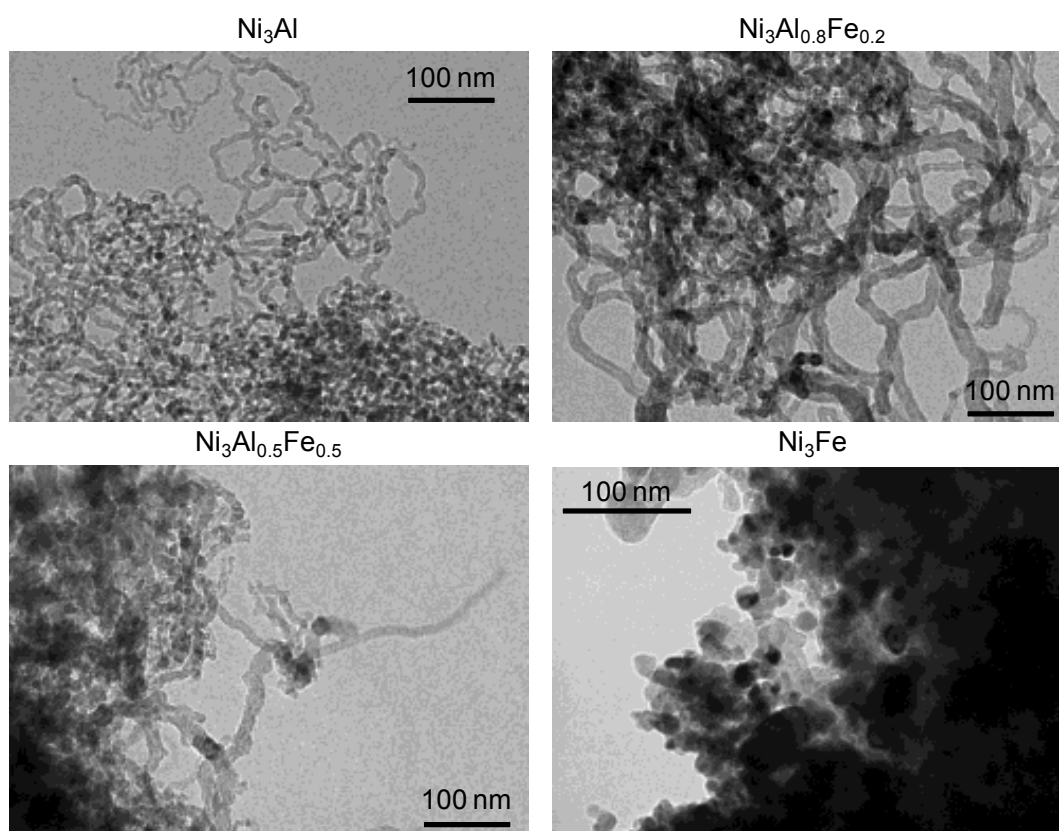


Figure 4.9. Transmission electron micrographs of the $\text{Ni}_3\text{Al}_{1-x}\text{Fe}_x$ samples after 90 h-ESR.

The presence of carbonaceous deposits was also evident by microscopy. Figure 4.9 shows selected micrographs of all catalysts after the 90 h reaction ESR test. All the aluminum-containing samples show the presence of dark nanoparticles of around 7-10 nm in average diameter, which seem to belong to Ni^0 particles intermingled with alumina-iron phases. Besides, carbon nanofibers, located at their tip apexes are also clearly discerned. It was

previously reported that this type of carbon results from adsorbed carbon on a Ni particle [59], which nucleates into a fiber. In such cases, most of the nickel crystal is still active and only part of it is blocked by the growing of the carbon fiber, thus leading to a gradual deactivation. In our nickel-aluminum-iron samples, mainly consisting of Ni⁰ particles (Figure 4.8) merged with Ni_yFe_{1-y}Fe₂O₄ species (likely reduced into Fe²⁺ and/or Fe⁰) and alumina phase (neither of them detected by XRD), a gradual deactivation is also observed (Figure 4.5). This is indicative and confirms previous observations on the lower deactivation attained by those catalysts where whisker or fiber carbon dominates. Additionally, the improved catalytic performance of the Ni-Al-Fe catalysts could be also due to the formation of small Ni nanoparticles upon conditioning and coke formation, which would likely lead to the stabilization of such particles on carbon (acting then as support).

No carbon filaments were observed by TEM in the Ni₃Fe sample, but considering the fast decrease in ethanol conversion, other type of coke deposits can be formed upon reaction, i.e. gum carbon. This type of carbon leads to rapid catalyst deactivation by carbon encapsulation of the metal.⁵⁹ Besides, large nickel particles were clearly discerned, which are also responsible for deactivation through sintering. These two effects would explain the fast deactivation of this catalyst compared to the aluminum-containing catalysts.

4.4. Conclusions

The steam reforming of ethanol over Ni-Al, Ni-Fe and Ni-Al-Fe mixed oxides derived from takovite, reevesite and mixtures thereof, prepared through the hydrotalcite route (coprecipitation), was investigated. Binary systems exhibit a significant deactivation. The Ni₃Al behaves as a typical reforming catalyst, favoring both ethanol dehydrogenation and dehydration, the latter being responsible for ethylene formation and subsequent gradual and slow polymerization into coke. On the opposite side, the Ni₃Fe catalyst experiences a fast deactivation, mainly related to both fast coke formation and nickel sintering, as demonstrated

by characterization of the used materials. In the intermediate situation, Ni-Al-Fe oxides are more active catalysts than their binary counterparts for ESR, rendering high and stable hydrogen selectivity of up to ca. 70%. A synergic effect in the electronic, structural and activity properties of the resulting oxides between the three metals is manifested. A gradual increase in iron reduces the undesired process characteristic of pure nickel-alumina catalysts, i.e. ethylene production by Al^{3+} Lewis acid sites. This cooperative effect favors ethanol dehydrogenation as the primary step, followed by acetaldehyde reforming and/or cracking, reverse water gas shift, and methanation, and in parallel, restrains the dehydration route to ethylene. Although more studies are still required to improve the stability of these materials, for instance, by incorporation of alkaline promoters to decrease carbon formation, the activity of the nickel-based ternary systems is remarkable.

4.5. References

- [1] R. J. Pearson, J. W. G. Turner, *Comprehensive Renewable Energy* 5 (2012) 305-342.
- [2] L. F. Brown, *Int. J. Hydrogen Energy* 26 (2001) 381-397.
- [3] J. Xuan, M. K. H. Leung, D. Y. C. Leung, M. Ni, *Renew. Sustain. Energy Rev.* 13 (2009) 1301-1313.
- [4] D. Montané, E. Bolshak, S. Abelló, *Chem. Eng. J.* 175 (2011) 519-533.
- [5] A. N. Fatsikostas, X. E. Verykios, *J. Catal.* 225 (2004) 439-452.
- [6] M. Ni, D. Y. C. Leung, M. K. H. Leung, *Int. J. Hydrogen Energy* 32 (2007) 3238-3247.
- [7] A. Haryanto, S. Fernando, N. Murali S. Adhikari, *Energy Fuels* 19 (2005) 2098-2106.
- [8] M. Benito, J. L. Sanz, R. Isabel, R. Padilla, R. Arjona L. Daza, *J. Power Sources* 151 (2005) 11-17.
- [9] P. K. Sharma, N. Saxena, A. Bhatt, C. Rajagopal P. K. Roy, *Catal. Sci. Technol.* 3 (2013) 1017-1026.
- [10] M. Bilal, S. D. Jackson, *Catal. Sci. Technol.* 3 (2013) 754-766.
- [11] A. Bshish, Z. Yakoob, B. Narayanan, R. Ramakrishnan A. Ebshish, *Chem. Papers* 65 (2011) 251-266.
- [12] G. F. Froment, *Catal. Rev.* 50 (2008) 1-18.
- [13] K. Egeblad, J. Rass-Hansen, C. C. Marsden, E. Taarning C. H. Christensen, in *Catalysis*, eds. J. J. Spivey and K. M. Dooley, The Royal Society of Chemistry, Cambridge, 2009, vol. 21, pp. 13-50.
- [14] W. T. Reichle, *J. Catal.* 94 (1985) 547-557.
- [15] F. Cavani, F. Trifirò A. Vaccari, *Catal. Today* 11 (1991) 173-301.
- [16] D. Tichit, B. Coq, *CATTECH* 7 (2003) 206-217.
- [17] A. Vaccari, *Catal. Today* 41 (1998) 53-71.
- [18] J. Comas, M. L. Dieuzeide, G. Baronetti, M. Laborde, N. Amadeo, *Chem. Eng. J.* 118 (2006) 11-15.
- [19] V. Mas, M. L. Dieuzeide, M. Jobbágy, G. Baronetti, N. Amadeo, M. Laborde, *Catal. Today* 133-135 (2008) 319-323.
- [20] I. O. Cruz, N. F. P. Ribeiro, D. A. G. Aranda, M. M. V. M. Souza, *Catal. Commun.* 9 (2008) 2606-2611.
- [21] C. Resini, T. Montanari, L. Barattini, G. Ramis, G. Busca, S. Presto, P. Riani, R. Marazza, M. Sisani, F. Marmottini, U. Costantino, *Appl. Catal. A* 355 (2009) 83-93.
- [22] G. Busca, U. Costantino, T. Montanari, G. Ramis, C. Resini, M. Sisani. *Int. J. Hydrogen Energy* 35 (2010) 5356-5366.
- [23] M. Li, X. Wang, S. Li, S. Wang, X. Ma, *Int. J. Hydrogen Energy* 35 (2010) 6699-6708.
- [24] A. F. Lucrédio, J. D. A. Bellido E. M. Assaf, *Appl. Catal. A* 388 (2010) 77-85.

- [25] A. Romero, M. Jobbágy, M. Laborde, G. Baronetti, N. Amadeo. *Catal. Today* 149 (2010) 407-412.
- [26] X.P. Yu, W. Chu, N. Wang, F. Ma, *Catal. Lett.* 141 (2011) 1228-1236.
- [27] R. Guil-López, R. M. Navarro, M. A. Peña, J. L. G. Fierro, *Int. J. Hydrogen Energy* 36 (2011) 1512-1523.
- [28] L. Huang, Q. Liu, R. Chen, A. T. Hsu. *Appl. Catal. A* 393 (2011) 302-308.
- [29] A. J. Vizcaíno, M. Lindo, A. Carrero, J. A. Calles. *Int. J. Hydrogen Energy* (2012) 1985-1992.
- [30] J. R. H. Ross, in *Catalysis*, eds. G. C. Bond, G. Webb, J. R. H. Ross, R.S.C London. 7 (1985) 1-45.
- [31] S. Abelló, E. Bolshak, D. Montané, *Appl. Catal. A* 450 (2013) 261-274.
- [32] E. Bolshak, S. Abelló, D. Montané. *Int. J. Hydrogen Energy* 38 (2013) 5594-5604.
- [33] H. M. Rietveld, *J. Appl. Cryst.* 2 (1969) 65-71.
- [34] TOPAS, General Profile and Structure Analysis Software for Powder Diffraction Data, V4.2, Bruker AXS GmbH, Karlsruhe, Germany.
- [35] R. J. Hill C. J. Howard, *J. Appl. Cryst.* 20 (1987) 467-474.
- [36] N. V. Y. Scarlett, I. C. Madsen, *Powder Diffr.* 21 (2006) 278-284.
- [37] R. W. Cheary, A. A. Coelho, *J. Appl. Cryst.* 25 (1992) 109-121.
- [38] E. Uzunova, D. Klissurski, S. Kassabov, *J. Mater. Chem.* 4 (1994) 153-159.
- [39] M. Jitianu, D. C. Gunness, D. E. Aboagye, M. Zaharescu, A. Jitianu, *Mater. Res. Bull.* 48 (2013) 1864-1873.
- [40] O. Clause, B. Rebours, E. Merlen, F. Trifiró, A. Vaccari, *J. Catal.* 133 (1992) 231-246.
- [41] D. C. Puxley, I. J. Kitchener, C. Komodromos, N. D. Parkyn, in *Preparation of Catalysts III*, *Stud. Surf. Sci. Catal.*, eds. G. Poncelet, P. Grange, P. A. Jacobs, Elsevier Science 16 (1983) 237-271.
- [42] S. Abelló, D. Verboekend, B. Bridier, J. Pérez-Ramírez, *J. Catal.* 259 (2008) 85-95.
- [43] R. K. Datta R. Roy, *Am. Mineral.* 53 (1968) 1456-1475.
- [44] N. Dharmaraj, P. Prabu, S. Nagarajan, C. H. Kim, J. H. Park, H. Y. Kim, *Mater. Sci. Eng. B* 128 (2006) 111-114.
- [45] L. Ma, K. Zhou, Z. Li, Q. Wei, L. Zhang, *Corrosion Sci.* 53 (2011) 3712-3724.
- [46] P. R. Graves, C. Johnston, J. J. Campaniello, *Mater. Res. Bull.* 23 (1988) 1651-1660.
- [47] O. N. Shebanova, P. Lazor, *J. Solid State Chem.* 174 (2003) 424-430.
- [48] O. Clause, M. G. Coelho, M. Gazzano, D. Matteuzzi, F. Trifirò, A. Vaccari, *Appl. Clay Sci.* 8 (1993) 169-186.
- [49] L. E. Alzamora, J. R. H. Ross, E. C. Kruissink, L. L. van Reijen, *J. Chem. Soc., Faraday Trans.* 77 (1981) 665-681
- [50] M. S. Lee, J. Y. Lee, D.W. Lee, D. J. Moon, K.Y. Lee, *Int. J. Hydrogen Energy* 37 (2012) 11218-11226.
- [51] F. Auprêtre, C. Descorme, D. Duprez, *Catal. Commun.* 3 (2002) 263-267.

- [52] M. M. Yung, W. S. Jablonski, K. A. Magrini-Bair, *Energy Fuels* 23 (2009) 1874-1887.
- [53] G. Busca, *Chem. Rev.* 107 (2007) 5366-5410.
- [54] J. Comas, F. Mariño, M. Laborde, N. Amadeo, *Chem. Eng. J.* 98 (2004) 61-68.
- [55] C. Melchor-Hernández, A. Gómez-Cortés, G. Díaz, *Fuel.* 107 (2013) 828-835.
- [56] H. Muroyama, R. Nakase, T. Matsui, K. Eguchi, *Int. J. Hydrogen Energy* 35 (2010) 1575-1581.
- [57] L. Huang, J. Xie, R. Chen, D. Chu, W. Chu, A. T. Hsu, *Int. J. Hydrogen Energy* 33 (2008) 7448-7456.
- [58] L. Huang, J. Xie, W. Chu, R. Chen, D. Chu, A. T. Hsu, *Catal. Commun.* 10 (2009) 502-508.
- [59] J. Rass-Hansen, C. H. Christensen, J. Sehested, S. Helveg, J. R. Rostrup-Nielsen, S. Dahl, *Green Chem.* 9 (2007) 1016-1021.

4.6. Appendix for chapter 4:

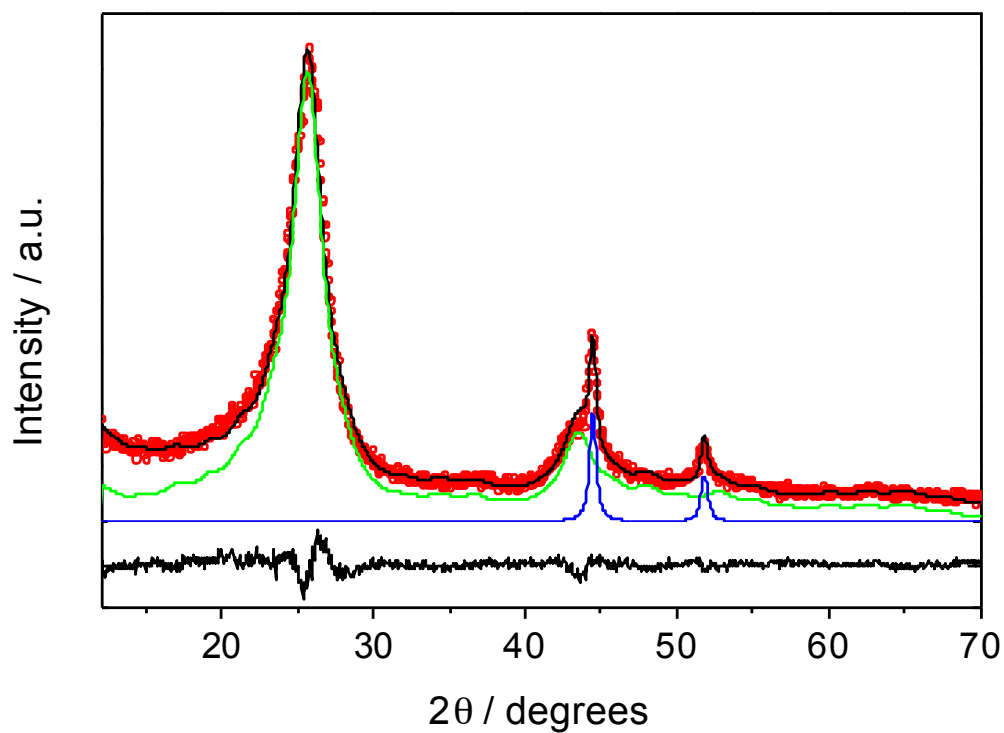


Figure 4.S1. Observed (circles), calculated (continuous lines) and difference diffractograms obtained with TOPAS software for the sample $\text{Ni}_3\text{Al}_{0.8}\text{Fe}_{0.2}\text{-U}$ with Ni and a model for non-crystalline carbon used in the quantitative PONCKS method (Ni 3.14 wt.%, non-crystalline carbon 96.86 wt.%). Conventional Rietveld agreement factor, Rwp 8.13.

Chapter 5

Summary, conclusions and outlook

5.1 Summary

The main goal of the thesis was to develop a stable catalyst for ethanol steam reforming with good selectivity towards hydrogen formation and low tendency to carbon deposition..

The study started with catalysts of Ni-Fe mixed oxides derived from reevesites (Ni-Fe hydrotalcites). The influence of iron content (Ni/Fe ranging from 3 to 1) and the calcination temperature of the catalyst precursor (500 and 800°C) on the reaction performance were studied. Both parameters were important to optimize the steam reforming process because they determined the nature of the oxide (the percentage of crystalline phases, i.e. Ni(Fe)O_x and NiFe₂O₄) and influenced the final size and dispersion of nickel species formed during the reaction. With an increase of iron content in the precursor we observed a positive effect due to the enhancement of catalytic activity and hydrogen selectivity, induced by the improved dispersion of nickel and the alleviation in carbon deposition. The best catalyst (Ni/Fe ratio of 1 and calcined at 500°C) was stable and reached a hydrogen selectivity of up to ca. 60%, with low methane formation. It consisted of a Ni(Fe)O_x + NiFe₂O₄ mixture with high surface area and small Ni⁰ crystallites. At high calcination temperature (800°C) crystallization and growing of NiFe₂O₄ lead to higher carbon deposition and probably Ni⁰ sintering, resulting in lower activity and fast deactivation. The improved performance over catalysts calcined at lower temperature and with lower Ni/Fe ratio, derived from the influence of iron on the structural and electronic properties of the mixed oxides, which induced a slow formation of metallic nickel particles and coke deposits.

The effect of further increasing the iron content was then studied and the best catalyst was tested at different reaction temperatures. An excess of iron in the sample precursor, i.e. Ni/Fe ratios of 0.5, induced the formation of a low surface area spinel phase (NiFe₂O₄), even at low calcination temperature. After performing ESR reaction and characterization we found the formation of the spinel was detrimental, as this caused lower activity and faster deactivation through Ni⁰ sintering. The effect of reaction temperature was evaluated for the

most active catalyst (Ni/Fe =1); increasing reaction temperature from 400°C to 600°C generated less carbon deposits and favored ethanol dehydrogenation combined with steam reforming of acetaldehyde, acetaldehyde decarbonylation, methanation, and ethanol dehydration. However, partial deactivation was present at longer time on stream due to nickel sintering. The optimum temperature for higher ethanol dehydrogenation and acetaldehyde reforming, coupled with lower methane production was 500°C.

After successful confirmation of the promising performance at the selected experimental conditions and Ni/Fe ratio, we decided to use ternary Ni-based hydrotalcites, including iron and aluminum as the trivalent metals. The steam reforming of ethanol was then evaluated over Ni-Al, Ni-Fe and Ni-Al-Fe mixed oxides (with common formula $\text{Ni}_3\text{Al}_{1-x}\text{Fe}_x$) derived from takovite, reevesite and mixtures thereof. Compared to pure binary systems (Ni_3Al and Ni_3Fe), the ternary systems showed the best performance in ethanol reforming, leading to a high and stable hydrogen selectivity of up to ca. 70% in 100 h-reaction tests. Ni_3Al behaved as a typical reforming Ni-catalyst, favoring both ethanol dehydrogenation and dehydration, the latter being responsible for ethylene formation and subsequent gradual and slow polymerization into coke. On the opposite side, the Ni_3Fe catalyst experienced a fast deactivation, mainly related to both fast coke formation and nickel sintering, as demonstrated by characterization of the used materials. The increased activity of the ternary systems can be attributed to a cooperative effect between aluminum and iron, favoring ethanol dehydrogenation as the primary step, followed by acetaldehyde reforming and/or cracking with limiting the dehydration route to ethylene.

Overall this thesis confirms the fact that Ni-Al-Fe mixed oxides derived from hydrotalcite-like precursors are perspective materials for effective ethanol steam reforming.

5.2 Conclusions

The main conclusions that can be inferred as a result of the completion of the present work are the following:

1. The process of steam reforming of ethanol was studied over Ni-Fe mixed oxides derived from Ni-Fe hydrotalcites. The effect of Ni/Fe ratio ranging from 3 to 0.5 in the resulting material on catalytic performance was investigated. The chemical and activity properties of the derived mixed oxides are strongly affected by the amount of iron, which exhibits a positive role in nickel-based catalysts. This is possibly due to the enhancement of catalytic activity and hydrogen selectivity induced by the improved dispersion of nickel and the alleviation in carbon deposition. The best catalyst, with a Ni/Fe ratio of 1 and calcined at 500°C, demonstrated high and stable hydrogen selectivity of up to ca. 60%, low methane content, and consisted of a mixture of Ni(Fe)O_x solid solution and NiFe₂O₄ with very small crystallites. However, an excess of iron in the sample precursor, i.e. Ni/Fe ratios of 0.5, induced the formation of a low surface area spinel phase (NiFe₂O₄), even at low calcination temperature. This resulted in lower activity and faster deactivation in the reaction.
2. We found that the temperature of calcination of the reevesite precursors was critical for the catalytic behavior, as it determined the nature of the oxide (the percentage of crystalline phases, i.e. Ni(Fe)O_x and NiFe₂O₄) and affected the final size and dispersion of nickel species formed during the reaction. Crystallization and growing of NiFe₂O₄ at higher calcination temperature - 800°C (compared to other group of materials calcined at 500°C) associated with higher carbon deposition and probably Ni⁰ sintering led to lower activity and fast deactivation. High surface area, higher iron content, lower reducibility of nickel species and small nickel crystallite sizes led to a higher activity in ethanol dehydrogenation, acetaldehyde decarbonylation and reforming, and WGS.

3. The influence of reaction temperature was investigated over the best catalyst. We discovered that the catalyst was less deactivated when the reaction was performed at 500°C, together with sufficient hydrogen yield. Increasing the reaction temperature from 400°C to 600°C generated less carbon deposits and favored ethanol dehydrogenation combined with steam reforming of acetaldehyde, acetaldehyde decarbonylation, methanation, and ethanol dehydration. However, partial deactivation is present at longer time on stream due to nickel sintering. Under these conditions, the best catalyst reached a stable hydrogen selectivity of up to 60%.
4. The steam reforming of ethanol over Ni-Al, Ni-Fe and Ni-Al-Fe mixed oxides prepared through the hydrotalcite route, was investigated. Binary systems exhibited a significant deactivation due to ethylene formation or nickel sintering as demonstrated by characterization of the used materials. In the intermediate situation, Ni-Al-Fe oxides were more active catalysts than their binary counterparts for ESR, rendering high and stable hydrogen selectivity of up to ca. 70%. A synergic effect in the electronic, structural and activity properties of the resulting oxides between the three metals was manifested and finally allowed performing long reactions, of up to 120 hours on stream without significant deactivation.

5.3 Outlook and future work

A possible application for the catalysts investigated here could be in the area of portable or stationary hydrogen generators in automobile industries as well as in electronic equipment. Such devices can use renewable energy sources like bioethanol and can be safer compared to high-pressure hydrogen storage vessels or more economically feasible than other hydrogen-based alternative energy sources. Future work can be focused on the development and optimization of these catalytic reformers design. For example, it is necessary to justify which type of reactor is more suitable for the selected catalyst: fixed bed reactor, monolithic reactor,

wall-coated heat exchanger, micro-channel reactor or metallic foam reactor. It is important to continue investigating the ways to overcome the deactivation by introducing doping agents and finding stable catalytic systems able to work for long-term reactions at weight hourly space velocities, which are sufficiently high to meet the demands of future fuel processing reactors. Another possible problem to solve is to maintain low CO levels at the reactor outlet, and thus avoid fuel cell deterioration.

5.4. List of publications

Journals

- **“Thermodynamic analysis of fuel processors based on catalytic-wall reactors and membrane systems for ethanol steam reforming”** Daniel Montané, Evgeny Bolshak, Sònia Abelló. *Chemical Engineering Journal*, 175 (2011), 519-533
- **“Ni-Fe catalysts derived from hydrotalcite-like precursors for hydrogen production by ethanol steam reforming”** Sònia Abelló, Evgeny Bolshak, Daniel Montané. *Applied Catalysis A: General*, 450 (2013) 261-274.
- **“Ethanol steam reforming over Ni-Fe-based hydrotalcites: effect of iron content and reaction temperature”**. Evgeny Bolshak, Sònia Abelló, Daniel Montané. *International Journal of Hydrogen Energy*. 38 (2013) 5594-5604.
- **“Ternary Ni-Al-Fe catalysts for ethanol steam reforming”**. Sònia Abelló, Evgeny Bolshak, Francesc Gispert-Guirado, Xavier Farriol, Daniel Montané. *Catalysis Science and Technology*. 4 (2014) 1111-1122.

Contributions to conferences

- **7th International Conference on Environmental Catalysis, Lyon, France.** (2-6 September 2012) “Hydrogen production by Ethanol Steam Reforming over Ni-Fe catalysts derived from Hydrotalcite-like precursors”.
- **20th European Biomass Conference, Milan, Italy.** (18-22 June 2012) “Activated Nickel-Iron hydrotalcite catalysts for ethanol steam reforming”
- **12th Mediterranean Congress of Chemical Engineering, Barcelona, Spain.** (15-18 November 2011) “Cobalt-based catalysts for steam reforming of ethanol”
- **9th Doctoral Day, URV, Tarragona, Spain.** (27 April 2011) “Cobalt based catalysts for the steam reforming of ethanol”. Awarded with 2nd place as «best research project» among second year PhD students.

5.5. About the author

Evgeny Bolshak was born on 29 March of 1984 year in Russia. After finalizing the high-school in 2001 he studied at Mendeleev University of Chemical Technology of Russia (Moscow) from 2001 till 2007. After defending his master's degree on specialty of basic organic and petrochemical synthesis with honor Evgeny joined LG Chem Company (Moscow office) where he worked as technical specialist till year 2009. Then he continued his research career as PhD student at Universitat Rovira i Virgili in chemical engineering department.